Effect of Dissolved Air and System Pressure on Pool Boiling from Biphilic Surfaces

山田, 将之

https://doi.org/10.15017/1931912

出版情報：九州大学, 2017, 博士（工学）, 課程博士
バージョン：
権利関係：

Effect of Dissolved Air and System Pressure on Pool Boiling from Biphilic Surfaces

Masayuki Yamada

Table of Contents

List of Figures iv

List of Tables xi

Nomenclature xii

Chapter 1 Introduction 1

1.1 Background 1

1.2 Basics of boiling phenomenon 4

1.2.1 Boiling curve 4

1.2.2 Boiling incipience 6

1.2.3 Bubble growth and departure 8

1.2.4 Heat transfer mechanism of nucleate boiling 10

1.2.5 Factors affecting pool boiling 11

1.3 Surface wettability 13

1.4 Literature survey 15

1.4.1 Improvement of boiling characteristics through wettability modification 16

1.4.2 Effect of dissolved air on boiling characteristics 23

1.4.3 Boiling characteristics under sub-atmospheric conditions 25

1.5 Research objectives 27

1.6 Thesis organization 28

Chapter 2 Fabrication of heating surfaces 30

2.1 Fabricating methods 30

2.1.1 Mirror-finished copper surface 30

2.1.2 TiO_2 sputtering 31

2.1.3 PTFE spray coating 32

2.1.4 P-HNT coating 33

2.1.5 Ni/TFEO electroplating 34

2.2 Contact angle measurement 36

Chapter 3 Effect of dissolved air on subcooled boiling 37

3.1 Experimental apparatus 37

3.1.1 Open type apparatus 37

3.1.2 Closed type apparatus 39

3.1.3 Heat transfer block 40

3.2 Experimental procedures and data reduction 41

3.2.1 Degassing 41

3.2.2 Boiling heat transfer experiment 45

3.2.3 Single bubble experiment 46

3.3 Boiling heat transfer characteristics 47

3.3.1 Mirror-finished copper surface 47

3.3.2 Biphilic surface 51

3.4 Single bubble behavior 55

3.4.1 Bubble behavior and bubble departure diameter and frequency 55

3.4.2 Temperature inside bubble 60

3.5 Numerical simulation of single bubble behavior 64

3.6 Heat transfer mechanisms 68

3.7 Summary 70

Chapter 4 Effect of system pressure 72

4.1 Experimental apparatus and heating surfaces 72
4.2 Experimental procedures and data reduction 73
4.2.1 Boiling heat transfer experiment 73
4.2.2 Single bubble experiment 75
4.3 Boiling heat transfer characteristics 75
4.3.1 Heat transfer enhancement with a biphilic surface 76
4.3.2 Effects of spot diameter and pitch 83
4.3.3 Transition to intermittent boiling on a biphilic surface 88
4.3.4 Comparison with previous studies 94
4.4 Single bubble behavior 95
4.4.1 Bubble behavior and TPCL motion 95
4.4.2 Bubble departure diameter 98
4.4.3 Bubble growth rate 101
4.5 Summary 103

Chapter 5 Conclusions 106

Acknowledgement 110

References 111

Chapter A Appendix 126
A-1 Uncertainty analysis 126
A-2 Contact angle measurement 127
A-3 Gas solubility 128
A-4 Detail of numerical simulation 129

List of Figures

Figure 1.1 A typical boiling curve obtained for upward facing surfaces or horizontal wires with controlled heat flux. Schematics of boiling modes are displayed above the graph. 5

Figure 1.2 Condition for heterogeneous nucleation from a conical cavity with a radius of r_c. 8

Figure 1.3 Schematic of bubble cycle. 9

Figure 1.4 Heat transfer mechanism during (a) bubble growth and (b) departure processes. 10

Figure 1.5 Effects of various parameters on boiling curve. 12

Figure 1.6 Equilibrium of three interfacial forces at the three phase contact point. 14

Figure 1.7 Schematic of Cassie-Baxter model. 15

Figure 2.1 The mirror-finished copper surface: (a) photo, (b) SEM image, and (c) 3-D profile. Blue scale bar: 10 mm. Green scale bar: 5 μm. 31

Figure 2.2 The TiO_2 sputtered surface: (a) photo, (b) SEM image, and (c) 3-D profile. Blue scale bar: 10 mm. Green scale bar: 500 nm. 32

Figure 2.3 (a) A photo and (b) 3-D profile of the PTFE-spray-coated surface. Blue scale bar: 10 mm. SEM images of (c) the center region of the coating and (d) the border with a copper substrate. Green scale bar: 10 μm. Red scale bar: 30 μm. 33

Figure 2.4 (a) A photo of a TiO_2 surface coated with the Polymer-modified HNT (P-HNT), whose diameter is 6 mm. Blue scale bar: 10 mm. SEM images of P-HNT coating taken from (b) the top and (c) an inclined angle. Green scale bar: 50 μm. Red scale bar: 1 μm. 34

Figure 2.5 (a) A photo of a copper surface spotted with the Ni/TFEO electroplating. Blue scale bar: 10 mm. (b) A 3-D profile and (c), (d) SEM images of the plated surface.

Green scale bar: 10 μm. 36

Figure 3.1 A schematic of the “open” type experimental system, which consists of a pool boiling apparatus (1-11) and peripheral equipment (12-23). 38

Figure 3.2 A schematic of the “closed” type experimental apparatus. 39

Figure 3.3 A schematic of the heat transfer block. 40

Figure 3.4 Schematic of the degassing procedure in the pure subcooled condition. A red-coloring of the valve numbers (I-VI) means the valve being opened. 42

Figure 3.5 (a) A departed bubble captured by the high speed camera. A bubble departure diameter was measured as an average of vertical and horizontal widths of the bubble. (b) Length scale of captured videos was calibrated by capturing a ruler putted above the hydrophobic spot. 46

Figure 3.6 (a) A device for measurement of a temperature profile inside a bubble, which can be mounted onto the boiling vessel (b). The tip of the thermocouple can be precisely moved in three-dimensions with the help of a three-axis linear translation positioner. 47

Figure 3.7 Comprasion of boiling curves of the mirror-finished copper surface at $\Delta T_{\mathrm{sub}} =$ 20 K under the gassy and pure subcooled conditions. The arrows indiacte ONB, and the black solid line is calculation of Lloyd and Moran’s correlation, eq. (3.7) and (3.8). 48

Figure 3.8 Comparison of boiling behavior of the mirror-finished copper surface at ΔT_{sub} $=$ 20 K and $\Delta T_{\mathrm{sat}} \approx$ 13, 16, 22 K under (a) gassy and (b) pure subcooled conditions. For the pure subcooled condition, the boiling behavior at $\Delta T_{\mathrm{sat}} \approx$ 13 K is omitted because it is still in the natural convection region. 50

Figure 3.9 (a) A photo of the biphilic surface having hydrophobic spots made of the PTFE spray (6 mm in diameter and 7 mm in pitch) on the TiO_2 surface. Scale bar: 10 mm. (b) Boiling curves of the biphilic surface at $\Delta T_{\mathrm{sub}} = 20$ K under the gassy and pure subcooled conditions. 51

Figure 3.10 Evolution of boiling behavior after ONB on the biphilic surface at $\Delta T_{\mathrm{sub}} = 20$ K under the gassy subcooled condition. 53

Figure 3.11 Comparison of boiling behavior on the biphilic surface at $\Delta T_{\mathrm{sub}} = 20$ K and $\Delta T_{\mathrm{sat}} \approx 3, 6, 13$ K under (a) gassy and (b) pure subcooled conditions. 54

Figure 3.12 Evolutions of bubble behavior in the gassy subcooled condition at $\Delta T_{\mathrm{sub}} = 20$ K and $\Delta T_{\mathrm{sat}} = -1.2$, 7.1, and 11.5 K. Scale bar: 3 mm. 56

Figure 3.13 (a) The bubble departure frequency, f_{d}, and (b) diameter, d_{d}, from a single hydrophobic spot (with $\varphi = 6$ mm and $\theta \approx 140^{\mathrm{o}}$) coated on superhydrophilic surface ($\theta \approx 0^{\mathrm{o}}$). The results of Tashiro's study [155] taken with a copper surface ($\theta = 70^{\mathrm{o}}$) having a single hydrophobic spot ($\theta = 120$-127^{o}) are also plotted for comparison. (c) Relationship of f_{d} vs. d_{d}. 57

Figure 3.14 (a) Evolution of a bubble shape with increasing ΔT_{sat} at $\Delta T_{\mathrm{sub}} = 20$ K. The red dash line represents the heating surface. Blue scale bar: 3 mm. (b) Plot of the distribution of a time-averaged bubble height, H_{b}, over various ΔT_{sat}. Error bars for the horizontal and vertical axes show the measurement error and the maximal and minimal values for five seconds' measurements, respectively. Blue dash line is calculation of eq. (3.10). (c) The model for eq. (3.10), where a bubble is assumed to be consist of a cylinder with H_{c} in height and r in radius, and a hemispherical cap 59

Figure 3.15 (a) A measurement procedure of vapor temperature inside a bubble. (b) Temperature history during the measurement at $\Delta T_{\mathrm{sub}} = 20$ K and $\Delta T_{\mathrm{sat}} = 6.1$ K under the gassy subcooled condition. 61

Figure 3.16 (a) Profiles of the vapor temperature, T_{v}, inside a bubble under the gassy subcooled condition at the various T_w. The detailed temperature profile at T_w = (b) 98.4 $^\mathrm{o}$C and (c) 109.6 $^\mathrm{o}$C. The red triangles represent T_w obtained from the temperature gradient inside the heat transfer block. Blue solid lines are the power approximations of T_v. Error bars indicate the maximal and minimal values for 10 seconds' measurements. 62

Figure 3.17 (a) Temperature profiles inside a bubble under the pure subcooled condition at T_w = 103.8 and 108.3 $^\mathrm{o}$C. For comparison, the results of the gassy subcooled condition at similar T_w are included. (b) The partial pressures of non-condensable gas, P_g, inside a bubble calculated from the minimum values of T_v (summarized in Table 3.3). 63

Figure 3.18 (a) Bubble behavior in the binary system (water + nitrogen), which are shown side by side with experimental observations (blue dash lines represent the heating surface). The color scale indicates fluid density normalized by the critical density of water. Nondimensional time, τ, is scaled by the bubble departure period. Contact angles of the yellow- and green-colored portions of the heating surface are set to be 120$^\mathrm{o}$ and 10$^\mathrm{o}$, respectively. (b) A spatial distribution of nitrogen at the same instants as in (a), whose normalized density is represented by the color scale. (c) Bubble behavior in the single component system. 65

Fig. 3.19 Evolutions of the local velocity distribution of the bubble interface in the (a) binary (water + nitrogen) and (b) single component (water) systems. (c) Total tangential mass fluxes integrated over the liquid-vapor interface, $M^{|}$, versus nondimensional time, τ. 67

Figure 3.20 Classification of heat transfer mechanisms of the gassy subcooled boiling from the biphilic surface. The data of pure subcooled boiling on biphilic and copper surfaces are plotted for comparison. NC: Natural convection. LHT: Latent heat transport. MC: Marangoni convection. NB: Nucleate boiling. 69

Figure 4.1 Biphilic surfaces with different diameters and pitches of hydrophobic spots, (a) Surface A (φ = 0.5 mm, p = 1.5 mm), (b) Surface B (φ = 0.5 mm, p = 3.0 mm), and (c) Surface C (φ = 1.0 mm, p = 1.5 mm). Blue scale bar: 10 mm. 72

Figure 4.2 Difference between the saturation temperatures at the liquid surface, $T_{\mathrm{sat,s}}$, and heating wall, $T_{\mathrm{sat,w}}$, caused by the hydrostatic pressure of water column with a height of 120 mm, at the various liquid surface pressures, P_{s}. 74

Figure 4.3 (a) Boiling heat transfer comparison between Surface B (φ = 0.5 mm, p = 3.0 mm) and Surface D (mirror-finished copper) at $P \approx 102.3$ kPa and 14.0 kPa ($T_{\mathrm{bulk}} \approx 50$ °C). Error bars show the maximal and minimal values of two minutes' measurements in the steady state. (b) The corresponding h vs ΔT_{sat} in the nucleate boiling region after ONB. Error bars show the measurement uncertainty. 77

Figure 4.4 Relationships between the standard deviation, SD, of T_1 (measured at 3 mm below the top surface) and q on (a) Surface D and (b) B. The data at and above the heat flux of arrowed points are in the nucleate boiling regime. Notice that the vertical axis of (a) is broken for visibility. Transient temperature measurements of T_1 on (c) Surface D and (d) B at $P \approx 102.3$ kPa and 14.0 kPa during two minutes in the steady state at q = 163-186 kW/m^2. The red-dot-dash lines represent the mean values. 78

Figure 4.5 Evolution of boiling behavior on Surface D at q = 165.4 kW/m^2 and P = 13.7 kPa, corresponding to the lower panel in Fig. 4.4c. Blue scale bar: 10 mm. 79

Figure 4.6 Evolutions of boiling behavior on Surface B at P = (a) 102.3 kPa and (b) 14.0 kPa, and various heat fluxes. Blue scale bar: 10 mm. 81

Figure 4.7 (a) Comparison of boiling curves between the three biphilic surfaces (Surface A, B, and C) at $P \approx 101.3$ kPa and 13.8 kPa. The solid lines indicate the calculations of eq. (4.3) at the respective pressures. (b) The corresponding h vs ΔT_{sat} in the nucleate boiling region. Error bars in (a) and (b) show the measurement uncertainty. 83

Figure 4.8 Effect of (a) a pitch and (b) diameter of the hydrophobic spots. The vertical axis, $h_{\mathrm{meas}}/h_{\mathrm{corr}}$, is HTC normalized by the calculations based on eq. (4.3) for the respective pressures. 84

Figure 4.9 Evolutions of boiling behavior on Surface A at $P =$ (a) 101.3 kPa and (b) 13.6 kPa, and various heat fluxes. Blue scale bar: 10 mm. The red and blue arrows indicate bubble merging between neighboring spots and an isolated bubble, respectively. 85

Figure 4.10 Evolutions of boiling behavior on Surface C at $P =$ (a) 101.5 kPa and (b) 13.8 kPa, and various heat fluxes. Blue scale bar: 10 mm. 87

Figure 4.11 (a) Boiling curves and (b) HTC (after ONB) obtained on Surface B at different pressures. Error bars in (a) and (b) show the maximal and minimal values over two minutes' measurements in the steady state and the measurement uncertainty, respectively. The solid lines in (a) represent the calculations of eq. (4.3) at $P =$ 101.3 kPa and 6.9 kPa. (c) The corresponding $h_{\mathrm{meas}}/h_{\mathrm{corr}}$ vs q. 89

Figure 4.12 Relationships between SD of T_1 and q on Surface B at various pressures. Data before ONB is omitted. Notice that the vertical axis is broken for visibility. 91

Figure 4.13 Evolutions of boiling behavior (left panels) and the corresponding transient measurements of T_1 during two minutes in the steady state (right panels) on Surface B at $q \approx 60$ kW/m^2 and $P =$ (a) 50.7 kPa, (b) 21.8 kPa, (c) 8.8 kPa, and (d) 6.9 kPa. Blue scale bar: 10 mm. The red-dot-dash lines in the right panels represent the mean values. 91

Figure 4.14 Evolutions of boiling behavior (left panels) and the corresponding transient temperature measurements of T_1 during two minutes in the steady state (right panels) on Surface B at $P =$ 6.9 kPa, and $q =$ (a) 164.0 kW/m^2 and (b) 293.7 kW/m^2.

Blue scale bar: 10 mm. The red-dot-dash lines in the right panel represent the mean values. 93

Figure 4.15 Evolutions of single bubble behavior growing from a hydrophobic spot (φ = 0.5 mm) at P = (a) 103.9 kPa, (b) 49.2 kPa, (c) 33.0 kPa and (d) 21.5 kPa. The bottom panels in (c) and (d) are enlarged views of a vicinity of the heating surface (pointed out with a red-dot line). Blue scale bar: 2 mm. Green scale bar: 4 mm. 96

Figure 4.16 Behavior of the complete bubble departure at various pressures and heat inputs with several spot diameters. Blue scale bar: 5 mm. 98

Figure 4.17 Bubble departure diameter, d_d, of surfaces with different hydrophobic spot diameters at various heat input, Q, and P. Blue and red solid lines are calculations of eq. (1.12) and (1.13), respectively. 99

Figure 4.18 TPCL behavior map (pinned or depinned). The vertical axis is the system pressure normalized with P^*, corresponding the pressure where $d_\mathrm{Zuber}{}^*$ becomes equal to d_Cole. 101

Figure 4.19 Evolutions of a bubble height, H, and width, W, (top panels) and averaged bubble radius, r_ave, (bottom panels) under (a) pinned and (b) depinned conditions, where r_ave is derived by taking an average of H and W. Under the depinned condition, depinning of TPCL occurs at the arrowed point. 102

List of Tables

Table 1.1 Summary of previous works about (super)biphilic surfaces. 22

Table 2.1 Sputtering conditions. 31

Table 2.2 Summary of surface properties and fabrication methods. 36

Table 3.1 ΔT_{ONB} [K] corresponding to Fig. 3.7. 48

Table 3.2 ΔT_{ONB} [K] corresponding to Fig. 3.9b. 52

Table 3.3 The minimum values of the vapor temperature, $T_{\mathrm{v,min}}$, at various T_{w}. 63

Table 4.1 Surface information. 73

Table 4.2 ΔT_{ONB} [K] corresponding to Fig. 4.3a. 77

Table 4.3 Two characteristic regions in the boiling curves, shown in Fig 4.7(a), represented by $n \approx 3$ and 1.3 for the equation of $q \sim \Delta T_{\mathrm{sat}}{}^{n}$. 88

Table 4.4 The effect of the pressure level on ΔT_{ONB} of Surface B. 89

Table 4.5 Comparison of the present result and recent studies for enhancement of sub-atmospheric pool boiling of water and water-based liquid. 94

Nomenclature

C	solubility	mol/mol
d	diameter	m
d_c	contact diameter	m
D	Diffusion coefficient	m^2/s
f	frequency	Hz
f_A	area fraction	-
g	acceleration due to gravity	m/s^2
h	heat transfer coefficient	$W/(m^2 \cdot K)$
H	height	m
H_e	Henry's constant	Pa/mol
l_a	Laplace's coefficient	m
L	total length of the bubble interface	m
L_{lv}	latent heat of vaporization	J/kg
$M^{\parallel}$	total tangential mass fluxes integrated over the bubble interface	$kg/(m \cdot s)$
p	pitch of hydrophobic spots	m
P	pressure	Pa
P_{atm}	atmospheric pressure	Pa
q	heat flux	W/m^2
Q	amount of heat	W
r	radius	m
r_c	radius of a cavity	m
R_a	arithmetic average roughness	m
Rf	Roughness factor	-

t	time or period	s
T	temperature	$^{\circ}$C
ΔT_{sat}	degree of superheat	K
ΔT_{sub}	degree of subcooling	K
ΔT_{ONB}	wall superheat at the onset of nucleate boiling	K
x	distance	m

Greek symbols

γ	interface energy	$\mathrm{J/m^2}$
δ	thickness of superheated liquid layer	m
θ	contact angle	$^{\circ}$
λ	thermal conductivity	W/(m·K)
v	kinetic viscosity	$\mathrm{m^2/s}$
ρ	density	$\mathrm{kg/m^3}$
σ	surface (interface) tension	N/m
τ	nondimensional time	-
φ	diameter of hydrophobic spots	m

Subscripts

b	bubble
bulk	bulk
c	copper
d	bubble departure
g	gas phase
l	liquid phase

lv	liquid-vapor interface
min	minimal value
s	liquid surface
sat	saturated condition
sl	solid-liquid interface
sv	solid-vapor interface
v	vapor phase
w	heating surface

Dimensionless numbers

Bo	Bond number
Ja	Jacob number
Nu	Nusselt number
Pr	Prandtl number
Ra	Rayleigh number

Chapter 1

Introduction

1.1 Background

Boiling is a familiar phenomenon, experienced in our daily life such as food preparation and sterilization treatment. Importance of boiling phenomenon in the industrial field dramatically increased in the 1730s, when the first reliable steam engine was invented by James Watt. Steam engines, needless to say, convert heat energy of steam generated in a boiler to mechanical work. From the Watt's invention, boilers have been used for power sources of trains, ships, and power plants. Boiling phenomenon in boilers plays a crucial role in the present-day society, for instance, power sources for steam turbines of thermal and nuclear power plants and heating and humidification in the food processing field [1, 2]. Boiling is also in wide use as an efficient way to cool high-temperature objects. In the steel-making process, good understanding and control of boiling behavior are essential because hot steel plates are cooled down by evaporation and boiling of splayed water droplets [3]. Thermosyphons, a heat transfer device using boiling and condensation, have been applied for electronics cooling because of their superior performance and energy saving [4, 5]. The superconducting technology, utilized in MRIs (Magnetic Resonance Imaging) and linear motor cars, requires cooling to a very low temperature, which is achieved with boiling of helium or nitrogen [6, 7]. In addition, refrigerators and air-conditioners draw heat from a low-temperature heat source through boiling and release it to a high-temperature heat source through condensation with the help of a heat pump. Applications of the heat pumps are not only in the former examples but also in various fields: EcoCute (which has been introduced as energy saving equipment), utilization of geothermal energy, and waste heat recovery systems [8-10].

As mentioned above, boiling phenomenon is widely used in both the private and industrial sectors. Hence, improvement of boiling heat transfer based on understanding of the phenomenon has a great impact on our society. In 2010, for example, data centers consume 1.3% of the total electricity use in the world [4]. The value is expected to further increase due to the increasing demand in developing and industrializing countries. Almost 50% of that electricity consumption is used for thermal management of CPUs in order to maintain their temperature appropriately [11, 12]. Therefore, the enormous energy consumption in the data centers can be significantly reduced by enhancement in the efficiency of cooling devises through improvement of boiling performance. Energy consumption of heating, cooling, and hot water supply in the house hold sector exceeds seven percent of the total energy consumption of Japan [13]. According to NEDO (New Energy and Industrial Technology Development Organization), moreover, unused energy of 1000 billion kWh (comparable to the annual gross generation in Japan) is annually discarded as waste heat [14]. Developments of high-efficiency heat exchangers and heat pumps are capable of significantly contributing to the resolution of these problems.

Now, as for the history of boiling research, scientific treatment of boiling phenomenon began in the 1930s, more than 100 years later than the industrial revolution started from the invention of the steam engine [15, 16]. Jakob and Fritz published an article about bubble behavior and boiling heat transfer in 1931. At around the same time, Nukiyama [17] carried out pool boiling experiments of water around a platinum wire heated by Joule effect and obtained the Nukiyama curve (so-called boiling curve) which gives the entire picture of characteristics of boiling heat transfer. Although some important papers were published after that, boiling phenomenon was actively studied from the 1950s to 1960s on the back of significant developments of nuclear power and aviation technologies [18]. In this period, various studies were conducted with an aim to reveal mechanisms of pool boiling [19-23], and empirical equations and physical models widely used today were proposed: the correlations for nucleate boiling heat transfer of Rohsenow [24], Kutateladze [25], and Nishikawa and Yamagata [26], the CHF (Critical Heat Flux) model of Zuber [27], and the correlation for film boiling heat transfer of Berenson [28]. In the 1970s, enhancement of boiling performance attracted much research efforts due to the increased seriousness of the energy problem. Consequently, the demand resulted in development of high performance heating surfaces, such as Thermoexcel [29] and UC High Flux [30]. Thence, many works have been conducted for further enhancement of boiling performance and unveiling of boiling phenomenon with various techniques to this day. The former includes nano-fluids [31], fluid mixtures (immiscible mixtures, high-carbon alcohol aqueous solutions, and so on) [32, 33], nano/micro-structured surfaces [34, 35], wettability modification of a heating surface [36], and honeycomb porous plates [37]. On the other hand, examples of the latter are listed as below: observation of solid-liquid contact behavior by means of the total reflection method [38], local and instantaneous measurements of heat flux and wall temperature with MEMS (Micro Electro Mechanical Systems) sensors or high-speed infrared cameras [39-41], and measurements of micro-layer thickness by applying the laser distinction method [42].

In addition to the above, multifarious works are being undertaken, and it is extremely difficult to grasp all of them. The number of the scientific papers with the word of “boiling” in their title, abstract, or keywords has been steadily increasing from 1330 in 2000 to 2510 in 2010, and reached 3040 in 2016. The reason that boiling research attracts increasing attention even now, more than 80 years passed from Nukiyama’s work, is because boiling is a highly-complex phenomenon accompanying phase change as well as has a vital engineering importance.

1.2 Basics of boiling phenomenon

In this section, an overview of boiling phenomenon is introduced, focusing on pool boiling which is the target of the present study.

1.2.1 Boiling curve

Characteristics of boiling heat transfer can be represented by a graph of heat flux, q, against wall superheat, ΔT_{sat}, namely boiling curve. Figure 1.1 shows a typical boiling curve obtained for upward facing surfaces or horizontal wires with controlled heat flux [43]. Schematics of boiling modes are also displayed above the graph.

By applying heat to a surface, heat transfer is initially dominated by natural convection without the case of microgravity. When ΔT_{sat} reaches a certain value (point A in Fig. 1.1), a vapor bubble is generated on the surface, resulting in the transition from natural convection to nucleate boiling. The point A is called the onset of nucleate boiling (ONB) point and the corresponding ΔT_{sat} is defined as wall superheat at ONB, ΔT_{ONB}. Since heat transfer coefficient (HTC) of nucleate boiling is one to two orders of magnitude greater than that of natural convection, a gradient of the boiling curve increases significantly. In boiling of low-surface-tension liquids or on low-surface-energy substrates, a number of nucleation sites are activated simultaneously at a higher ΔT_{sat}, causing a decrease in ΔT_{sat} for a constant q (in other words, an overshoot appears). The overshoot, however, is not seen on boiling curves obtained with decreasing q.

In the partial nucleate boiling region, corresponding to the early stage of nucleate boiling, isolated bubbles depart from the surface (Region II in Fig. 1.1). The number of nucleation sites and frequency of bubble departure increases as q rises. As a result, bubbles start to merge with neighboring and foregoing bubbles. Such boiling behavior is defined as fully developed nucleate boiling (Region III in Fig. 1.1). In the region, jet-like release of bubbles occurs, and mushroom-

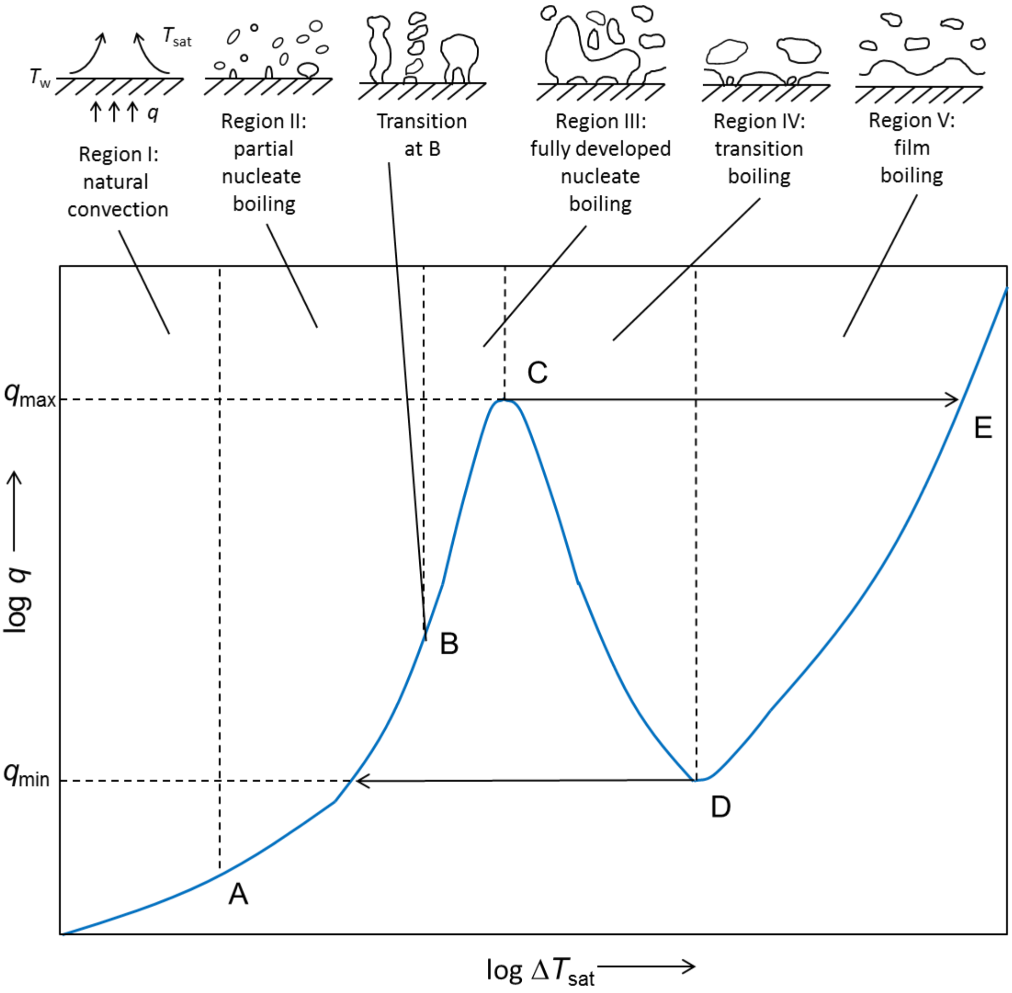

Figure 1.1 A typical boiling curve obtained for upward facing surfaces or horizontal wires with controlled heat flux. Schematics of boiling modes are displayed above the graph.

shaped bubbles, supported by several stems, are formed on the surface.

By further increasing q, liquid flow toward the surface tends to be obstructed because of departure of large bubbles with a higher frequency. Finally, the heat transfer mode turns in to film boiling, where there is no contact between the liquid and surface due to a vapor blanket formed at the solid-liquid interface. The corresponding q (point C in Fig. 1.1) is called the critical heat flux (CHF). HTC of film boiling is remarkably low owing to poor heat transfer of conduction through the vapor film and radiation from the substrate. In the case of controlled heat flux, therefore, ΔT_{sat} sharply jumps up once q reaches CHF. Passing through transient boiling (Region IV in Fig. 1.1) immediately, the boiling state is stabilized at point E in Fig.

1.1. On the other hand, film boiling is maintained at q below CHF when boiling curve is taken with decreasing q. It suddenly changes back to nucleate boiling at a certain value of q (point D in Fig. 1.1), which is far below CHF. The heat flux, where the vapor film collapses, is defined as the minimum heat flux (MHF).

Transition boiling, having characteristics of both nucleate boiling and film boiling, is a very unstable boiling mode where ΔT_{sat} increases as q decreases. Stable transient boiling is, thus, obtainable only in experiments with controlled wall temperature.

1.2.2 Boiling incipience

When a spherical vapor bubble with a radius of r exists in liquid at a uniform temperature of T in equilibrium, the force balance at the interface is described as follows (Laplace's equation).

$$P_{\mathrm{v}} - P_{\mathrm{l}} = 2\sigma / r \tag{1.1}$$

where P_{v} and P_{l} are pressures in the vapor and liquid phase, and σ is surface tension. The liquid temperature must be higher than the saturation temperature (that is, superheated condition) to enable bubble nucleation because a pressure inside the bubble is higher than that of the liquid side [44].

From the Clapeyron-Clausius equation,

$$\frac{\mathrm{d}P}{\mathrm{d}T_{\mathrm{sat}}} = \frac{\rho_{\mathrm{l}} \rho_{\mathrm{v}} L_{\mathrm{lv}}}{T_{\mathrm{sat}} \left(\rho_{\mathrm{l}} - \rho_{\mathrm{v}} \right)} \tag{1.2}$$

and eq. (1.1), a degree of liquid superheat necessary to form a stable vapor bubble can be estimated as

$$\Delta T_{\mathrm{sat}} = \frac{T_{\mathrm{sat}} \left(\rho_{\mathrm{l}} - \rho_{\mathrm{v}} \right)}{\rho_{\mathrm{l}} \rho_{\mathrm{v}} L_{\mathrm{lv}}} \cdot \frac{2\sigma}{r} \approx \frac{2\sigma T_{\mathrm{sat}}}{\rho_{\mathrm{v}} L_{\mathrm{lv}} r} \tag{1.3}$$

where ρ is density and L_{lv} is latent heat of vaporization. According to this equation, it is clear that a bubble with a smaller r requires a higher ΔT_{sat}.

There are two types of bubble nucleation: homogeneous nucleation and heterogeneous nucleation. In the homogeneous nucleation, bubble nucleation occurs inside liquid, not including any gas or vapor, at a temperature much higher than T_{sat}. On the other hand, bubbles are formed at the solid-liquid or liquid-liquid interface in the heterogeneous nucleation. ONB in common boiling is due to the heterogeneous nucleation, where defects or cavities on a heating surface work as nuclei.

Based on the schematic shown in Fig. 1.2, ΔT_{sat} needed for bubble nucleation from a cavity with a radius of r_{c} is calculated as follows. From eq. (1.3), to enable bubble growth from the cavity, a vapor temperature must satisfy the following equation,

$$T_{\mathrm{v}} > T_{\mathrm{sat}} + \frac{2\sigma T_{\mathrm{sat}}}{\rho_{\mathrm{v}} L_{\mathrm{lv}} r_{\mathrm{c}}} \tag{1.4}$$

Here, it is assumed that liquid adjacent to the surface has a linear temperature profile in the vertical direction.

$$T_{\mathrm{l}} = T_{\mathrm{sat}} + \Delta T_{\mathrm{sat}}(1 - \frac{x}{\delta}) \tag{1.5}$$

where δ is thickness of the superheated liquid layer, given by using thermal conductivity of the liquid phase, λ_{l}.

$$\delta = \frac{\lambda_{\mathrm{l}} \Delta T_{\mathrm{sat}}}{q} \tag{1.6}$$

To maintain the bubble with a radius of r_{c}, $T_{\mathrm{l}} \geq T_{\mathrm{v}}$ must be satisfied at its apex ($x = r_{\mathrm{c}}$). Hence, from eq. (1.4), (1.5), and (1.6),

$$r_{\mathrm{c}}^2 - \frac{\lambda_{\mathrm{l}} \Delta T_{\mathrm{sat}}}{q} r_{\mathrm{c}} + \frac{2\sigma \lambda_{\mathrm{l}} T_{\mathrm{sat}}}{\rho_{\mathrm{v}} L_{\mathrm{lv}} q} \leq 0 \tag{1.7}$$

is derived. The solution of the above equation leads to a range of r_{c} for cavities activated at a given ΔT_{sat} as below.

$$\left(r_{\mathrm{c}}\right)_{\mathrm{min}}^{\mathrm{max}} = \frac{\lambda_{\mathrm{l}} \Delta T_{\mathrm{sat}}}{2q} \left[1 \pm \sqrt{1 - \frac{8\sigma T_{\mathrm{sat}} q}{\rho_{\mathrm{v}} L_{\mathrm{lv}} \lambda_{\mathrm{l}} \left(\Delta T_{\mathrm{sat}}\right)^2}}\right] \tag{1.8}$$

Incidentally, van Steralen and Cole extensively summarized experimental data, and proved

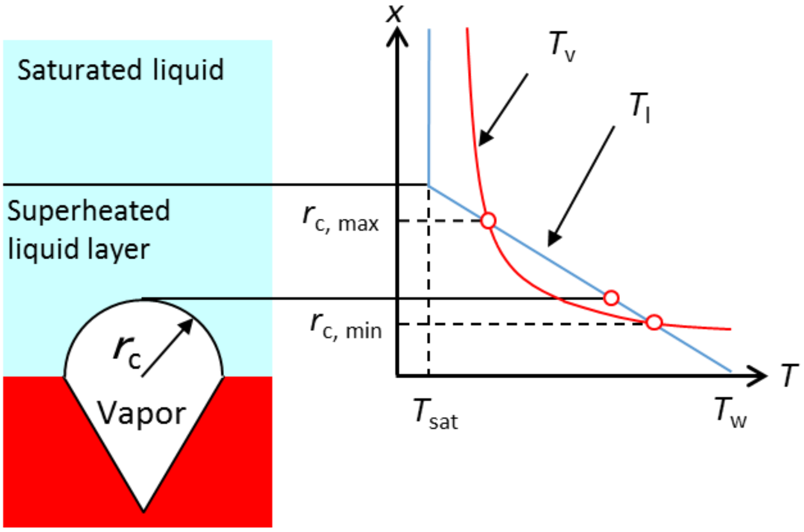

Figure 1.2 Condition for heterogeneous nucleation from a conical cavity with a radius of r_c.

that the actual bubble nucleation from cavities on a substrate is not always due to the heterogeneous nucleation, but highly depends on gas or vapor pre-existing inside them. When gas is trapped inside a cavity, the equilibrium condition (eq. (1.1)) can be rewritten by the following replacing of its right side.

$$\frac{2\sigma}{R} \rightarrow \frac{2\sigma}{R} - P_{\mathrm{g}} \tag{1.9}$$

where P_g is partial pressure of the gas.

1.2.3 Bubble growth and departure

Bubble motion is closely related to heat transfer mechanisms of nucleate boiling. In common nucleate boiling, bubbles repeat nucleation, growth, and departure (this duration is defined as a growth period) with intervals (so-called a waiting period), as shown in Fig. 1.3. Such periodic behavior is called bubble cycle. Here, the waiting period is time required for a reformation of the superheat liquid layer disturbed during the growth period.

A size of a bubble departing from a surface is determined by the balance of forces acting on the bubble: buoyancy, adhesion force (surface tension), drag force, and surrounding liquid

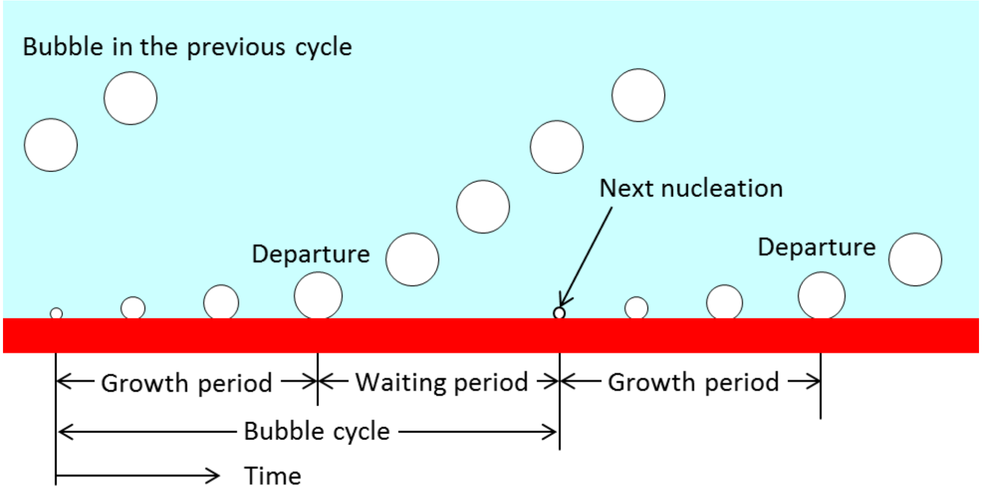

Figure 1.3 Schematic of bubble cycle.

motion [45]. Fritz and Zuber respectively proposed correlations of the bubble departure diameter, d_d, considering only the static balance between surface tension and buoyancy force. In Fritz's model, a contact angle, θ, of a bubbles is assumed to be kept constant, although a contact diameter, d_c, changes as the bubble grows. On the other hands, Zuber's model considers a constant d_c and varying θ. With the Bond number, Bo, the two correlations are expressed as follows.

$$Bo^{1/2} = 0.0209\,\theta \tag{1.10}$$

$$Bo^{1/2} = \left[6d_\mathrm{c}\sqrt{\frac{g(\rho_\mathrm{l}-\rho_\mathrm{v})}{\sigma}}\right]^{1/2} \tag{1.11}$$

$$Bo = \frac{d_\mathrm{d}^2 g(\rho_\mathrm{l}-\rho_\mathrm{v})}{\sigma} \tag{1.12}$$

where g is acceleration due to gravity and a unit of θ is degree.

The above equations cannot be applied for boiling at low pressures where bubbles largely expand due to a reduced ρ_v. Cole, therefore, derived the following correlation by adopting Jacob number, Ja, to reproduce pressure dependency of d_d.

$$Bo^{1/2} = 0.04\,Ja \tag{1.13}$$

$$Ja = \frac{\rho_\mathrm{l} c_\mathrm{pl} \Delta T_\mathrm{sat}}{\rho_\mathrm{v} L_\mathrm{lv}} \tag{1.14}$$

where c_{pl} is heat capacity of liquid.

1.2.4 Heat transfer mechanism of nucleate boiling

In the nucleate boiling, which has a superior HTC, heat is transferred with various heat transfer mechanisms as shown in Fig. 1.4 [46]. During bubble growth process (Fig. 1.4 (a)), a thin liquid layer with a thickness of 1-10 μm (micro-layer) is trapped between the hemispherical bubble and the surface. Evaporation of this microlayer removes heat from the surface in the form of the latent heat (q_{ml}). A plenty amount of heat is transferred though the micro-layer because temperatures at its top and bottom are the saturation and wall temperature—a very steep temperature gradient is generated across the thin layer. In a vicinity of the three phase contact line (TPCL), a reduced thickness of the micro-layer brings enlargement of heat transfer (q_{cl}). Evaporation also takes place at the liquid-vapor interface in the superheated liquid layer (q_{sl}). Additionally, the growing bubble induces liquid motion (so-called, microconvection), resulting in enhanced convective heat transfer (q_{mc}). In a region free from influence of the bubble, heat transfer is dominated by natural convection (q_{nc}).

When the bubble grows up to a certain size, it shifts to the departure process due to an increased buoyancy force. q_{ml} has a minor or no role since the micro-layer has been dried out in the growth process. Although q_{cl} still exists, it is expected to be smaller than that during

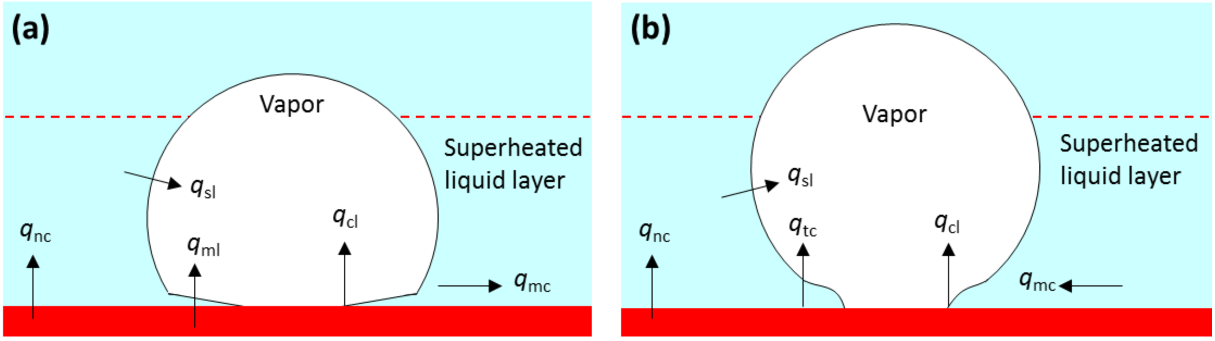

Figure 1.4 Heat transfer mechanism during (a) bubble growth and (b) departure processes.

the growing process, because an advancing contact angle is greater than a receding contact angle, leading to a thicker liquid layer beneath the bubble. q_{sl} contributes to the heat transfer in the same manner as the growth process, excluding a case of subcooled boiling. As the bubble base shrinks, a high-temperature part of the surface, which was being covered with the vapor patch, is rewetted by the surrounding liquid. Consequently, transient conduction from the surface to the liquid occurs (q_{tc}). The shrinkage of the bubble base also brings the microconvection toward the center axis of the bubble (q_{mc}). A wake induced by the bubble departure causes additional microconvection.

1.2.5 Factors affecting pool boiling

There are numerous factors affecting heat transfer characteristics of pool boiling, which can be divided into two types: fluid-side and surface-side [47]. Thermophysical properties of fluid (i.e. density, heat capacity, viscosity, thermal conductivity, latent heat of vaporization, and surface tension) have remarkable influence on boiling features. Since these properties are functions of temperature and pressure, a degree of subcooling, ΔT_{sub}, and system pressure, P, are the representatives of the fluid-side factors. Moreover, liquid level and a degree of gravity affect boiling performance. On the other hand, the surface-side parameters include surface geometry (roughness and structures), inclination, size, thickness, and wettability in addition to thermophysical properties [48, 49]. Fig. 1.5 summarizes how an increase in the respective parameters influences boiling curve.

The details of each effect are as follows. CHF and MHF are improved, and HTCs in transition and film boiling are enhanced as ΔT_{sub} increases [50, 51]. With regard to the nucleate boiling regime, influence of ΔT_{sub} cannot be described sweepingly, because it has two opposing effects on HTC: reduction of the number of nucleation sites and bubble departure frequency, and improvement of convective heat transfer owing to a decreased liquid temperature [52].

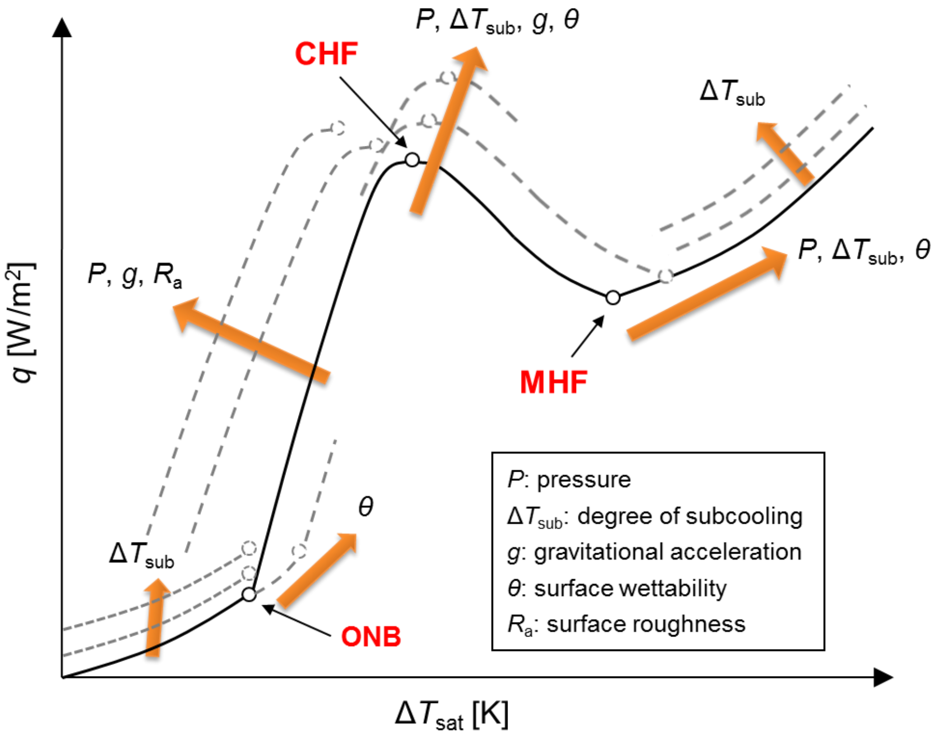

Figure 1.5 Effects of various parameters on boiling curve.

Bubbles hardly detach from a surface under microgravity conditions, resulting in deterioration of HTC and CHF [53-55]. As system pressure rises, ONB is promoted because the increase in the saturation temperature of bubble due to Laplace pressure becomes insignificant. As a result, HTC of nucleate boiling is enhanced [56]. CHF is also improved with increasing pressure in the range up to about one third of the critical pressure; however it decreases monotonically at the higher pressures [57, 58]. HTC in the nucleate boiling regime is enhanced when liquid level is lower than a certain value [59]. The critical liquid level depends on a kind of fluid, which is about 5 mm for distilled water.

Surface roughness, R_a, is closely related to formation of bubble nuclei. Generally, nucleate boiling on a rougher surface show better HTC [60, 61]. However, R_a becomes less influential in the film boiling region where the solid-liquid contact is completely interrupted. Inclination of a heating surface affects boiling performance remarkably. HTC and CHF are minimized with a downward facing surface [62-64]. When a characteristic length of a heating surface is smaller than 20 times of the Laplace coefficient, CHF increases with decreasing characteristic length since liquid supply in the direction along the surface is promoted [65]. HTC becomes greater by using a heating surface with a thickness less than a certain value. The critical thickness differs from material to material [66, 67]. Surfaces with porous [68-70] or fin structures [71, 72] lead to superior HTC and CHF because of an increased nucleation site density, enlarged surface area, and wicking effect. Surface wettability extensively affects boiling curve from ONB to MHF. Its detail are described later in Section 1.4.

In addition to the above, boiling performance can be enhanced by adding external forces such as electric fields [73, 74] and ultrasonic waves [75, 76].

1.3 Surface wettability

The present study deals with boiling on wettability-modified surfaces. In this section, hence, an overview of wetting phenomena and an evaluation method of wettability are introduced.

Molecules inside liquid are attracted by surrounding molecules, and these forces are isotropic. Conversely, molecules at the liquid-gas interface are pulled toward the inner part of the liquid due to a weaker attractive force from the gas phase. This force imbalance gives rise to surface tension [77]. The molecules on the surface also in a state of losing part of its cohesive energy, that is, they has a higher free energy. This surplus is the origin of surface energy.

Figure 1.6 shows the balance of three interfacial forces when a liquid droplet is put on a solid substrate, where σ_{lv}, σ_{sv}, and σ_{sl} are interfacial tensions of the liquid-vapor, solid-vapor, and solid-liquid interfaces, respectively. Based on the force balance in the horizontal direction, the following relation is derived (Young's equation).

$$\cos\theta = \frac{\sigma_{\mathrm{sv}} - \sigma_{\mathrm{sl}}}{\sigma_{\mathrm{lv}}} = \frac{\gamma_{\mathrm{sv}} - \gamma_{\mathrm{sl}}}{\gamma_{\mathrm{lv}}} \tag{1.15}$$

where θ is contact angle and γ is interfacial energy. σ_{lv} is called surface tension and commonly represented by σ. In this article, σ is also used unless otherwise mentioned. As seen from eq.

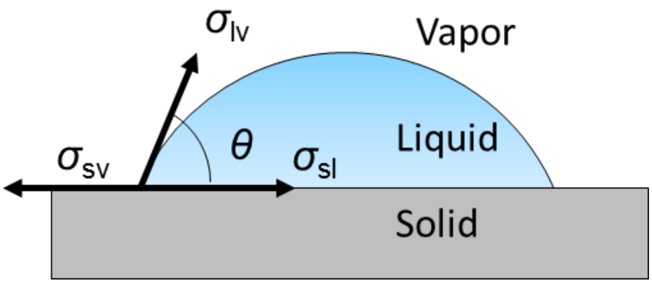

Figure 1.6 Equilibrium of three interfacial forces at the three phase contact point.

(1.15), θ is decided by combination of kinds of liquid and solid. If the liquid has a high-affinity for the solid, θ is small, and vice versa. A degree of wettability is usually represented by using θ due to ease of measurement. In the case of water, for instance, surfaces whose θ is below and above 90^{o} are called hydrophilic and hydrophobic, respectively. In addition, there are terms for the two extreme cases: superhydrophilic ($\theta < 10^{o}$) and superhydrophobic ($\theta > 150^{o}$).

Wettability is in a close connection with surface roughness. Wenzel [78] modified Young's equation, basing on the concept that interface tensions rises with increasing actual surface area, as follows.

$$\cos\theta' = \frac{Rf\,(\sigma_{sv} - \sigma_{sl})}{\sigma_{lv}} = Rf\cos\theta \tag{1.16}$$

where θ and θ' are contact angles of flat and rough surfaces, respectively. Roughness factor, *Rf*, is the ratio of the actual surface area to the projected area. Since *Rf* is necessarily larger than unity, $\theta' < \theta$ if $\theta < 90^{o}$, and $\theta' > \theta$ if $\theta > 90^{o}$. In other words, hydrophilic surfaces become more wettable and hydrophobic surfaces become less wettable as surface roughness increases. Although Wenzel's model is available for a surface having a relatively small roughness, it cannot be applied to a surface with so large *Rf* that the absolute value of the right side of the equation exceeds unity.

Cassie and Baxter [79] proposed a model, shown in Fig. 1.7, for the wetting phenomenon on surfaces with heterogeneous wettability. A contact angle, θ', of a surface, consisting of two

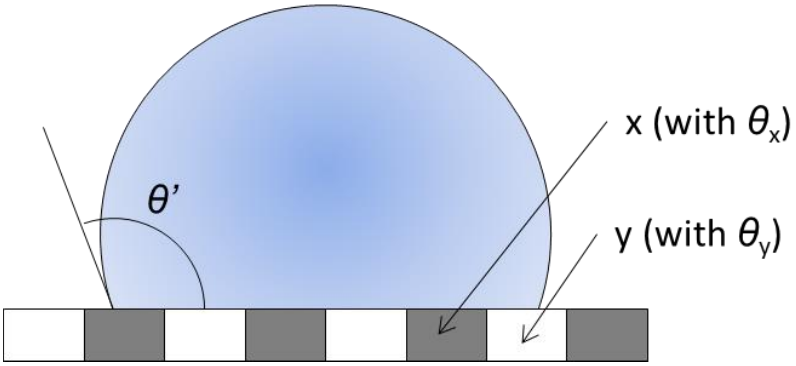

Figure 1.7 Schematic of Cassie-Baxter model.

components of x (with θ_x) and y (with θ_y), is described with the following equation by using their area fraction, f_A : $(1-f_A)$.

$$\cos\theta' = \frac{f_A(\gamma_{x,sv}-\gamma_{x,sl})+(1-f_A)(\gamma_{y,sv}-\gamma_{y,sl})}{\gamma_{lv}} = f_A\cos\theta_x + (1-f_A)\cos\theta_y \tag{1.17}$$

Additionally, they extended their model for the case that one of the components is air (assumed here to be y), and derived the equation by considering θ of air is 180° (because water forms a spherical droplet in the atmosphere), as below.

$$\cos\theta' = f_A\cos\theta_x + f_A - 1 \tag{1.18}$$

This equation means that contact angle becomes large when air is trapped inside grooves on a rough surface without water penetrating into them. The concepts of Wenzel's and Cassie-Baxter's model are essential to fabricate superhydrophobic surfaces.

1.4 Literature survey

Wettability is one of the dominant parameters of boiling phenomenon. Wettability modification of a boiling surface has been extensively studied owing to its great potential for enhancement of boiling performance. In this section, a review of previous works on pool boiling is given while focusing on the following three points: wettability modification, noncondensable gas inside boiling mediums, and system pressure.

1.4.1 Improvement of boiling characteristics through wettability modification

1.4.1.1 Hydrophobic and superhydrophobic surfaces

Research for boiling features on wettability-modified surfaces has a long history. Costello and Frea [80] reported 75% reduction of CHF on a less wettable surface made by a silastic coating, in 1965. Torikai and Yamazaki [81] studied boiling characteristics and the condition of contact between bubbles and a substrate with a uniform hydrophobic surface of a silicone-coated conductive glass, and obtained the following results: (i) The bottom of bubbles was generally in the dry state, namely, no micro-layer beneath the bubbles; (ii) The heating surface was divided into two regions based on bubble behavior. Bubble growth and departures took place frequently on one part, and bubbles hardly detached from the surface while slowly expanding and shrinking on the other. Such boiling behavior was similar to transient boiling; (iii) On the hydrophobic surface, ONB occurred at lower ΔT_{sat} than that on a hydrophilic surface, resulting in an enhanced HTC at lower q. However, HTC in high q region deteriorated, and CHF was significantly reduced. The transient-boiling-like behavior was also observed by Hasegawa et al. [82, 83], who used stainless plate (20×100 mm^2) entirely or partially coated with a silastic adhesive. They subsequently concluded that the boiling mode was essentially nucleate boiling (transient-boiling-like nucleate boiling), because periodic bubble departures occurred, and additionally q increased as ΔT_{sat} rose in the region.

Takegawa et al. [84] investigated a heat transfer mechanism on a hydrophobic surface through observations of bubble behavior with a high-speed camera. According to the study, heat transfer on the hydrophobic surface was dominated by the followings: (i) latent heat transportation of bubbles and (ii) convection induced when departing small bubbles coalesce with surrounding large bubbles. They also reported that both a bubble departure diameter and frequency monotonically became greater with increasing q on the hydrophobic surface, unlike on a normal surface.

Yasukawa [85] revealed that a single bubble grew over the entire surface without an occurrence of the transient-boiling-like nucleate boiling on a narrow hydrophobic surface (with a diameter of 10 mm). Investigating boiling characteristics at ΔT_{sat} up to 200 K, they obtained the following results: (i) At ΔT_{sat} from 6 to 200 K, a growing bubble firstly formed concavity at a lower part of its interface, followed by a partial bubble departure of the above-neck-portion. As a results, a thin vapor film remained on the surface after the departure, which interrupted the solid-liquid contact; (ii) q just monotonically increased as ΔT_{sat} increased, leading to absences of CHF and MHF points on boiling curve; (iii) A gradient of the boiling curve was similar to that of film boiling.

To comprehend the effect of hydrophobicity on boiling characteristics, Torikai et al. [86] carried out experiments by using surfaces (with 10 mm in diameter) applied three different hydrophobic coatings: a Teflon spray (θ = 100°), silicone adhesive (θ = 110°), and silicone cladding (θ = 124°). Boiling curves similar to Yasukawa [85] were obtained on the silicone adhesive and silicon cladding (having the higher hydrophobicities). On the other hand, the Teflon-spray-coated surface was not covered by a single large bubble, whose boiling curve had the same tendency with normal surfaces, that is CHF and MHF points appeared.

Num et al. [87] studied behavior of a single bubble on a smooth hydrophobic surface (Teflon coating, θ = 118-134°) on which an artificial cavity with a diameter of 7 μm was manufactured. They found that, a bubble departure diameter and period on the surface were increased by 7 and 60 times compared with those on a bare silicon surface (θ = 33-46°), respectively, due to an extended contact diameter of the bubble. Furthermore, the bubble departure followed a short "necking" period (where the bubble interface was constricted), and then a tiny vapor bubble was remained on the surface after the detachment. The residue worked as a nucleus of the next bubble. This means an absence of a waiting period in the bubble cycle, which agrees well with the observations conducted by Yasukawa [85] and Torikai et al. [86].

They also performed a numerical simulation by using the level-set method. Although some assumptions were made (θ was kept constant at 120° and evaporation of a micro-layer was omitted), a numerically obtained departure diameter and period showed good agreement with their experimental data within 5 and 7%, respectively.

Takata et al. [88] successfully fabricated a superhydrophobic surface (θ = 150-170°, d = 30 mm) by means of a nickel electroplating containing fine PTFE particles. On such surface, ONB occurred at an extremely low ΔT_{sat} (= 2.15 K), and a vapor film covering the whole surface was formed at $\Delta T_{\mathrm{sat}} \approx 6$ K. HTC of the surface was higher than that of a plain copper surface at $\Delta T_{\mathrm{sat}} \leq 15$ K; however, it tended to deteriorate at higher ΔT_{sat}. Moreover, CHF and MHF points were absent in its boiling curve. Hsu and Chen [89] also obtained the similar results by using a surface with $\theta \approx 149^{\circ}$.

From the above studies, the characteristics of boiling on (super)hydrophobic surfaces are summarized as follows.

- ONB and HTC at lower ΔT_{sat} are enhanced, although HTC at higher ΔT_{sat} and CHF deteriorate.
- A single bubble grows over the entire surface when a narrow or high-hydrophobic heating surface is used. In that case, CHF and MHF points are absent in boiling curve.
- A contact diameter of a bubble expands, resulting in a large bubble departure diameter and period.
- Bubble departure follows a short “necking” period, and then part of vapor is remained on a surface after the detachment. This partial departure leads to a bubble cycle without a waiting period.

1.4.1.2 Hydrophilic and superhydrophilic surfaces

Costello and Frea [80] hydrophilized a surface by depositing scale on the surface through repetition of boiling experiments with tap water. Using the hydrophilic surfaces, they found CHF was improved by 50% compared with a surface without scale. Since then, many studies, utilizing the same hydrophilizing method, were carried out [90-93], and enhancements of MHF, CHF, and HTC of transition boiling were found. Among of those, Maracy and Winterton [93] succeeded to obtain a superhydrophilic surface ($\theta \approx 0^{o}$) by repeating boiling experiments 36 times. They reported CHF was improved with decreasing θ.

Takata et al. [94, 95] prepared a superhydrophilic surface ($\theta \approx 0^{o}$), using the unique characteristics of TiO_2 that it is super-hydrophilized by an irradiation of ultraviolet (UV) light. On the superhydrophilic surface made of a TiO_2-coated cooper substrate, compared with a bare copper surface, about two times improvement of CHF and 100 K increase in MHF temperature were obtained, in addition to enhancement of HTC in the nucleate boiling region. Various fabrication methods were developed in the past decade such as the photocatalytic effect of TiO_2 [96, 97], coating with nano-particles [89, 98-100] and nanowires [101, 102], and surface oxidizing treatments [103, 104]. Although the enhancement of CHF was confirmed in all of those studies, HTC of nucleate boiling increased in some cases [94, 99, 101] and decreased in the others [98, 100, 103]. This is supposed to be because the hydrophilization of a surface brings two opposing effects: the hydrophilic coatings induce micro-nano structures which serve as favorable nucleation sites, at the same time, the coated layer becomes thermal resistance.

Num et al. [105] carried out a detailed investigation of behavior of a single bubble on a superhydrophilic surface ($\theta = 7.5 \pm 2^{o}$) having an artificial cavity (15μm in diameter). On the surface, bubbles maintain their almost-perfect-spherical shape during growing and departure processes. A bubble departure diameter and period are respectively reduced by 2.5 and 4 times, compared with a bare silicon surface ($\theta = 44^{o}$), due to suppressed expansion of the bubble base.

From the above studies, the characteristics of boiling on (super)hydrophilic surfaces are summarized as follows.

- CHF, MHF, and HTC of transition boiling are improved.
- The effect of hydrophobic coatings on HTC in the nucleate boiling region depends on their surface topology and thickness.
- A bubble departure diameter and period decrease because of a small contact diameter of a bubble.

1.4.1.3 Biphilic and superbiphilic surfaces

Superiority of use of a surface with heterogeneous wettability, not uniform hydrophilic or hydrophobic, was shown by Young and Hunmmel [106] in 1964. They made a hydrophilic surface having hydrophobic domains by means of applying a tetrafluoro resin into holes irregularly distributed on a SUS304 surface (supposed to be slightly hydrophilic). On such surface, vigorous bubble departure occurred at $q = 13$ kW/m^2 and $\Delta T_{\mathrm{sat}} = 2$ K (ONB condition on a surface without the resin was $q = 47$ kW/m^2 and $\Delta T_{\mathrm{sat}} = 12$ K). HTC reached 8.6 kW/m^2 at $\Delta T_{\mathrm{sat}} = 8$ K due to promoted liquid circulation by the departing bubbles, which was almost 18-fold of a plain SUS304 surface. Moreover, temporal fluctuation of ΔT_{sat} in the steady state became very small on the heterogeneous wettability surface. All experiments were done at $q <$ 315 kW/m^2 (below CHF) in their study to avoid damage to the surface.

Takata et al. [107] carried out boiling experiments on copper surfaces ($\theta = 92^{\mathrm{o}}$) with dot- or checker-patterned superhydrophobic coating ($\theta = 152^{\mathrm{o}}$). HTC on the patterned surfaces was seven times greater than that on a plain copper surface at moderate heat fluxes. However, HTC deteriorated at $\Delta T_{\mathrm{sat}} > 8$ K, and CHF was reduced. Observing boiling behavior, they also found bubbles were generated from only the coated domains, meanwhile the solid-liquid contact was maintained without bubble nucleation on the uncoated area. Additionally, a departure diameter of a bubble highly depended on a size of the hydrophobic domain since TPCL was pinned at the edge of the hydrophobic spot. In the paper, increase in CHF by replacing the bare copper domain with a superhydrophilic coating was expected. They subsequently confirmed that HTC could be enhanced without reduction of CHF on a patterned surface consisted of TiO_2-sputtered ($\theta = 0^o$) and PTFE-spray-coated ($\theta = 127^o$) domains [108]. In experiments on superhydrophilic surfaces ($\theta = 7^o$) having microscale hydrophobic patterns ($\theta = 110^o$) with 40 μm in diameter and 50 and 200 μm in pitch, conducted by Betz et al. [109], both CHF and HTC were improved by 65 and 100%, respectively, compared with the uniform superhydrophilic surface.

Jo et al. [110] fabricated heterogeneous wettability surfaces with various patterns, and studied the influence of diameter and pitch of hydrophobic spots on nucleate boiling heat transfer. As a result, a higher HTC was obtained on a surface with a larger diameter and smaller pitch at low ΔT_{sat}, although a smaller diameter was preferred and the pitch had a minor effect at high q. They also performed the similar experiment, focusing on CHF [111]. It was consequently revealed CHF was improved as a fraction of hydrophobic area decreased. The bubble departure following the necking, reported by Num et al. [87], was also observed on the heterogeneous surfaces through observation of bubble behavior with a high-speed camera. TPCL of a bubble on a hydrophobic spot with a diameter of 1 mm was pinned at the border between hydrophobic and hydrophilic domains, as with the result of Takata et al. [107]. By contrast, TPCL of a growing bubble was depinned from the border and moved toward the hydrophilic side on a surface with a spot diameter of 100 μm. Even in that case, the hydrophobic spot was remained to be covered with a residual bubble after the detachment.

Betz et al. [112, 113] firstly examined a surface juxtaposing superhydrophobic and superhydrophilic regions (named superbiphilic). They made the surface by means of patterning of a nano-structured silicon oxide substrate with a hydrophobic polymer. The resulting superbiphilic surface ($\theta = 0^o$ and 150-165^o) led to improvement of HTC by one order of magnitude at $\Delta T_{\mathrm{sat}} < 10$ K and 300% at $\Delta T_{\mathrm{sat}} \geq 10$ K, compared with a plain hydrophilic surface (θ = 7-30°). In addition, a two-fold increase in CHF was also obtained.

With progresses in surface treatments and coating techniques, biphilic and superbiphilic surfaces have been fabricated by many different methods. Table 1.1 summarizes their fabrication methods and the maximal HTC and CHF obtained using them.

From the above studies, the characteristics of boiling on (super)biphilic surfaces are summarized as follows.

- ONB occurs at low ΔT_{sat} from hydrophobic domains, meanwhile hydrophilic domains maintain solid-liquid contact. The manipulated bubble generation leads to a superior HTC.
- CHF can be increased by use of a highly-wettable surface for the hydrophilic side.
- TPCL of a bubble is pinned at the border between hydrophobic and hydrophilic regions. As a result, bubble departure diameter depends on a size of the hydrophobic spot. On a surface with a small spot diameter (e.g. 100 μm), however, TPCL moves toward

Table 1.1 Summary of previous works about (super)biphilic surfaces.

Source	Hydrophobic(HPo)	Hydrophilic(HPi)	θ (HPo/HPi) [deg]	HTC [kW/(m·K)]	CHF [kW/m^2]
Takata et al. [108]	PTFE spray	TiO_2 with UV irradiation	120/0	28	760
Jo et al. [111]	Teflon coating	Flat SiO_2	123/54	25	830
Betz et al. [113]	Fluoropolymer coating	Nanostructured SiO_2	150-165/0	155	1300
Zupančič et al. [114]	PDMS*-silica coating	Laser-treated PDMS-silica coating	137.8/<1	51	900
Choi et al. [115]	Polymer coating	Nanostructured ZnO	110/20	12	NM**

*PDMS: Polydimethylsiloxane.

**NM: Not measured.

hydrophilic side. Even in the case, the hydrophobic spot is covered with a residual bubble after the detachment.

- HTC and CHF are affected by a size, pitch, and area fraction of the hydrophobic domains. The best pattern for HTC enhancement depends on q. CHF increases as a fraction of the hydrophobic area decreases.

1.4.2 Effect of dissolved air on boiling characteristics

Takata et al. [88] observed bubble nucleation at $\Delta T_{\mathrm{sat}} = -1.59$ K (namely, T_{w} below the saturation temperature) in subcooled boiling ($\Delta T_{\mathrm{sub}} = 5$ K) on a superhydrophobic surface. Suroto et al. [116] and Tashiro et al. [117] carried out subcooled boiling on biphilic surfaces ($\theta = 0^{\circ}$ and 120-127°), and also found that ONB occurred from a hydrophobic domain at $\Delta T_{\mathrm{sat}} = -4.17$ K under $\Delta T_{\mathrm{sub}} = 20$ K. Moreover, HTC was improved; nevertheless bubbles hardly departed from the hydrophobic spots, which means an absence of the microconvection. They concluded dissolved air in the test liquid (pure water) was considered to cause these phenomena. Shen et al. [118] studied behavior of a single bubble at $\Delta T_{\mathrm{sub}} = 20$ K using a copper surface with a single hydrophobic spot ($\theta = 120$-127°), obtaining the following findings: (i) Periodic bubble departures with an extremely small frequency (four orders of magnitude smaller than that in saturated boiling) occurred at $\Delta T_{\mathrm{sat}} = -2.6$ K; (ii) A temperature inside a bubble, directly measured by a thermocouple, was below the saturation temperature, that is, the bubble contained noncondensable gas; (iii) A partial pressure of the noncondensable gas in the bubble was calculated to be 40 kPa at most. Vakarelski et al. [119] conducted quenching of a superhydrophobicized steel sphere ($\theta > 160^{\circ}$) in a water pool (at 22 $^{\circ}$C). In the experiment, a thin vapor film kept covering the entire sphere surface even after the cooling process was completed. Although they did not mention about noncondensable gas, the test liquid must have contained dissolved air because the water pool was opened to the air. As described above, several unique phenomena, likely caused by dissolved air, were observed on hydrophobic surfaces; however, their details have not been clarified yet.

Now, a review of general influence of noncondensable gas on boiling phenomenon is introduced. In 1966, Behar et al. [120] studied the effect of dissolved nitrogen on subcooled boiling of m-Terphenyl, and found that ONB and HTC were promoted as the gas concentration increased. Torikai et al. [121] also obtained the similar results in water/air system. They additionally proposed a model for the facilitated ONB, based on an assumption that a partial pressure of air inside a critical bubble is in balance with dissolved air in the liquid. In the model, P_{g} in eq. (1.9) (see Sub-section 1.2.2) is derived by using Henry's law,

$$P_{\mathrm{g}} = H_{\mathrm{e}} \cdot C_{\mathrm{g}} \tag{1.19}$$

where H_{e} is Henry constant and C_{g} is solubility of gas. The resulting equation can well explain their experimental data.

Hong et al. [122] devised an experimental apparatus to measure boiling characteristics under a pure subcooled condition in which dissolved air was thoroughly removed. In the apparatus, a reserved tank was connected to the top of a main boiling vessel. By applying heat, sufficient to sustain vigorous boiling, to water in the reserved tank, it was prevented that surrounding air dissolved into the subcooled test liquid in the main vessel during experiments. They carried out subcooled boiling of FC-72 around a platinum wire under the pure and gassy (contained the saturated amount of dissolved air) subcooled conditions. Consequently, remarkable differences between the two conditions were observed: (i) Bubbles immediately condensed after the detachment in the pure subcooled condition, although departed bubbles rose without condensation in the gassy subcooled condition; (ii) ONB and HTC were promoted as ΔT_{sub} increased under the gassy subcooled condition; however, they were independent on ΔT_{sub} under the pure subcooled condition.

In addition to the above, many researchers investigated the effect of dissolved air on boiling features [72, 123-126]. Among of these, ONB at negative ΔT_{sat} was observed in subcooled boiling of FC-72, whose air solubility is very high (48 vol%). Takamatsu et al. [124] performed experiments with a surface having re-entrant cavities under two different air solubilities (3% and 31%). In the case of the high solubility, ONB occurred at $\Delta T_{\mathrm{sat}} \approx -7$ K in $\Delta T_{\mathrm{sub}} = 25$ K. They considered this was because a concentration of dissolved air exceeded the solubility limit in a vicinity of the surface, and the excess air formed a bubble. Rainey et al. [125] found that, on a porous surface, ΔT_{ONB} became -6 K under $\Delta T_{\mathrm{sub}} = 30$ K, and HTC was enhanced due to facilitated bubble generation and departure.

As for boiling of water, to the best of author's knowledge, Wang et al. [127] only observed ONB at negative ΔT_{sat}, excluding Takata et al.'s group [88, 116-118]. In their work, the first bubble nucleation occurred at $T_{\mathrm{w}} = 40$ °C (corresponding to $\Delta T_{\mathrm{sat}} = -60$ K) on superhydrophobic spot ($\theta = 158^{\circ}$), if both the surface and water were not degassed. They, however, focused on bubble nucleation, and HTC was not measured.

As mentioned above, ΔT_{ONB} can take a negative value in conditions favorable for bubble nucleation: subcooled boiling of (i) FC-72 on structured surfaces which easily trap gas and (ii) water on biphilic or hydrophobic surfaces. However, characteristics of subcooled boiling on biphilic surfaces have not been measured in the pure subcooled condition yet. A comparison between the gassy and pure subcooled conditions is needed to understand the effect of dissolved air on boiling features of biphilic surfaces.

1.4.3 Boiling characteristics under sub-atmospheric conditions

System pressure, P, is one of the dominant parameters of boiling, whose influence has been extensively studied. Rallis and Jawurek [128] investigated the effect of pressure on pool boiling of ethanol around a platinum wire, obtaining the following results: (i) As P decreased, ΔT_{ONB} increased, and HTC and CHF deteriorated; (ii) Bubble generation became more unstable with decreasing P. Nucleation sites started to move randomly over a heating surface at P = 29.8 kPa; (iii) At P = 18.8 kPa, finally, boiling mode directly shifted from natural convection to film boiling without a detectable appearance of the nucleate boiling regime; (iv) These results could be explained by increase of $\sigma T_{\mathrm{sat}}/\rho_{\mathrm{v}}L_{\mathrm{lv}}$ in the nucleation theory (eq. (1.3)) with decreasing P.

van Stralen et al. [129] observed behavior of a single bubble in water boiling under sub-atmospheric conditions (2.0-26.7 kPa), using an upward-facing surface with an artificial cavity. A bubble departure diameter and waiting period increased with decreasing P, which reached 150 mm and 100 s, respectively, at P = 2.04 kPa. This intermittent departure of large bubbles caused vigorous temporal fluctuations of T_{w}. The similar behavior was also observed in many other studies [56, 130-134]. Among of these, Nishikawa et al. [56] and Iida et al. [130] respectively revealed that the transition to the intermittent bubble generation occurred at about P = 20 kPa in water boiling on normal metal surfaces (copper and nickel). Niro et al. [132] and McGillis et al. [133] defined the boiling behavior with a waiting period greater than a growth period as “intermittent boiling”.

In summary, ONB, HTC, and CHF are suppressed, and boiling behavior becomes unstable under low pressure conditions.

Incidentally, water is often preferred for a refrigerant of thermosyphons for electronics cooling due to its advantages such as a high thermal conductivity and latent heat of vaporization, non-flammability, and non-toxicity [135-138]. However, a system pressure of the thermosyphon must be lowered since the saturation temperature of water at the atmospheric pressure is higher than a safety temperature of CPUs and LEDs (85 $^{\mathrm{o}}$C in general). Therefore, the deterioration of boiling performance under low pressures may become a serious problem [139]. Moreover, enhancement of nucleate boiling heat transfer at sub-atmospheric pressures is urgently required to meet further increase in heat generation density of electronic devices. In response to the demand, boiling performance in sub-atmospheric condition was improved with various methods such as fin [140, 141] or porous structures [142, 143] and nanofluids [144, 145]. These techniques have been also applied to thermosyphons [146-149].

Now, comparison between the disadvantages of sub-atmospheric boiling and advantages of biphilic surfaces come up with an idea that they are in clear contrast. However, the existing studies about biphilic surfaces mainly focus on the atmospheric condition. The biphilic surfaces have not been applied to pool boiling under low pressures before, to the best of author’s knowledge.

1.5 Research objectives

As described in the previous section, the effect of surface wettability on boiling phenomenon has been extensively studied, and its basic characteristics are being revealed. In subcooled boiling on biphilic surfaces, however, unique phenomena were reported: ONB at negative superheats and heat transfer enhancement with bubbles rarely detaching from the surface. They are supposed to be caused by dissolved air in water. Although the influence of noncondensable gas was thoroughly studied regarding to common metal or structured surfaces, the similar phenomena was not observed. In addition, boiling characteristics on biphilic surfaces have not been investigated in conditions with controlled solubilities of dissolved air.

The literature review in the previous section suggests that deterioration of boiling performance under sub-atmospheric conditions may be overcome by use of biphilic surfaces. Nevertheless, the previous studies focuses on only the atmospheric pressure. Thus, not only heat transfer performance but also fundamental characteristics are not known regarding to sub-atmospheric conditions.

To the response to the above issues, the main objectives of the present work is to study the influence of dissolved air and system pressure on pool boiling from biphilic surfaces. For the former purpose, an experimental apparatus, which is able to thoroughly eliminate dissolved air, has been developed. The effect of dissolved air is experimentally investigated by using the apparatus. In addition, a numerical simulation is performed to understand differences of bubble behavior between environments with and without non-condensable gas, in detail. For the later purpose, heat transfer performance is measured at various pressures using surfaces with different wettability patterns. Moreover, the detailed effect of system pressure on boiling characteristics is studied through an observation of single bubble behavior.

The study about dissolved air will shed light on the remaining unclear aspect of the effect of surface wettability on the boiling phenomenon, although it may not directly contribute to the practical applications. On the other hand, the present work regarding system pressure has a potential to reveal superiority of biphilic surface under low pressure conditions. The obtained results will be beneficial to show guidelines to design the practical devices, resulting in enhancement of electronics cooling, and consequently, contribution to the energy saving.

1.6 Thesis organization

This thesis consists of the following five chapters.

Chapter 1 is the introduction where background, basics of boiling phenomenon and related physics, a review of previous works, and research objectives are described.

In Chapter 2, fabrication method and surface properties of heating surfaces are presented. The details of fabricating techniques used for the surfaces are introduced: TiO_2 sputtering, PTFE spray coating, Polymer-modified halloysite nanotube (P-HNT) coating, Ni/TFEO (tetrafluoroethylene oligomer) electroplating, and photolithography. Results of a contact angle measurement and observation by a laser microscopy and SEM (Scanning Electron Microscope) are shown.

In Chapter 3, investigation about the effect of dissolved air is described. Firstly, an experimental setup, newly developed to control an amount of dissolved air, is introduced as well as degassing and experimental procedures. Two different types of experiments are conducted: measurement of boiling characteristics on a biphilic surface having multiple hydrophobic spots, and observation of single bubble behavior with the help of a high-speed camera. A numerical approach is also taken to obtain information of a distribution of non-condensable gas and surrounding flow field during growth of a single bubble on a biphilic surface. Based on the experimental and numerical results, heat transfer mechanisms of subcooled boiling on biphilic surfaces are considered.

In Chapter 4, experimental investigation of the influence of system pressure is presented. At the beginning, an experimental apparatus and procedures are described. HTCs of biphilic surfaces having different patterns are compared with a plain copper surface at two different pressures (the atmospheric and reduced pressures). The effect of wettability pattern is also considered. Additionally, the boiling characteristics are measured in the pressure range from atmospheric down to 6.9 kPa. Bubble behavior, especially the TPCL motion, under sub-atmospheric conditions is studied in detail by using surfaces with a single hydrophobic spot. Bubble departure diameter and grows rate are also measured.

Finally, the thesis is concluded with future plans in Chapter 5.

Chapter 2

Fabrication of heating surfaces

2.1 Fabricating methods

In the present study, a mirror-finished copper surface is used as reference. TiO_2 sputtering is employed to make superhydrophilic surface, meanwhile, hydrophobic surfaces were fabricated by PTFE spray coating, Polymer-modified halloysite nanotube (P-HNT) coating, and Ni/TFEO (tetrafluoroethylene oligomer) electroplating. In this section, their fabrication methods are described in detail.

2.1.1 Mirror-finished copper surface

The mirror-finished copper surface was made by smoothing the top surface of the heat transfer block with the following procedures. Firstly, a machined surface was dry-polished by using emery papers in the order of #320, #600, and #1000. The surface was subsequently lapped with a lapping machine (ML-180, Maruto instrument). In the lapping process, a medium polishing cloth (MM420, Maruto instrument) and a diamond polishing solution (Maruto instrument), were used at first. After that, the surface was finished by using a soft polishing cloth (MM431, Maruto instrument) and aluminum abrasives with grain sizes from 3.0 to 1.0 μm (Baikalox, Baikowski).

A photo, SEM image, and 3-D image (obtained with a laser microscopy (VK-9710, Keyence)) of the resulting surface are shown in Fig. 2.1. As shown in the figure, the surface

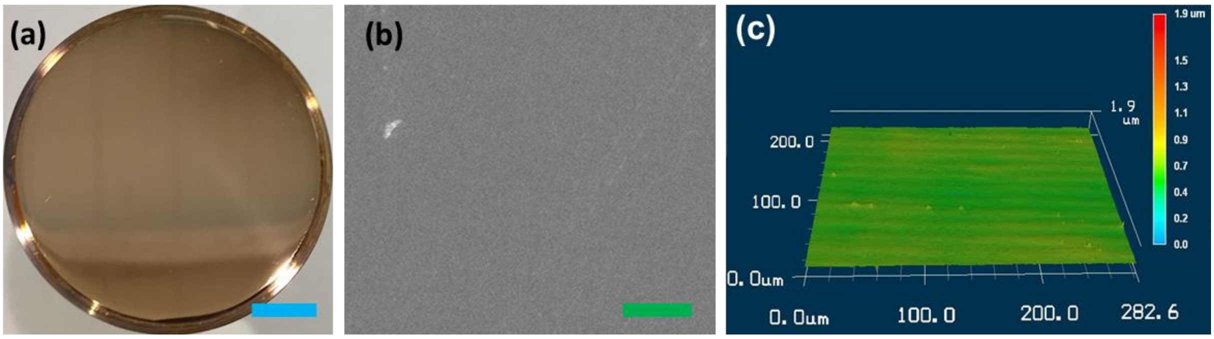

Figure 2.1 The mirror-finished copper surface: (a) photo, (b) SEM image, and (c) 3-D profile. Blue scale bar: 10 mm. Green scale bar: 5 μm.

was nearly free from blemishes. The surface roughness, R_a, was measured to be 0.03 μm from the 3-D image.

2.1.2 TiO_2 sputtering

Superhydrophilic surface was made with the help of the photocatalytic effect of TiO_2. A sputtering technique was employed to fabricate a TiO_2 layer. The procedure was as follows. Firstly, the mirror-finished copper surface, made by the above method, was cleaned ultrasonically in an acetone bath for 10 minutes. Ti and TiO_2 layers were deposited on the surface with the sputtering conditions shown in Table 2.1. The Ti layer was given in order to increase adhesion between the substrate and TiO_2 coating. The sputtering conditions were

Table 2.1 Sputtering conditions.

	Ti	TiO_2
Pressure [Pa]	4	4
Temperature [°C]	RT*	300 or 350**
Gas flow rate [sccm] (Ar/O_2)	10/0	10/5
RF power [W]	100	100
Duration [hr]	4	6 or 8**

* RT: Room temperature.

**The temperature and duration were decided to make thickness of TiO_2 layer 0.6 μm.

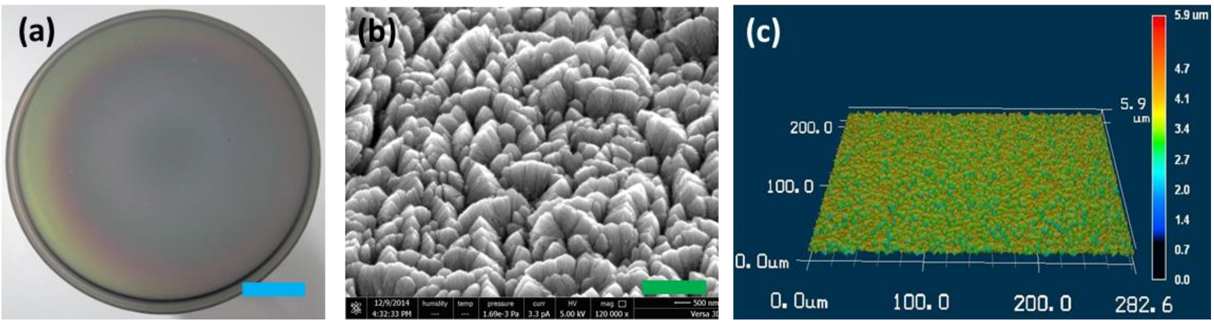

Figure 2.2 The TiO_2 sputtered surface: (a) photo, (b) SEM image, and (c) 3-D profile. Blue scale bar: 10 mm. Green scale bar: 500 nm.

determined so that thicknesses of Ti and TiO_2 layers became 0.4 μm and 0.6 μm, respectively.

Figure 2.2 shows a photo, SEM image, and 3-D profile of the obtained surface. Microstructures were formed on the surface as shown in the SEM image (Fig. 2.2b). R_a was approximately 0.3 μm, which is one order of magnitude larger than that of the mirror-finished copper surface.

2.1.3 PTFE spray coating

The PTFE spray coating (FC-103, FINE CHEMICAL JAPAN) is used to obtain a hydrophobic surfaces. The coating procedure was as follows. At first, a base substrate (the mirror-finished copper or TiO_2-sputtered surface) was cleaned with the same manner as above. The coating agent was sprayed on the surface at 20 cm distance for five seconds. The same process was repeated two more times with an interval of 30 minutes for natural drying. After the last spray, the coated surface was left in the air for one hour in order to adequately dry the coating. Finally, the sample was baked at temperatures above 260 ^{o}C for 30 minutes in an electric furnace under N_2 flow to increase its durability.

A phot of the resulting surface is shown in Fig. 2.3a, where the coating is applied on only the center region of 30 mm. Although the thickness of the layer was not stable because the

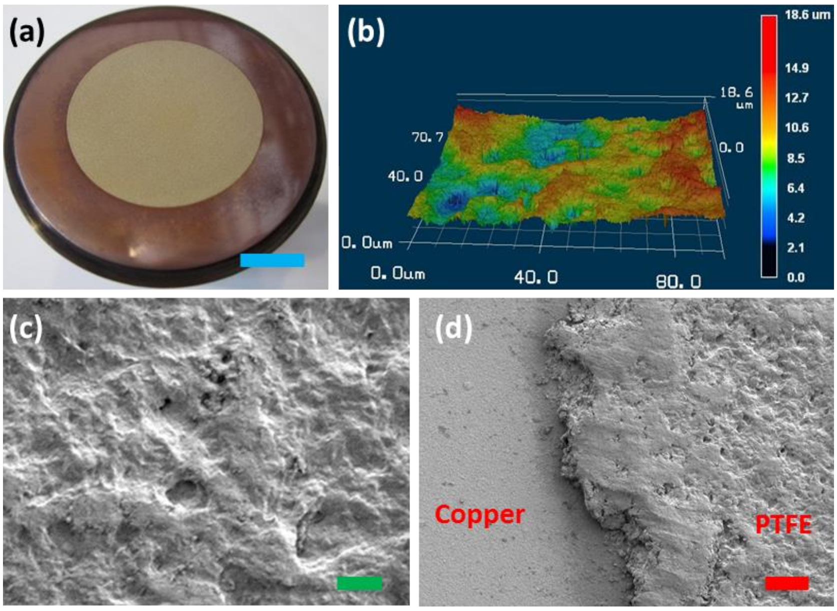

Figure 2.3 (a) A photo and (b) 3-D profile of the PTFE-spray-coated surface. Blue scale bar: 10 mm. SEM images of (c) the center region of the coating and (d) the border with a copper substrate. Green scale bar: 10 μm. Red scale bar: 30 μm.

coating was manually operated, it was approximately 20 μm. As shown in the 3-D profile (Fig. 2.3b), the coated surface was very rough, whose $R_a \approx 3$ μm. In addition, the surface had many cavities with a diameter of several μm (Fig. 2.3c), which was supposed to work as a good nucleation site. A masking tape for printed circuit boards was used to pattern the coating. The wettability pattern was clearly defined as shown in Fig 2.3d.

2.1.4 P-HNT coating

This coating agent (provided by the Institute for Materials Chemistry and Engineering in Kyushu University) consists of a fluorine solvent (AK225, Asahi Glass) containing 3.0 w% of HNTs, with 1-15 μm in length and 50 nm in diameter (SIGMA-ALDRICH), modified by the polymer of P(FA-C8-co-DOPAm). After the ultrasonic cleaning in acetone, a substrate was coated by drop-coating of the agent. The coated surface was dried in the atmosphere more than one minute, and then, ultrasonically cleaned in acetone for five minutes.

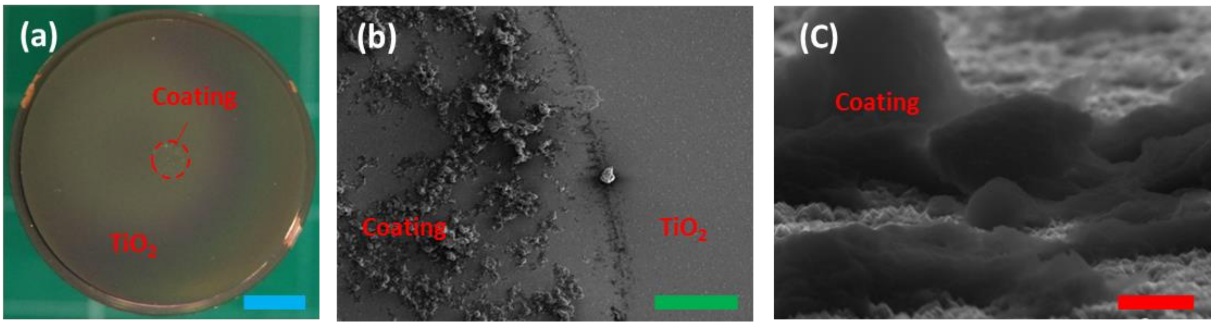

Figure 2.4 (a) A photo of a TiO_2 surface coated with the Polymer-modified HNT (P-HNT), whose diameter is 6 mm. Blue scale bar: 10 mm. SEM images of P-HNT coating taken from (b) the top and (c) an inclined angle. Green scale bar: 50 μm. Red scale bar: 1 μm.

Fig 2.4a shows a photo of TiO_2 surface having a hydrophobic spot ($\varphi = 6$ mm) made by the P-HNT coating. The red circle indicates the coated area. According to the SEM images (Fig. 2.4b and c), aggregates of P-HNT were spattered on the surface, whose height was 3 μm at most. This coating was easy to make and also has high hydrophobicity. However, it was available only for subcooled boiling at low heat fluxes due to its low durability. The same manner as that of the PTFE spray coating was used for patterning.

2.1.5 Ni/TFEO electroplating

Ni/TFEO electroplating (Tef metal coat, Nomura plating) uses a Ni plating solution containing 35 vol% of fine TFEO particles with a mean diameter of 5 μm. This plating can be patterned by photolithography, and the smallest spot diameter which can be made is 0.5 mm. Photoresist masks for the patterning were fabricated by the following procedure.

(1) Clean the mirror-finished copper surface in an ultrasonic bath with acetone for 10 minutes.

(2) Set the block on the sample stage of a spin coater (a special holder was prepared to support the block).

(3) Apply a positive-type photoresist (PMER P-HA1300PM, TOKYO OHKA KOGYO),

brought back to the room temperature in advance, on the surface.

(4) Perform spin-coating at 1400 rpm for 20 seconds.

(5) Pre-bake the sample on a hot plate at 110 ^{o}C for nine minutes.

(6) Leave the sample in the atmosphere for one hour.

(7) Expose the sample to UV light while putting a glass mask, having an intended pattern, on the surface. The optimum exposing time was determined by try and error because it depended on a pattern of the mask.

(8) Develop the pattern by immersing and shaking the surface in a developing solution (PMER P-7G, TOKYO OHKA KOGYO), maintained at 23±0.5 ^{o}C, for six minutes.

(9) Rinse the sample with pure water, and then, dry it with air blow.

A photoresist mask with a thickness of about 30 μm was fabricated with the above process. After the electroplating was carried out by an outside manufacturer, the following procedure was taken to complete the coating process.

(10) Remove the photoresist by immersing the surface in a dissociation solution (Stripper-104, TOKYO OHKA KOGYO), maintained at 70 ^{o}C, for 20 minutes.

(11) Rinse the sample with pure water for two minutes.

(12) Bake the sample in an electric furnace under N_2 flow at 280 ^{o}C for two hours in order to harden the plated layer.

Figure 2.5a shows a picture of a copper surface having hydrophobic spots (with a diameter and pitch of 0.5 and 1.5 mm, respectively) made by the Ni/TFEO electroplating. As shown in the 3-D profile and SEM image, TFEO fine particles formed micro-structurers on the plated surface. A surface roughness and thickness of the plated layer were 0.77 and 10 μm, respectively. The coated surface showed good hydrophobicity owing to combination of the micro-structures and a low surface energy of TFEO. The border between the hydrophobic and hydrophilic areas was clearly defined by photolithography, as shown in Fig. 2.5d.

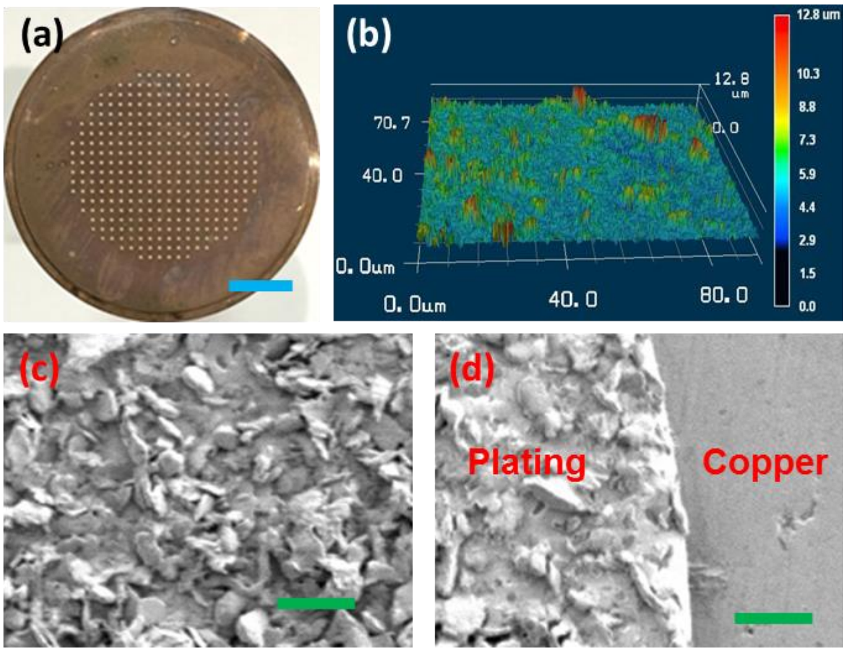

Figure 2.5 (a) A photo of a copper surface spotted with the Ni/TFEO electroplating. Blue scale bar: 10 mm. (b) A 3-D profile and (c), (d) SEM images of the plated surface. Green scale bar: 10 μm.

2.2 Contact angle measurement

Contact angles of the above five surfaces were measured by the $\theta/2$ method (refer to Section A-2 for details). The results are summarized in Table 2.2 with surface roughness, film thickness, and fabrication method. Note that the static contact angle on a horizontal surface was measured in the present study. Contact angle, θ, in this thesis means the static contact angle unless otherwise mentioned.

Table 2.2 Summary of surface properties and fabrication methods.

Surface	θ [°]	R_a [μm]	Thickness [μm]	Fabrication method
Copper	60-80	0.03	-	Lapping process
TiO_2	≈ 0	0.3	1	Sputtering
PTFE	120-127	3	≈ 20	Spray coating
P-HNT	140-150	-	≤ 3	Drop coating
Ni/TFEO	140-150	0.77	10	Electroplating

Chapter 3

Effect of dissolved air on subcooled boiling

3.1 Experimental apparatus

In the present study, two experimental apparatuses, open and closed type, were prepared to control an amount of dissolved air. Details of the apparatuses are described in this section.

3.1.1 Open type apparatus

An open type experimental system, shown in Fig. 3.1, consisted of a boiling apparatus (1-11 in Fig3.1) and peripheral equipment (12-21). A boiling vessel (8) was made of a Pyrex glass tube with 120 mm in inner diameter and 450 mm in height. The vessel was surrounded by four insulation boards (10), and one of them had an optical window (11). A temperature of the space between the vessel and insulation was maintained equal to a bulk liquid temperature by using an air heater (17) (PJ-216A, ISHIZAKI ELECTRIC MFG) connected to a temperature controller (18) (TJA-550K, AS ONE). A pipe, coming out of the top of the vessel, was connected to a pressure gage (12) (DG-923N-A, Tokyo aircraft instrument) and a vacuum pump (13). An oilless scroll pump (DVSL-100C, ANEST IWATA), having a high ability of vapor discharging, was chosen for the purpose of a long-term degassing.

Coil-shaped sheath heaters (3, 5) (SWD1070, Hakko Electric) were placed at upper and lower parts inside the boiling vessel, whose input was supplied by a slidac (14) (RSA-10, Tokyo Rikosha). A heat transfer block (9) was heated with the same heater (4); however, heat input

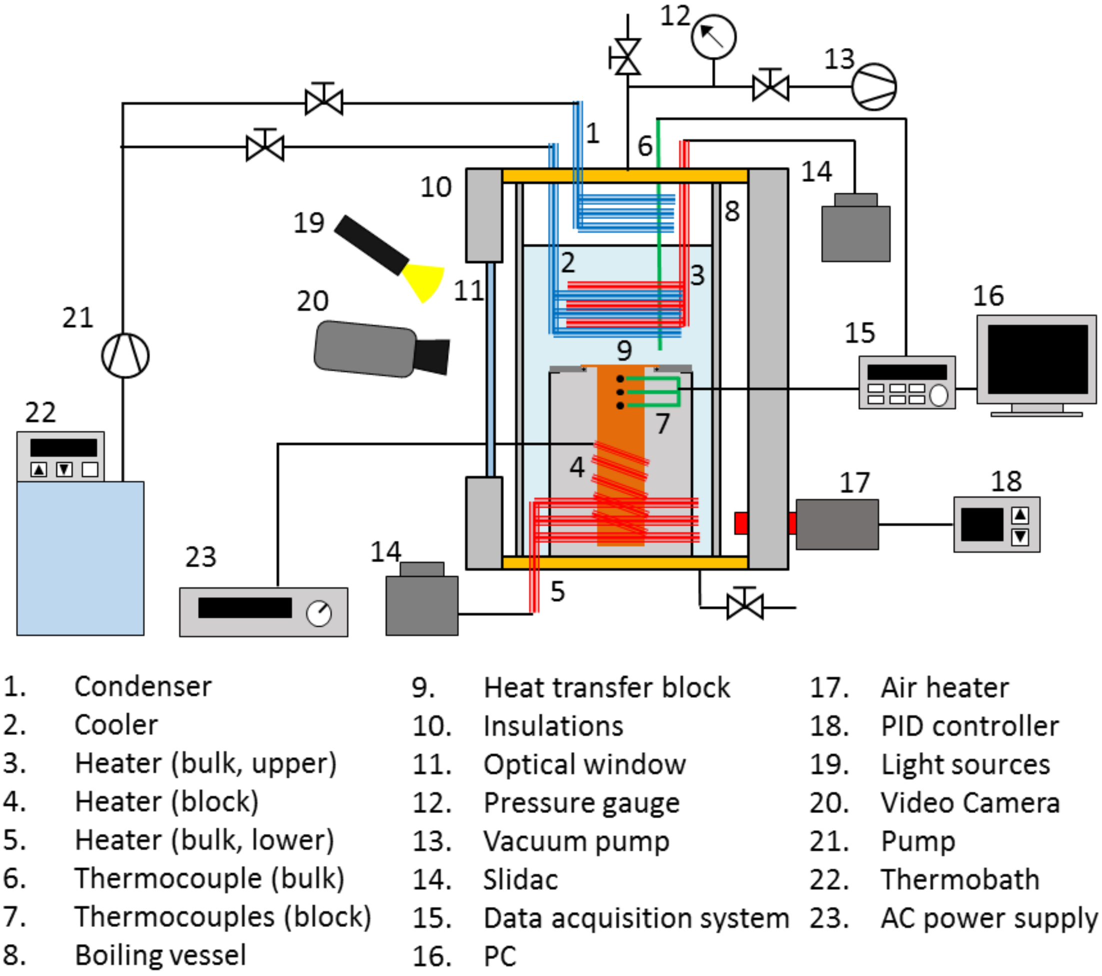

Figure 3.1 A schematic of the "open" type experimental system, which consists of a pool boiling apparatus (1-11) and peripheral equipment (12-23).

was controlled by an AC power supply (23) (SR-1.5K, Matsusada Precision). The block was wrapped by glass wool for insulation. Both condenser (1) and cooler (2) were made of a coiled copper tube. Temperature-conditioned water was supplied to them from a thermobath (22) (BH302, Yamato Scientific) by a pump (21) (WDP-1A, AS ONE).

Temperatures of the bulk water and heat transfer block were measured with K-type sheath thermocouples (6, 7) with a diameter of 1 mm. Outputs of the all thermocouples were stored in a PC (16) through a data acquisition system (34970A, Agilent). A sampling rate and measurement accuracy were 4.2 Hz and ±0.2 K, respectively. Boiling behavior was captured by a normal video camera (HDR-9J760V, SONY) with a light source (19) of LED light. In addition, single bubble behavior was observed by a high-speed camera (v4.3, PHANTOM) with a high brightness metal halide lamp (LS-M210, Sumita Optical Glass).

3.1.2 Closed type apparatus

A boiling vessel should be enclosed to prevent that the surrounding air dissolves into a test liquid during an experiment. However, a devised apparatus is needed to realize subcooled conditions with a lowered concentration of dissolved air because a fluid in a rigid vessel necessarily reaches the saturation state after a degassing by just closing up the vessel. A closed type apparatus was, hence, designed as shown in Fig. 3.2 by referring that of Kim et al. [150]. Peripheral equipment was the same with that of the open type apparatus.

The biggest difference from the open type apparatus was that a rubber bellows (14 in Fig. 3.2) (with a maximal volume of two liters) was connected to the bottom of the boiling vessel. The bellows was put in an enclosed chamber made of a Pyrex glass tube (13). A system pressure in the boiling vessel could be controlled by adjusting an inner pressure of the chamber.

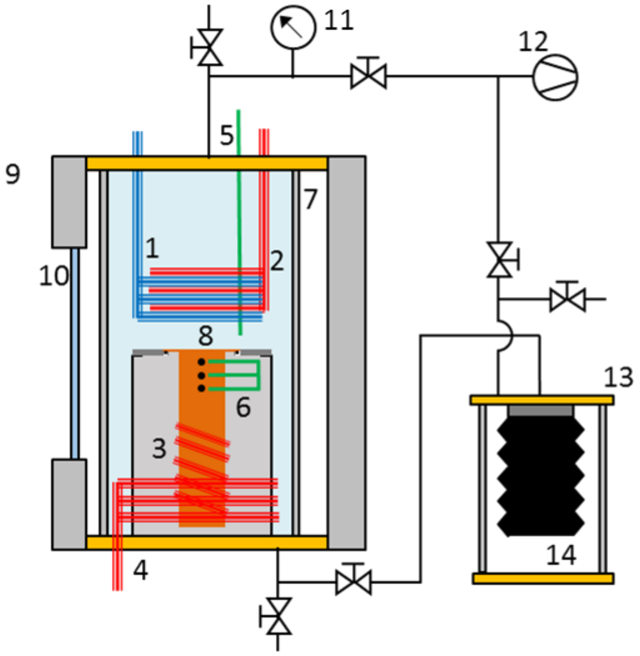

1. Cooler
2. Heater (bulk, upper)
3. Heater (block)
4. Heater (bulk, lower)
5. Thermocouple (bulk)
6. Thermocouples (block)
7. Boiling vessel
8. Heat transfer block
9. Insulations
10. Optical window
11. Pressure gauge
12. Vacuum pump
13. Vacuum camber
14. Rubber bellows

Figure 3.2 A schematic of the “closed” type experimental apparatus.

In addition, the boiling vessel and connections were hermitically sealed to prevent leakage. Since the vessel was totally filled with liquid water, namely no vapor space, the condenser was not used.

3.1.3 Heat transfer block

Figure 3.3 shows a schematic of a heat transfer block. The block was fashioned from a copper cylinder 30 mm in diameter and 100 mm in length. The block had an outer skirt with a diameter of 50 mm at the top to suppress undesirable bubble generation at the gap between the boiling surface and the surrounding stainless plate. A thickness of the outer skirt was made very thin (0.3 mm) to minimize heat conduction from the heating area. The edge of the outer skirt was hold with the two stainless plate through the intermediary of an O-ring for the purpose of sealing. The lower part of the block (80 mm) was tapered for mounting

Three holes with a diameter of 1.1 mm and depth of 15 mm were drilled on the side of the block for temperature measurement with thermocouples. Positions of the holes were approximately 3, 5, and 13 mm from the top surface, respectively.

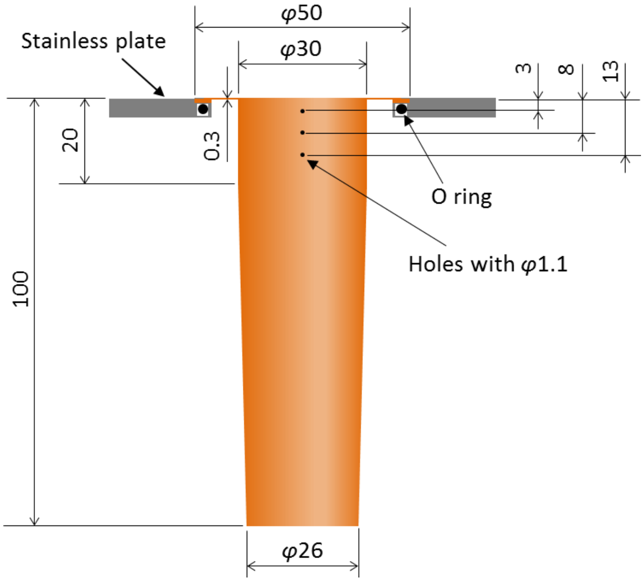

Figure 3.3 A schematic of the heat transfer block.

3.2 Experimental procedures and data reduction

In the present study, experiments were conducted under two contrasting conditions, gassy subcooled and pure subcooled, to investigate the influence of dissolved air. Different degassing procedures were taken for the respective conditions. Two kinds of experiments were conducted: measurement of boiling characteristics on a biphilic surface having multiple hydrophobic spots, and observation of single bubble behavior with the help of a high-speed camera. In this section, the degassing procedures, procedures of the boiling heat transfer and single bubble experiment, and data reduction method are described.

3.2.1 Degassing

3.2.1.1 Gassy subcooled condition

The open type apparatus was used in the gassy subcooled condition. Degassing was carried out with the following means. Firstly, the boiling vessel was evacuated, and then, de-ionized water was fed into the vessel from the bottom with the help of the pressure difference. After the vessel was opened to the air, the liquid pump was turned on to circulate cooling water though the condenser. The surrounding space of the vessel was heated up to 100 ^{o}C by the air heater. The water in the vessel was brought to a boil by applying a heat input of 60 W to each of the bulk heaters. Then, the boiling state was maintained for 30 minutes to remove dissolved air contained in the water.

As mentioned before, however, the surrounding air could come into the vessel during an experiment. Therefore, it was impossible to eliminate the influence of dissolved air even if the test liquid had been thoroughly degassed before the experiment.

3.2.1.2 Pure subcooled condition

Experiments under the pure subcooled condition were performed with the closed type apparatus. A degassing procedure was as follows, which is also shown in Fig. 3.4. The steps a-f of the procedure correspond to Fig. 3.4a-f, respectively.

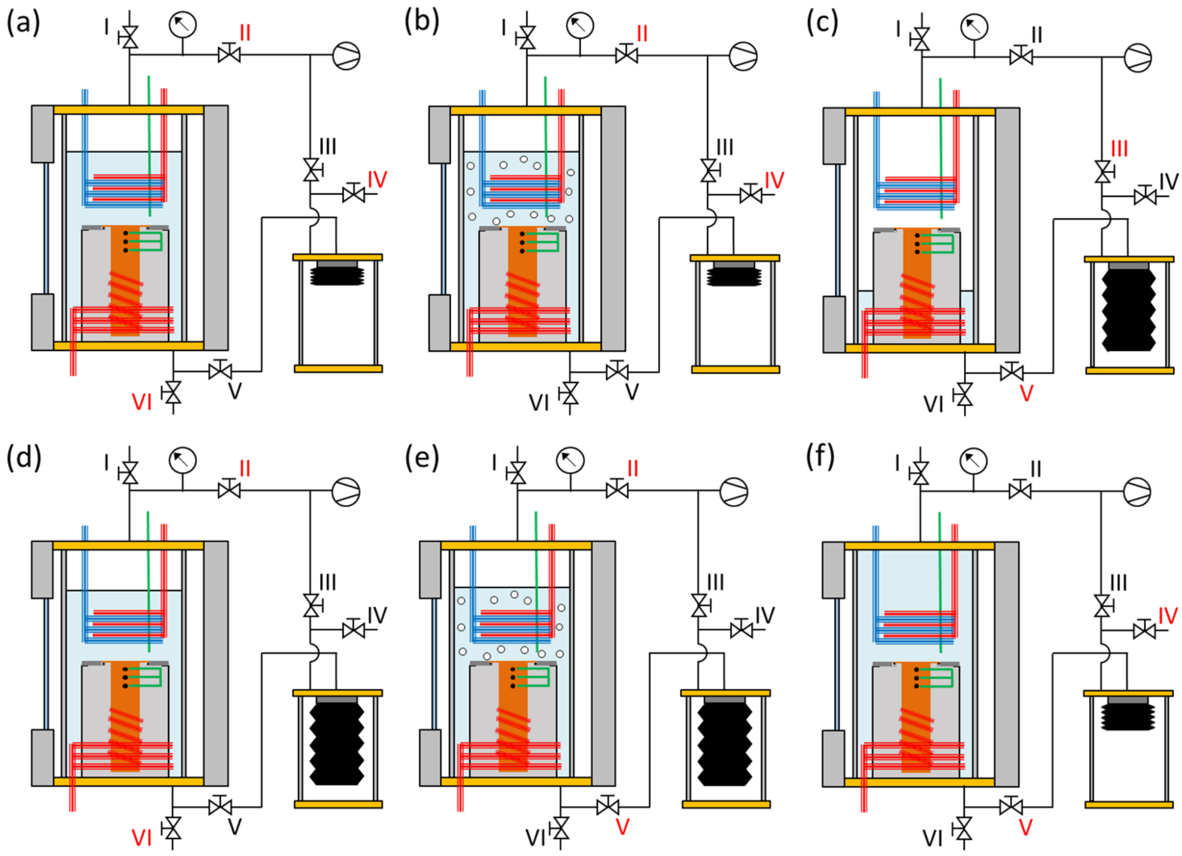

Figure 3.4 Schematic of the degassing procedure in the pure subcooled condition. A red-coloring of the valve numbers (I-VI) means the valve being opened.

(a) Introduce 2.5 liters of de-ionized water into the boiling vessel by turning on the vacuum pump and opening valve II and VI. As an initial sate, the bellows is shrunk and valve IV is opened.

(b) Evacuate the boiling vessel continuously for one hour after closing valve VI. During this period, dissolved air comes out of the water due to reduction of a partial pressure of air in the vapor phase.

(c) Close valve II and IV, and then, open valve V. After that, depressurize the vacuum chamber by opening valve III under a condition where the chamber is placed lower than the boiling vessel. As a result, water in the vessel moves into the bellows because of the water head difference.

(d) Introduce 2 liters of de-ionized water into the boiling vessel again by opening valve II and VI after closing valve III and V.

(e) Evacuate the test liquid for one more hour with valve V opened after closing valve VI. Meanwhile, adjust an inner pressure of the vacuum chamber so that the bellows does not stretch.

(f) Open the chamber to the air by opening valve IV after closing valve II. Consequently, the bellows shrinks, and a system pressure in the boiling vessel is pressurized up to the atmospheric pressure.

Subcooled conditions at the atmospheric pressure could be sustained while preventing inflow of the surrounding air with the above procedure. The system pressure was stabilized within ±0.1 kPa through experiments because increase and decrease in a volume of the test liquid, due to temperature change or bubble generation, was accumulated by the bellows. During an experiment, the bellows was placed at the similar height with the boiling vessel.

3.2.1.3 Estimation for an amount of dissolved air

Solubility of gases in liquids can be estimated with Henry's law (eq. (1.19)). The solubility of dissolved air in 80 °C water is derived as follows by using a Henry constant ($H_\mathrm{e} = 10.43\times10^9$ Pa) and saturation vapor pressure ($P_\mathrm{v,sat} = 48.93\times10^3$ Pa) at the same temperature (refer to Section A-3 for details).

$$C_\mathrm{g} = (101.32\times10^3 - P_\mathrm{v,sat})/H_\mathrm{e} = \{(101.32-48.93)\times10^3\}/(10.43\times10^9)$$

$$= 5.02\times10^{-6}\ \text{[mol/mol]} = 2.71\times10^{-7}\ [\text{mol/m}^3]$$

In the gassy subcooled condition, the surrounding air dissolves into the test liquid which has been degassed before an experiment. A supply rate of the dissolved air is, thus, roughly estimated by the one dimensional diffusion equation,

$$\frac{\partial C_g}{\partial t} - D\frac{\partial^2 C_g}{\partial z^2} = 0 \tag{3.1}$$

In the above equation, solubilities, C_g, are assumed to be 2.71×10^{-7} mol/m^3 and 0 mol/m^3 at the liquid surface (z = 0 mm) and heating surface (z = 120 mm). A diffusivity of air, D_2, at T_2 = 80 °C can be obtained from the Stokes-Einstein equation,

$$D_2 = \frac{T_2}{T_1}\frac{\eta_1}{\eta_2}D_1 \tag{3.2}$$

where D_1 is determined to be 2.05×10^{-9} m^2/s based on diffusivities of oxygen and nitrogen (2.01×10^{-9} and 2.20×10^{-9} m^2/s [151]) and their volume ratio at T_1 = 25 °C. Viscosities of η_1 and η_2 are 893.1 and 354.4 μPa･s, respectively. As a results, $D_2 = 6.12\times10^{-9}$ m^2/s is derived. The solution of eq. (3.1) with the obtained D_2 shows that only 2.41×10^{-10} mol/m^3 of dissolved air is supplied on the surface even 24 hours later. However, as mentioned later in Section 3.4, cyclic bubble departures with frequencies of a several minutes were observed in the gassy subcooled condition, which contradict the calculation. It is, consequently, supposed that natural convection of the liquid dominates the supply of dissolved air. Hence, an amount of dissolved air in water is assumed to correspond to the saturation solubility at a given water temperature in the gassy subcooled boiling.

In the pure subcooled condition, on the other hand, an amount of dissolved air is calculated based on a partial pressure of air in the vapor phase after the degassing process. The vapor pressure was measured between steps e and f in the above degassing procedure (with all valves closed), which was about 1 kPa higher than the saturation pressure at the water temperature. Thus, the solubility corresponding to an air partial pressure of 1 kPa at a normal temperature (25 °C) is estimated as follows, by using the Henry constant (H_e = 7.26×10^9 Pa) at the temperature.

$$C_\mathrm{g} = (1\times10^3)/(7.26\times10^9) = 1.38\times10^{-7} \quad \text{[mol/mol]}$$

The same solubility was maintained after a test liquid is heated up, because entering and exiting of air is prevented in the closed type apparatus. Therefore, the amount of dissolved air in the pure subcooled condition is reduced to 2.7% of that in the gassy subcooled boiling at $\Delta T_{\mathrm{sub}} = 20$ K.

3.2.2 Boiling heat transfer experiment

As for the boiling heat transfer experiment, procedures were the same between the gassy and pure subcooled conditions. After the respective degassing processes, a bulk temperature was adjusted to coincide with an intended subcooling. A heat input to the heating block was stepwisely increased, meanwhile the bulk temperature was kept constant within ±0.5 °C. Outputs of all the thermocouples and boiling behavior were recorded after steady state was reached at each of the heat inputs. When a temperature fluctuation for 200 seconds became less than ±0.5 K without monotonic temperature increase/decrease, the boiling behavior was regarded as the steady state.

Temperature measurements of each thermocouple over 50 data points (about 12 seconds) were used for data analysis. Heat flux, q, and wall temperature, T_{w}, were calculated based on a simple one-dimensional steady-state heat conduction, where a temperature gradient in the block was obtained by least squares approximation of the measured values.

$$q = -\lambda_{\mathrm{c}} \frac{dT}{dx} \tag{3.3}$$

$$T_{\mathrm{w}} = T_1 - \frac{q x_1}{\lambda_{\mathrm{c}}} \tag{3.4}$$

$$\frac{dT}{dx} = \frac{3\sum_{i=1}^{3} T_i x_i - \sum_{i=1}^{3} T_i \cdot \sum_{i=1}^{3} x_i}{3\sum_{i=1}^{3} x_i^2 - \left(\sum_{i=1}^{3} x_i\right)^2} \tag{3.5}$$

where λ_{c} is thermal conductivity of copper, x_i is position of the thermocouples with subscripts 1, 2, and 3 corresponding to the thermocouple positions of about 3, 8 and 13 mm, respectively. Wall superheat, ΔT_{sat}, was derived from the following equation.

$$\Delta T_{\mathrm{sat}} = T_{\mathrm{w}} - T_{\mathrm{sat}}\left(P_{\mathrm{atm}}\right) \tag{3.6}$$

where the saturation temperature at the atmospheric pressure was used as T_{sat} in both the gassy and pure subcooled conditions.

3.2.3 Single bubble experiment

Experiments using surfaces having a single hydrophobic spot were carried out to measure a bubble departure diameter and frequency in addition to a temperature profile inside a bubble. Bubble behavior was observed by the high speed camera on which a telescope lens (AF Nikkor 180 mm f/2.8D IF-ED, Nikon) was mounted. The bubble departure diameter was measured as an average of horizontal and vertical widths of a departed bubble, as shown in Fig. 3.5a. A ruler, put above the hydrophobic spot, was captured after each experiment for calibration of length scale (Fig. 3.5b).

Figure 3.6 shows a device for measurement of a temperature profile inside a bubble. A K-type thermocouple was encased in a SUS316 pipe with MgO thermal insulation. Because the one end of the stainless pipe was supported by a three-axis linear translation positioner, the tip of the thermocouple could be precisely moved in three-dimensions. The thermocouple was

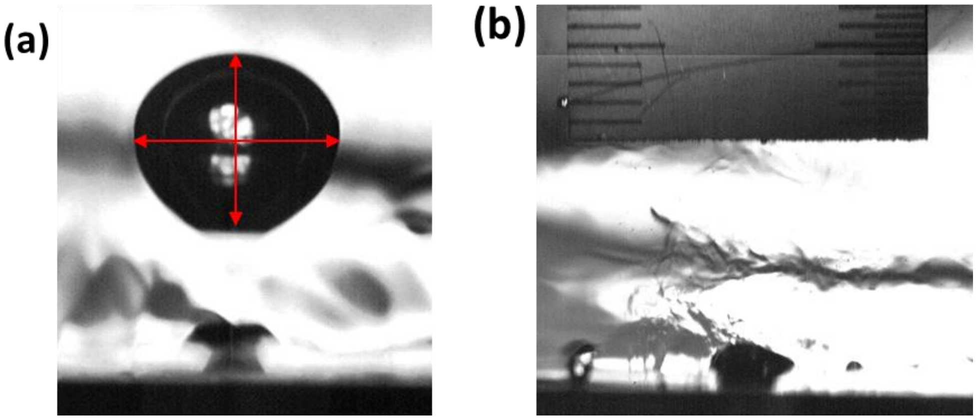

Figure 3.5 (a) A departed bubble captured by the high speed camera. A bubble departure diameter was measured as an average of vertical and horizontal widths of the bubble. (b) Length scale of captured videos was calibrated by capturing a ruler putted above the hydrophobic spot.

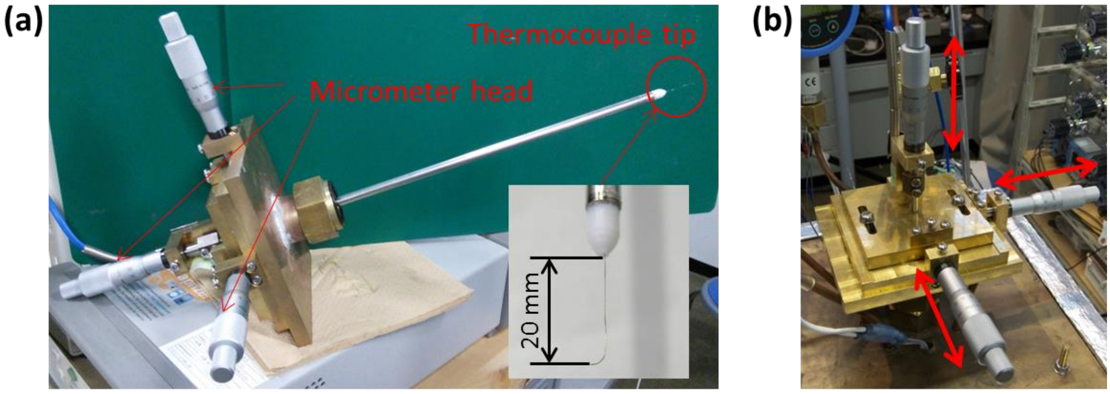

Figure 3.6 (a) A device for measurement of a temperature profile inside a bubble, which can be mounted onto the boiling vessel (b). The tip of the thermocouple can be precisely moved in three-dimensions with the help of a three-axis linear translation positioner.

chosen very thin (150 μm in diameter) and its tip was bent horizontally to minimize the effect of heat conduction along itself. The devise could be mounted onto the boiling vessel. O-rings were placed between all the sliding surfaces, which enable to use the device with the closed type apparatus.

3.3 Boiling heat transfer characteristics

In this section, the influence of dissolved air on heat transfer characteristics is described. Experiments were conducted by using a mirror-finished copper surface and biphilic surface at a subcooling of 20 K. The present study focuses on ONB and HTC at the low heat flux region, and thus, CHF was not measured.

3.3.1 Mirror-finished copper surface

Firstly, experiments with a mirror-finished copper surface were carried out to obtain reference data, as well as to confirm the validity of the present apparatus. Boiling characteristics were measured twice for each of the gassy and pure subcooled conditions. The surface was polished before each experiment to eliminate influence of surface contamination.

Figure 3.7 shows obtained boiling curves. The arrows in the figure correspond to the ONB points, and ΔT_{ONB} are summarized in Table 3.1. The solid line indicates the calculations based on Lloyd and Moran's correlation for the natural convection heat transfer on upward facing surfaces at the corresponding condition [152].

$$Nu = 0.54 Ra^{1/4} \quad (10^4 \leq Ra \leq 10^7) \tag{3.7}$$

$$Nu = 0.15 Ra^{1/3} \quad (10^7 \leq Ra \leq 10^{10}) \tag{3.8}$$

where Nu is the Nusselt number and Ra is the Rayleigh number. A characteristic length is a ratio of surface area to peripheral length, namely, one-fourth of a diameter of the heating

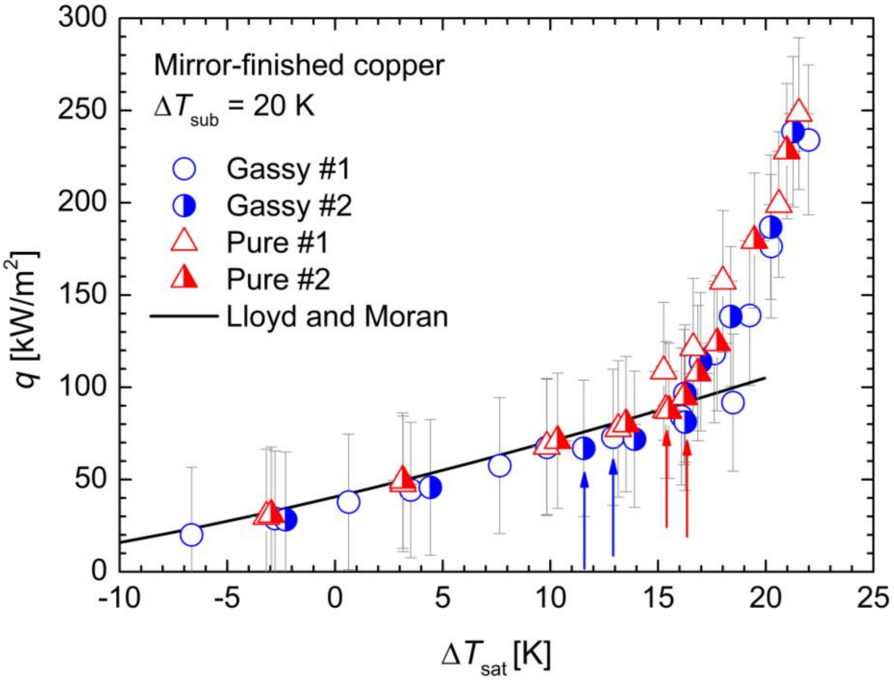

Figure 3.7 Comprasion of boiling curves of the mirror-finished copper surface at $\Delta T_{\mathrm{sub}} = 20$ K under the gassy and pure subcooled conditions. The arrows indiacte ONB, and the black solid line is calculation of Lloyd and Moran's correlation, eq. (3.7) and (3.8).

Table 3.1 ΔT_{ONB} [K] corresponding to Fig. 3.7.

Condition	#1	#2
Gassy	12.9	11.5
Pure	15.4	16.2

region (7.5 mm). Although the error bars of ΔT_{sat} are hidden behind the symbols, their values are ±0.33-0.35 K.

ΔT_{ONB} in the pure subcooled condition are 2.5-4.7 K higher than those in the gassy subcooled condition, which means ONB is promoted by dissolved air as with the previous study [121]. HTC is improved just after ONB in the pure subcooled condition. On the other hand, increase in HTC is not triggered by ONB in the gassy subcooled condition, and started at ΔT_{sat} close to ΔT_{ONB} of the pure subcooled boiling. The boiling curves in the both conditions almost overlap among them in not only the natural convection region but also the nucleate boiling region.

Through these experiments, the validity of the apparatus is confirmed since boiling curves in the natural convection region agree well with the correlation, in addition to the results in the same condition show good repeatability.

Figure 3.8 shows comparison of boiling behavior in the two conditions at $\Delta T_{\mathrm{sub}} = 20$ K and $\Delta T_{\mathrm{sat}} \approx 13$, 16, and 22 K, where an image of $\Delta T_{\mathrm{sat}} \approx 13$ K in the pure subcooled condition is omitted because it is before ONB. Only one tiny bubble is generated at ONB in the gassy subcooled condition ($\Delta T_{\mathrm{sat}} \approx 13$ K in Fig. 3.8a). The number of nucleation sites does not increase as the heat input is raised at $\Delta T_{\mathrm{sat}} < 16$ K. Subsequently, the nucleation site density and bubble departure diameter tend to increase at $\Delta T_{\mathrm{sat}} \approx 16$ K. Conversely, multiple bubbles depart from the surface just after ONB in the pure subcooled condition. From the results, it is suggested that the ONB under the gassy subcooled condition is caused by non-condensable gas trapped inside a cavity in advance, and nucleation of pure vapor bubbles starts at $\Delta T_{\mathrm{sat}} \approx 16$ K. By solving the nucleation theory (eq. (1.3)) with ΔT_{ONB} in the pure subcooled condition ($\approx$ 16 K), the maximal diameter of cavities on the heating surface is estimated to be 0.93μm. ΔT_{ONB} of the same cavity in the gassy subcooled condition is derived to be 9.8 K by using Torikai's model [121] (see Sub-section 1.4.2). The calculation agrees with the experimental

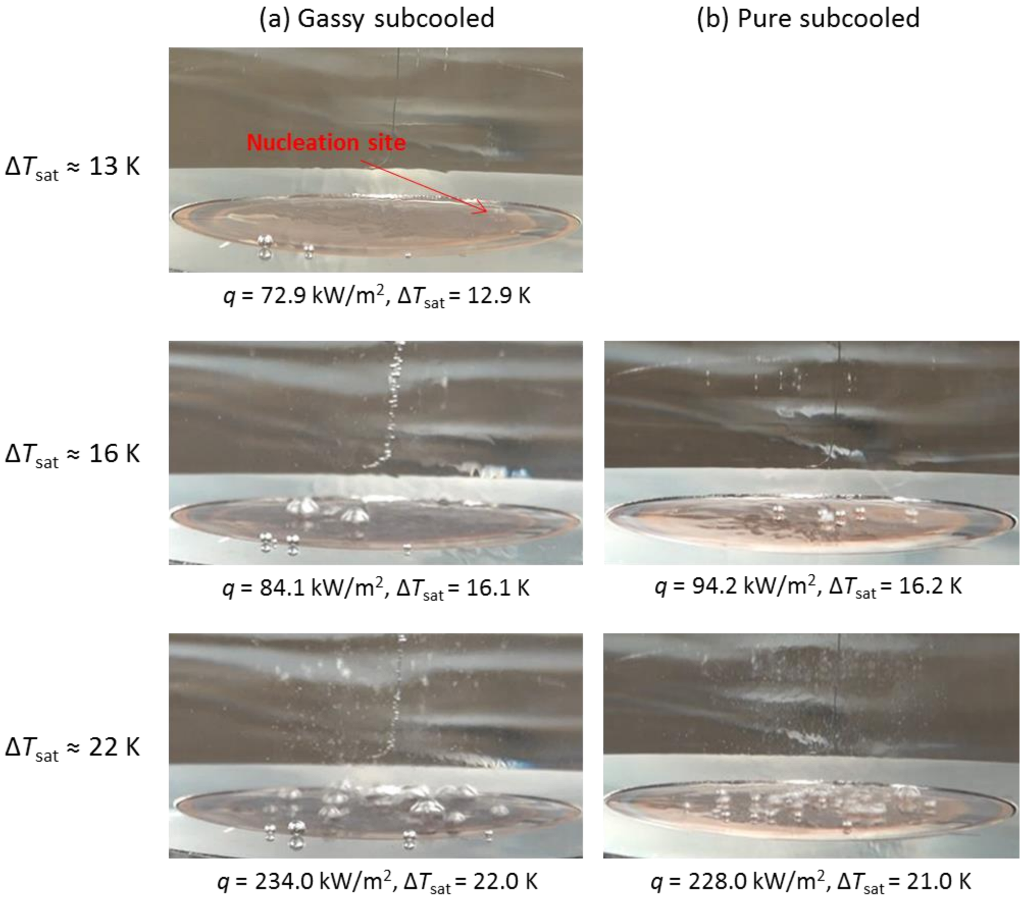

Figure 3.8 Comparison of boiling behavior of the mirror-finished copper surface at $\Delta T_{\mathrm{sub}} = 20$ K and $\Delta T_{\mathrm{sat}} \approx 13$, 16, 22 K under (a) gassy and (b) pure subcooled conditions. For the pure subcooled condition, the boiling behavior at $\Delta T_{\mathrm{sat}} \approx 13$ K is omitted because it is still in the natural convection region.

data within 30%, which supports the above suggestion.

As shown in Fig. 3.8, a large number of bubbles attach on the thermocouples, which is used in the single bubble experiment, in the gassy subcooled condition, whereas they do not appear in the pure subcooled condition. Those bubbles are supposed to mostly consist of air because the thermocouple, placed far from the heating surface, is surrounded with subcooled liquid. This comparison makes it clear that the amount of dissolved air is considerably reduced under the pure subcooled condition. Since remarkable difference is not observed in the boiling curve and behavior between the pure and gassy subcooled conditions, dissolved air does not affect heat transfer performance on the mirror-finished copper surface.

3.3.2 Biphilic surface

Similar experiments were repeated for a biphilic surface. The surface consists of a TiO_2-sputtered surface having hydrophobic spots (6 mm in diameter, φ, and 7 mm in pitch, p) made by the PTFE spray coating, as shown in Fig 3.9a. The resulting boiling curves are indicated in Fig. 3.9b, and ΔT_{ONB} are summarized in Table 3.2.

ΔT_{ONB} shifts from the negatives values in the gassy subcooled condition to the positive values in the pure subcooled condition. The difference of ΔT_{ONB} between the two condition is enough larger than the measurement error (about ±0.3 K). Hence, it is revealed ONB at negative ΔT_{sat} never occurs without sufficient presence of dissolved air even on a hydrophobic surface. The maximal cavity diameter is estimated to be 5.9 μm by using ΔT_{ONB} in the pure subcooled condition (= 2.5 K), in the same way as before. The obtained diameter seems to be reasonable, compared with the surface roughness ($R_a \approx 3$ μm) and SEM image of the PTFE spray coating (see Fig. 2.3). ΔT_{ONB} in the gassy subcooled condition is derived to be −3.7 K,

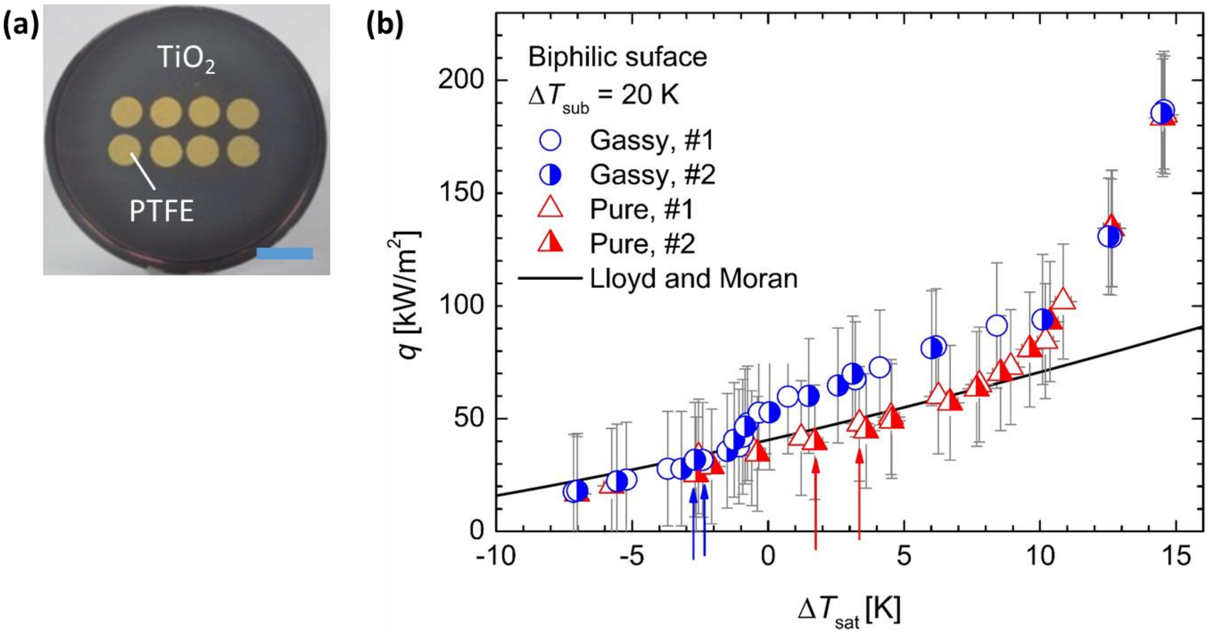

Figure 3.9 (a) A photo of the biphilic surface having hydrophobic spots made of the PTFE spray (6 mm in diameter and 7 mm in pitch) on the TiO_2 surface. Scale bar: 10 mm. (b) Boiling curves of the biphilic surface at $\Delta T_{\mathrm{sub}} = 20$ K under the gassy and pure subcooled conditions.

Table 3.2 ΔT_{ONB} [K] corresponding to Fig. 3.9b.

Condition	#1	#2
Gassy	−2.4	−2.7
Pure	3.3	1.7

which is in good agreement with the experimental results.

The boiling curves are remarkably different between the two conditions, unlike on the mirror-finished copper surface. In the pure subcooled condition, heat transfer is enhanced at $\Delta T_{\mathrm{sat}} \approx 10$ K, but not at ONB. By contrast, boiling curves in the gassy subcooled condition significantly differs from those on normal surfaces. Inclinations of the boiling curves sharply increase in the range from ΔT_{ONB} to $\Delta T_{\mathrm{sat}} \leq 0$ K, and then decreases again. Subsequently, gassy subcooled boiling keeps its heat flux 20-30 kW/m^2 higher than that of natural convection (the solid line in the figure) at $0 < \Delta T_{\mathrm{sat}} < 12$ K. Finally, gradients of the boiling curves start to increase at $\Delta T_{\mathrm{sat}} \approx 12$ K. The boiling curves in the two conditions overlap with each other at $\Delta T_{\mathrm{sat}} \geq 12$ K. Not that, due to the nature of the apparatus, an error of q is relatively large (see error bars in Fig. 3.9b); however, heat transfer in the gassy subcooled condition is no doubt improved at -2 K $< \Delta T_{\mathrm{sat}} < 12$ K, because the all boiling curves are almost perfectly converged in the range of $\Delta T_{\mathrm{sat}} \leq -2$ K and ≥ 12 K.

Figure 3.10 shows an evolution of boiling behavior in the gassy subcooled condition from ONB to $\Delta T_{\mathrm{sat}} = 0.7$ K, where the first heat transfer enhancement occurs. A tiny bubble is firstly generated on the edge of the hydrophobic spot (Fig. 3.10a). Subsequently, the number of bubbles on the periphery increases as q increases (Fig. 3.10b and c). By further increasing q, bubbles with a diameter of 1-2 mm are formed owing to coalescence of neighboring tiny bubbles (Fig. 3.10d and e). Finally, on each hydrophobic domain, the bubbles merges into a vapor dome, which cover the hydrophobic spot (Fig. 3.10f). During this period, generated bubbles stay on the spot for a long time, while coalescing laterally. From the above, the boost

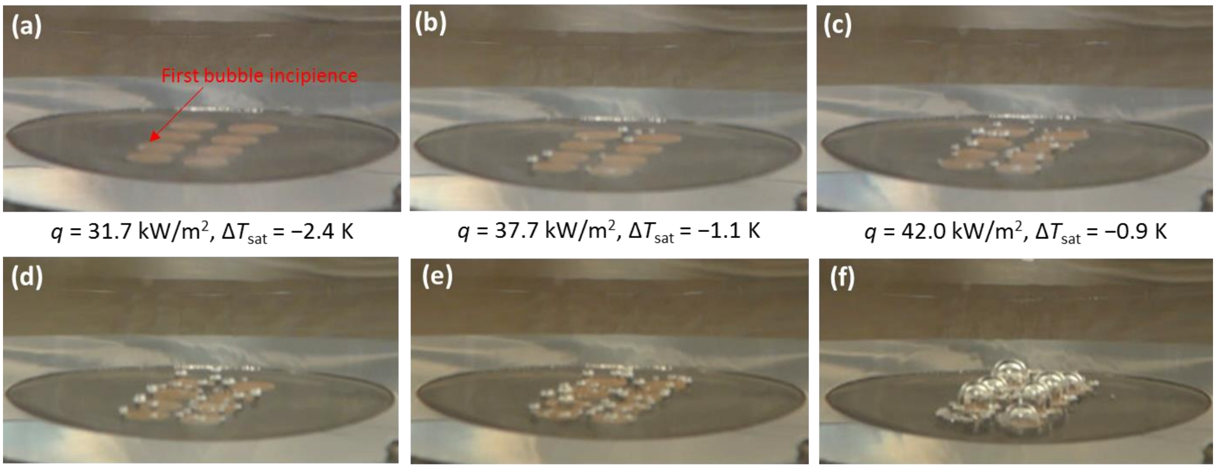

(a) q = 31.7 kW/m^2, ΔT_{sat} = −2.4 K (b) q = 37.7 kW/m^2, ΔT_{sat} = −1.1 K (c) q = 42.0 kW/m^2, ΔT_{sat} = −0.9 K

(d) q = 47.9 kW/m^2, ΔT_{sat} = −0.8 K (e) q = 52.7 kW/m^2, ΔT_{sat} = −0.3 K (f) q = 59.8 kW/m^2, ΔT_{sat} = 0.7 K

Figure 3.10 Evolution of boiling behavior after ONB on the biphilic surface at $\Delta T_{\mathrm{sub}} = 20$ K under the gassy subcooled condition.

of HTC at -2 K< $\Delta T_{\mathrm{sat}} \leq 0$ K is driven by increase in the number of bubbles on the hydrophobic spots. The effect reaches a ceiling when the vapor domes are formed.

Incidentally, the initial bubble nucleation always occurred at the edge of a hydrophobic spot, and bubbles were mainly generated on the hydrophobic domains near the border with the hydrophilic substrate through the present experiments. Nanobubbles are considered as a reason for reduction of ΔT_{ONB} on hydrophobic surfaces [153]. Recently, Nishiyama et al. [154] revealed that, on a hydrophobic surface with hydrophilic domains, a large number of nanobubbles are usually generated in the vicinity of the hydrophilic domains and the bubbles have high stability. Their finding explains the present result well.

Figure 3.11 indicates a comparison of boiling behaviors between the gassy and pure subcooled conditions at $\Delta T_{\mathrm{sat}} \approx 3$, 6, and 13 K. The first two and the last are where a difference in boiling curves is and is not observed, respectively. An evolution of bubble behavior with q in the pure subcooled condition is similar to that in the gassy subcooled condition—large bubbles, covering the entire surface of the hydrophobic spots, are formed as a result of merging of many tiny bubbles. However, the bubbles take a spherical-cap shape with a lower height

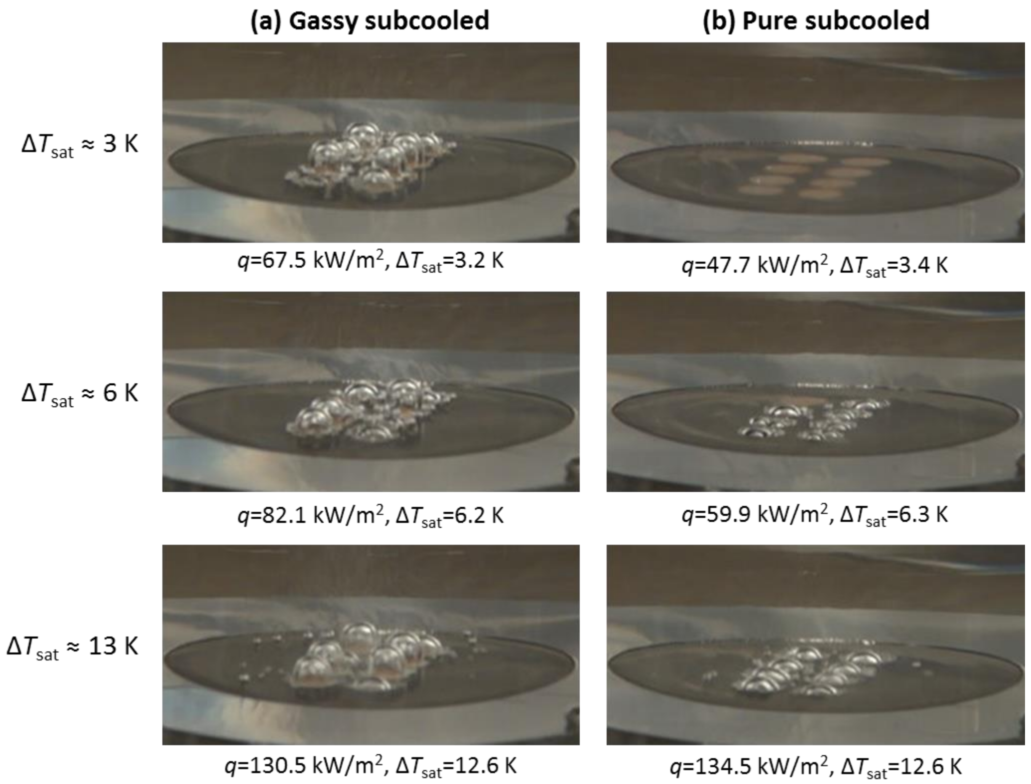

Figure 3.11 Comparison of boiling behavior on the biphilic surface at $\Delta T_{\mathrm{sub}} = 20$ K and $\Delta T_{\mathrm{sat}} \approx 3, 6, 13$ K under (a) gassy and (b) pure subcooled conditions.

($\Delta T_{\mathrm{sat}} = 6.3$ K in Fig. 3.11b), unlike the gassy subcooled condition where tall vapor domes are formed. As ΔT_{sat} increases, many small bubbles depart from the periphery of the hydrophobic spots, meanwhile, the primary bubbles keep their own shape. The microconvection, induced by detachment of the small bubbles, results in the heat transfer enhancement at $\Delta T_{\mathrm{sat}} = 8\text{-}10$ K in the pure subcooled condition (Fig. 3.11b). Bubbles start to depart frequently from nucleation sites on TiO_2 surface at $\Delta T_{\mathrm{sat}} \approx 10$ K ($\Delta T_{\mathrm{sat}} = 13$ K in Fig. 3.11b), leading to the significant increase in HTC.

In the gassy subcooled condition, the vapor domes, which depart with a very low frequency, cover the hydrophobic spots at $\Delta T_{\mathrm{sat}} \geq 0.7$ K. Multiple small bubbles are generated on the periphery of the hydrophobic spot. Part of those bubbles is accumulated by the primary bubble and the others rise into the bulk. The behavior is similar to the previous result reported by Takegawa et al. [84]. ONB on the hydrophilic region also occurs at $\Delta T_{\mathrm{sat}} \approx 10$ K ($\Delta T_{\mathrm{sat}} = 13$

K in Fig. 3.11a).

3.4 Single bubble behavior

Behavior of a single bubble on a hydrophobic spot was observed to investigate the effect of dissolved air on bubble growth and departure in detail. A temperature distribution inside a bubble was also measured by using a thermocouple with a diameter of 150 μm. Results and considerations through the experiments are described in this section.

3.4.1 Bubble behavior and bubble departure diameter and frequency

3.4.1.1 Gassy subcooled condition

Figure 3.12a-c show evolutions of bubble behavior in the gassy subcooled condition at $\Delta T_{\mathrm{sub}} = 20$ K and $\Delta T_{\mathrm{sat}} = -1.2$, 7.1, and 11.5 K, respectively. TiO_2 surfaces with a hydrophobic spot ($\varphi = 6$ mm) made by P-HNT coating were used in the experiment (see Fig. 2.4). A frame rate was set at 1000 fps. As shown in Fig. 3.12a, a single bubble expands over the entire of the spot at a negative ΔT_{sat} ($= -1.2$ K). The bubble gradually grows into an elongated slug shape, although lateral expansion is confined at the edge of the spot. Eventually, concavity is formed on the bubble interface (indicated with the red arrows in the figure). Then, a partial bubble departure of the above-neck portion occurs, while leaving the bubble base on the spot. During the bubble departure process, TPCL is always pinned at the border of hydrophilic and hydrophobic domains. This bubble behavior (so-called "necking") is also reported by Nam et al. [87]. Additionally, the interface of the bubble is very smooth at $\Delta T_{\mathrm{sat}} = -1.2$ K, because vapor is supplied only by evaporation at its TPCL and surrounding superheated liquid layer. As ΔT_{sat} increases, small bubbles, generated at the periphery of the hydrophobic spot, merge into the primary bubble, which was also observed in the heat transfer experiment (Fig. 3.11). As a result, the more disturbed interface is obtained, the higher ΔT_{sat} becomes (Fig. 3.12b and

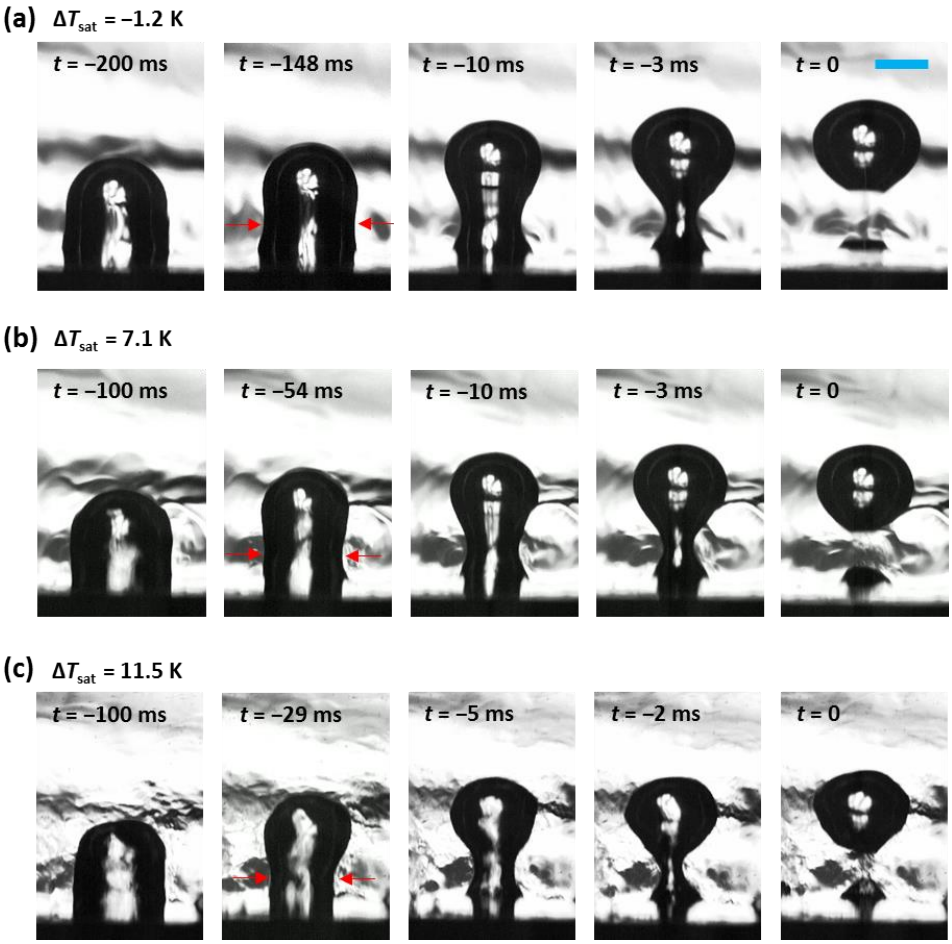

Figure 3.12 Evolutions of bubble behavior in the gassy subcooled condition at $\Delta T_{\mathrm{sub}} = 20$ K and $\Delta T_{\mathrm{sat}} = -1.2$, 7.1, and 11.5 K. Scale bar: 3 mm.

c); however, even in such cases, bubble departure follows the necking, and part of vapor is remained on the spot after the detachment.

Figure 3.13a and b present bubble departure frequencies, f_{d}, and diameters, d_{d}, in the gassy subcooled condition, respectively. The figures include data obtained by Tashiro [155] in the same condition, but a different surface—a single hydrophobic spot ($\varphi = 6$ mm and $\theta = 120$-127°) on a copper surface ($\theta = 70^{\circ}$). The error bars in the vertical direction are the maximal and minimal values over measurement of five bubbles. A periodic bubble departure with a very small frequency (9.0×10^{-4} Hz) is observed at a negative ΔT_{sat} ($= -1.2$ K). As mentioned in the next sub-section, bubble departure cannot take place without sufficient amount of air inside the bubble. Therefore, this result means air is supplied to the bubble by evaporation of

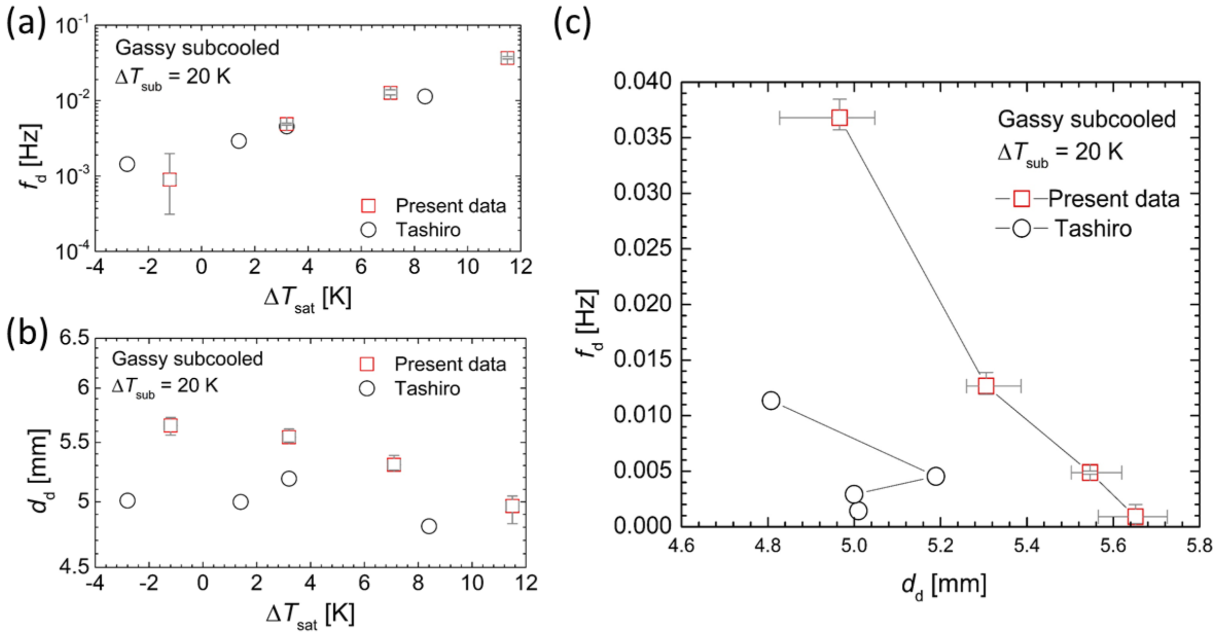

Figure 3.13 (a) The bubble departure frequency, f_d, and (b) diameter, d_d, from a single hydrophobic spot (with φ = 6 mm and $\theta \approx 140^\circ$) coated on superhydrophilic surface ($\theta \approx 0^\circ$). The results of Tashiro's study [155] taken with a copper surface ($\theta = 70^\circ$) having a single hydrophobic spot (θ = 120-127°) are also plotted for comparison. (c) Relationship of f_d vs. d_d.

the surrounding liquid containing dissolved air even at negative ΔT_sat. The bubble keeps accumulating air since only water vapor is condensed at its upper part. Bubble departure occurs when an amount of air inside the bubble becomes high enough. Latent heat transportation due to the evaporation and condensation must contribute to heat transfer in the gassy subcooled condition. f_d highly depends on ΔT_sat, which is increased by more than 40 times from $\Delta T_\mathrm{sat} = -1.2$ K to 12.9 K. On the other hands, d_d decrease by only 13% in the same range. Relationship of f_d vs. d_d is shown in Fig. 3.13c. It has been proposed in previous studies that the product of f_d and d_d takes a constant value. Zuber's correlation [156] is a representative of them,

$$f_\mathrm{d} d_\mathrm{d} = 0.59\left[\frac{\sigma g\left(\rho_\mathrm{l}-\rho_\mathrm{v}\right)}{\rho_\mathrm{l}^2}\right]^{1/4} \tag{3.9}$$

Solved for $\Delta T_\mathrm{sub} = 20$ K, the right side of the equation becomes 0.094, and f_d at $d_\mathrm{d} = 5$ mm is derived to be 18.7 Hz. However, a value of $f_\mathrm{d} d_\mathrm{d}$, obtained from the least squares approximation of the experimental data, is 0.00146, which is almost two orders of magnitude smaller than the correlation. In the present experimental range, bubble departure is supposed to be dominated by the balance of static forces (surface tension and buoyancy) since f_d are extremely small. In addition, as mentioned above, the bubble contact diameter is kept constant due to the pinning of TPCL. Therefore, the adhesion force acting the bubble is slightly decreased as ΔT_sat increase because of a lower surface tension at a higher temperature. As a result, d_d is less dependent on ΔT_sat. Conversely, f_d is significantly increased with increasing ΔT_sat (or q) due to an increased evaporation rate at higher q. This is considered to be the reason for the huge deviation between the experimental result and eq. (3.9).

The present results of f_d and d_d, agree with Tashiro's data [155] within 10%, excluding f_d at the minimum ΔT_sat (where the deviation is about 50%). Thus, bubble departure behavior is independent of a wettability contrast between hydrophilic and hydrophobic domains as far as TPCL is pinned at their border.

3.4.1.2 Pure subcooled

Figure 3.14a shows an evolution of bubble shape with ΔT_sat in the pure subcooled condition, where the red dash lines indicate the heating surface. A vapor cap on the hydrophobic spot is formed at $\Delta T_\mathrm{sat} = 3.6$ K. The bubble fails to detach from the spot while oscillating up and down, though the same condition has been maintained for one hour. Moreover, as ΔT_sat increases, the bubble shrinks and becomes a spherical-cap shape ($\Delta T_\mathrm{sat} = 8.1$ K in Fig. 3.14a), as similar to the heat transfer experiment (Fig. 3.11b). In the present study, bubble departure is not observed at any ΔT_sat.

Time-averaged heights of bubble, H_b, at each ΔT_sat are shown in Fig. 3.14b, where the error bars in the vertical direction indicate maximal and minimal values for five seconds' measurements. The blue dash line is numerically obtained H_b at the departure, which is calculated based on the force balance between surface tension and buoyancy, as below.

$$H_{\mathrm{b}} = \frac{1}{r}\left(\frac{2\sigma}{\rho_{\mathrm{l}} g} - \frac{2}{3} r^2\right) + r \tag{3.10}$$

where the bubble is assumed to consist of a cylinder (H_{c} in height and r in radius) and hemispherical-cap, as shown in Fig. 3.14c. From the above equation, $H_{\mathrm{b}} = 5.4$ mm is necessary to depart from the surface. However, $H_{\mathrm{b}} = 3.7$ mm at $\Delta T_{\mathrm{sat}} = 3.6$ K and are below 1 mm at $\Delta T_{\mathrm{sat}} = 8.1$ and 12.4 K. Thus, departure of the primary bubble does not occur in the pure subcooled condition, because the bubble cannot grow to the necessary height.

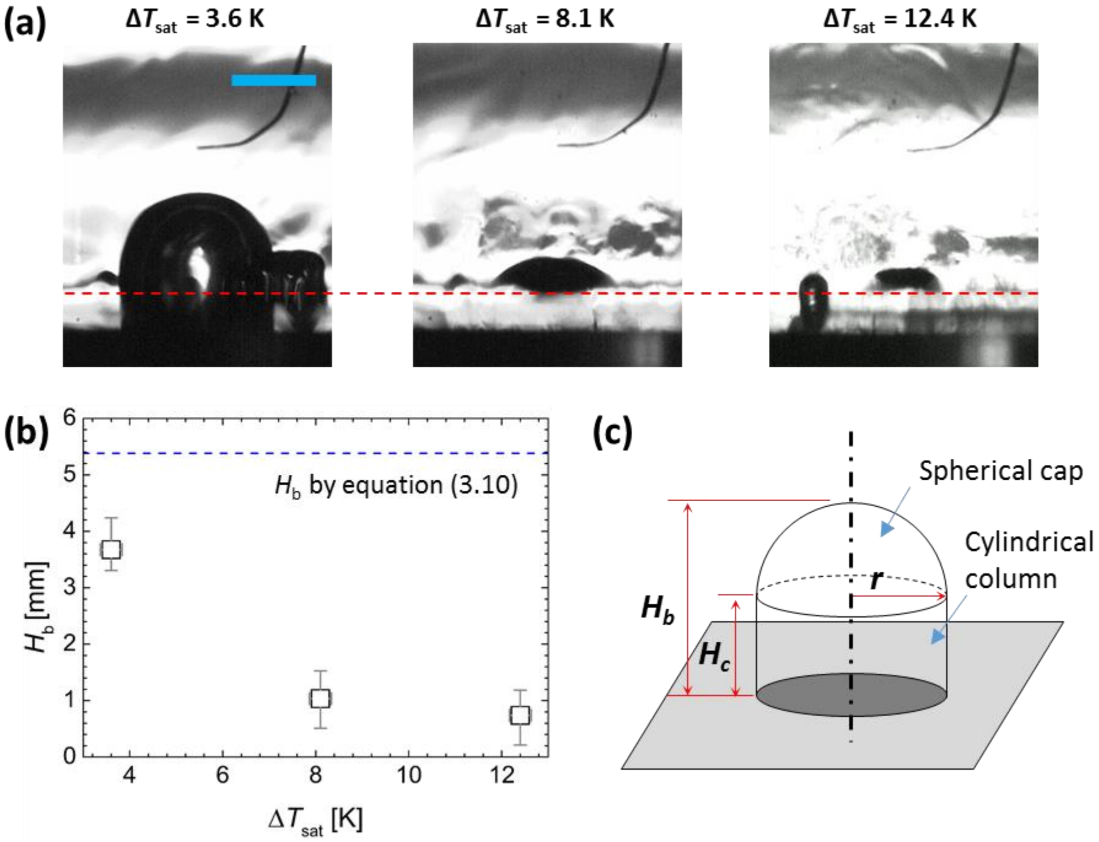

Figure 3.14 (a) Evolution of a bubble shape with increasing ΔT_{sat} at $\Delta T_{\mathrm{sub}} = 20$ K. The red dash line represents the heating surface. Blue scale bar: 3 mm. (b) Plot of the distribution of a time-averaged bubble height, H_{b}, over various ΔT_{sat}. Error bars for the horizontal and vertical axes show the measurement error and the maximal and minimal values for five seconds' measurements, respectively. Blue dash line is calculation of eq. (3.10). (c) The model for eq. (3.10), where a bubble is assumed to be consist of a cylinder with H_{c} in height and r in radius, and a hemispherical cap.

As seen in Fig3.14a, a contact diameter of the bubble shrinks at $\Delta T_{\mathrm{sat}} = 12.4$ K, although they are almost the same between $\Delta T_{\mathrm{sat}} = 3.6$ and 8.1 K. In observation from a higher angle with the normal video camera, it is confirmed that TPCL recedes from the edge toward the center direction of the spot at $\Delta T_{\mathrm{sat}} = 12.4$ K. Nucleate boiling (that is, frequent departure of small bubbles) takes place on the part of the spot exposed to the liquid: namely, a stable large bubble and small bubbles detaching frequently coexist on the hydrophobic spot. Such boiling behavior is similar to the transient-boiling-like nucleate boiling in the saturated condition observed by Torikai and Yamazaki [81], and Hasegawa et al. [82]. The reason for the shrinkage of the bubble is described in the next sub-section.

3.4.2 Temperature inside bubble

Temperature profiles inside bubbles were obtained by directly inserting a thermocouple (150 μm in diameter) into the bubbles. The measurements were performed from the bottom to apex along with the center line of the bubbles as shown in Fig. 3.15a. The horizontal position of the tip of the thermocouple was confirmed from observation with the high-speed camera. The origin in the vertical direction ($H = 0$) was determined by monitoring outputs of the thermocouple.

Figure 3.15b shows an example of a temperature history during the measurement at $\Delta T_{\mathrm{sat}} = 6.1$ K ($T_{\mathrm{w}} = 106.0$ $^{\mathrm{o}}$C) in the gassy subcooled condition. During $t = 0$-170 s, where T largely fluctuates, the tip is in the liquid side while being moved toward the surface. T suddenly starts to increase at $t \approx 170$ s, because the tip penetrates the interface. Then T sharply rises at $t \approx 240$ s, which corresponds the moment that the tip touches the heating surface. The height is set as $H = 0$. Then, the tip is moved upward step-by-step, which appears in the figure as the stepwise decrease in T. At the last measurement point, only a small part of the thermocouple is inserted inside a bubble. As a result, fluctuation of T becomes comparable to that in the

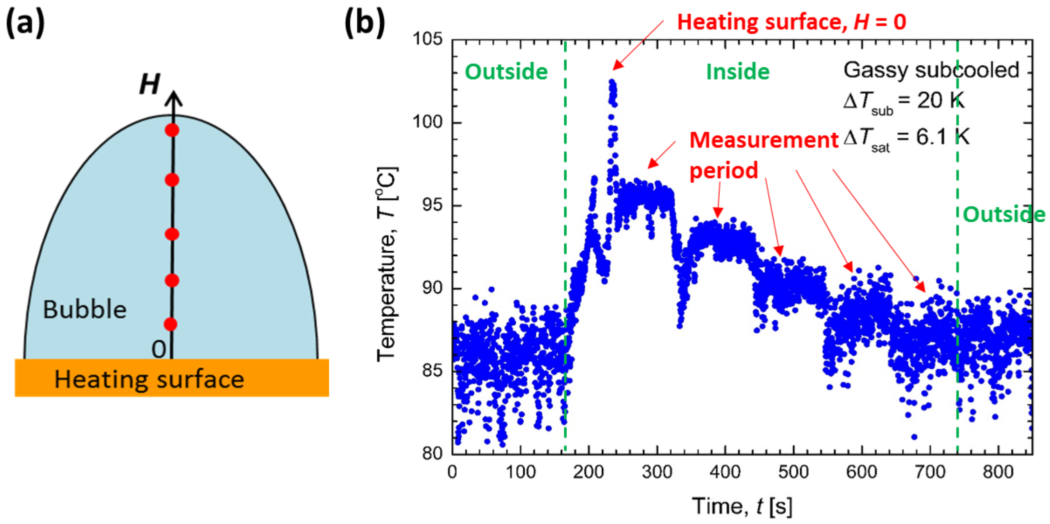

Figure 3.15 (a) A measurement procedure of vapor temperature inside a bubble. (b) Temperature history during the measurement at $\Delta T_{\mathrm{sub}} = 20$ K and $\Delta T_{\mathrm{sat}} = 6.1$ K under the gassy subcooled condition.

liquid phase after $t \approx 650$ s because of heat conduction from the liquid along the thermocouple. By judging from observation with the high-speed camera, the tip goes out from the bubble at $t = 740$ s.

Figure 3.16a indicate temperature profiles inside bubbles, taken by the same way as the above, at various T_{w} under the gassy subcooled condition. Each data is an average of 10 seconds' measurements. Vapor temperatures, T_{v}, are far below the saturation temperature even at just above the heating surface ($H = 0.5$ mm), and decrease with increasing height. Although shapes of temperature profiles are different among T_{w}, T_{v} at the top are almost the same (85.2-85.7 °C). Fig. 3.16b and c show detailed temperature profiles inside bubbles at $T_{\mathrm{w}} = 98.4$ and 109.6 °C, respectively. The figures include T_{w} obtained from the temperature gradient inside the heat transfer block. The error bars in the figures correspond to the maximal and minimal values of 10 seconds' measurements. The blue solid lines are the power-low-approximation of T_{v} (namely, $T_{\mathrm{v}} = \mathrm{a}H^{\mathrm{b}}$), where T_{w} is not used for the fitting. The constant and exponent are $\mathrm{a} = 89.2$ and $\mathrm{b} = -0.0356$ at $T_{\mathrm{w}} = 98.4$ °C, and $\mathrm{a} = 92.9$, $\mathrm{b} = -0.0581$ at $T_{\mathrm{w}} = 109.6$ °C. Taken into account T_{w}, the both temperature profiles are regarded as a curvilinear shape, suggesting convection takes place inside the bubble. However, the Rayleigh number is

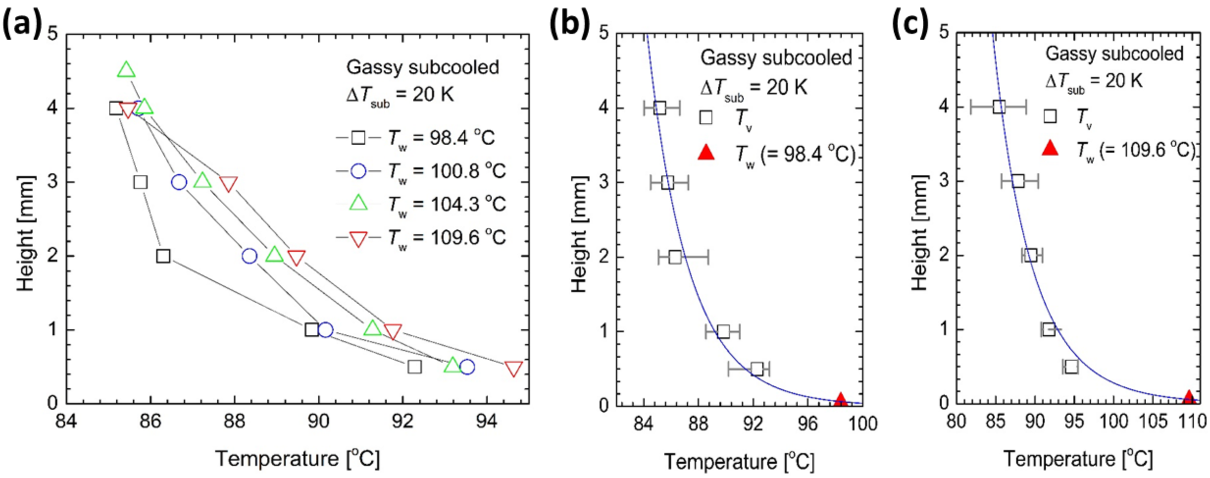

Figure 3.16 (a) Profiles of the vapor temperature, T_{v}, inside a bubble under the gassy subcooled condition at the various T_{w}. The detailed temperature profile at T_{w} = (b) 98.4 °C and (c) 109.6 °C. The red triangles represent T_{w} obtained from the temperature gradient inside the heat transfer block. Blue solid lines are the power approximations of T_{v}. Error bars indicate the maximal and minimal values for 10 seconds' measurements.

derived to be 66.9 by using a temperature at the bottom and apex of the bubble, height of the bubble, and physical properties at the minimum T_{v}. The calculated value is much lower than the critical Rayleigh number of 1708 [44]. Hence, the convection is supposed to be caused by vapor influx at lower part of the bubble, but not natural convection.

Temperature profiles under the pure subcooled condition are shown in Fig. 3.17a. The figure includes data of the gassy subcooled condition at the similar T_{w}, for comparison. Table 3.3 summarizes the minimum vapor temperature, $T_{\mathrm{v,min}}$, in the respective conditions. Note that, in the pure subcooled condition, T_{v} at $T_{\mathrm{w}} > 108.3$ °C could not be measured, because the bubble was too short to insert the thermocouple. As shown in the figure, T_{v} are smaller than the saturation temperature at the all measurement points even under the pure subcooled condition. Fig. 3.17b presents partial pressures of non-condensable gas, P_{g}, inside a bubble calculated from $T_{\mathrm{v,min}}$. P_{g} in the pure subcooled condition still shows large values (≈ 26 kPa), although it is reduced by 40% compared with that of the gassy subcooled condition. As mentioned in Sub-section 3.2.1, an amount of dissolved air in the pure subcooled condition is

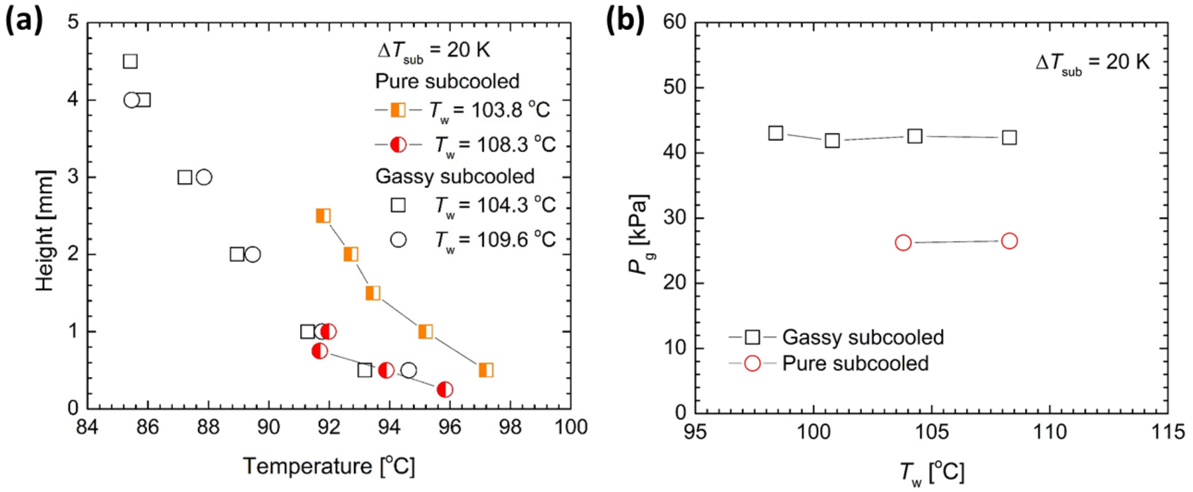

Figure 3.17 (a) Temperature profiles inside a bubble under the pure subcooled condition at T_w = 103.8 and 108.3 °C. For comparison, the results of the gassy subcooled condition at similar T_w are included. (b) The partial pressures of non-condensable gas, P_g, inside a bubble calculated from the minimum values of T_v (summarized in Table 3.3).

Table 3.3 The minimum values of the vapor temperature, $T_{v,min}$, at various T_w.

Gassy subcooled		Pure subcooled	
T_w [°C]	$T_{v,min}$ [°C]	T_w [°C]	$T_{v,min}$ [°C]
98.4	85.2	103.8	91.8
100.8	85.7	108.3	91.7
104.3	85.4		
109.6	85.5		

2.7% of that in the gassy subcooled condition, which is in contradiction with the obtained temperature profile. Recently, molecular dynamics simulation revealed that an amount of gas molecules adjacent to a hydrophobic surface is concentrated by 10-100 times compared with bulk due to suppression of gas diffusion [157, 158]. This gas rich layer might cause the high partial pressure of non-condensable gas in the bubble under the pure subcooled condition.

In the both conditions (Fig. 3.16a and Fig. 3.17a), $T_{v,min}$ are almost independent of T_w, whereas the bubble heights are different (more apparent in the pure subcooled condition). Consequently, it is supposed that bubble growth in the vertical direction is restricted by cooling effect of the surrounding liquid. The bubble can grow up to a certain height where the surrounding liquid temperature is equal to the saturation temperature of the bubble. Therefore, bubbles become tall enough to depart form a surface under the gassy subcooled condition because the saturation temperature of a bubble is reduced significantly due to a large amount of non-condensable gas. Moreover, based on that concept, bubble shrinkage and receding of TPCL with increasing T_w, shown in Fig. 3.14a, are explained as follows. As for convective heat transfer, a thickness of a thermal boundary layer decreases as HTC increases. In the experiment, agitation is facilitated as T_w increases due to promoted natural convection and bubble departure from the edge of the hydrophobic spot. Consequently, HTC is improved with increasing T_w: namely, the thickness of a thermal boundary layer becomes small and the height of the bubble is shortened as T_w increases. When the height is reduced at a certain value and a contact angle of the bubble exceeds an advancing contact angle, TPCL starts to move toward the inside of the hydrophobic spot.

3.5 Numerical simulation of single bubble behavior

Numerical simulation was performed to investigate the effect of dissolved air on subcooled boiling from a biphilic surface. Phase change of a binary system (water and a small amount of nitrogen) was simulated by using the diffuse interface model. From the point of view of computational cost, the physical model was limited to extremely small space (hundreds of nanometers) and time scales (a few nanoseconds). Moreover, a gravitational acceleration was artificially increased in order to have an appreciable impact on bubble dynamics. However, the Bond number was set to be 6.95, which more or less matches that of the experiment (= 5.94).

Figure 3.18 shows obtained bubble behaviors under a single component (only water) and binary (water + nitrogen) systems. In the simulation, an axisymmetric domain is considered. The yellow-collared central portion (30%) of the bottom wall is hydrophobic ($\theta = 120^\circ$), and the green-collared part is hydrophilic ($\theta = 10^\circ$). A temperature of the bottom wall is kept constant at $T = 0.91T^*$, where T^* is the critical temperature of water. In the initial state, a spherical saturated bubble ($T = 0.91T^*$) is put on the center of the hydrophobic domain. A bulk temperature is set to be lower than those of the bubble embryo and heating surface. Nitrogen is chosen as the non-condensable gas, whose initial concentrations in liquid phase are set to be 3500 ppm and 0 for the binary and single component cases, respectively.

In the binary system (Fig. 3.18a), the bubble firstly expands in horizontal direction and

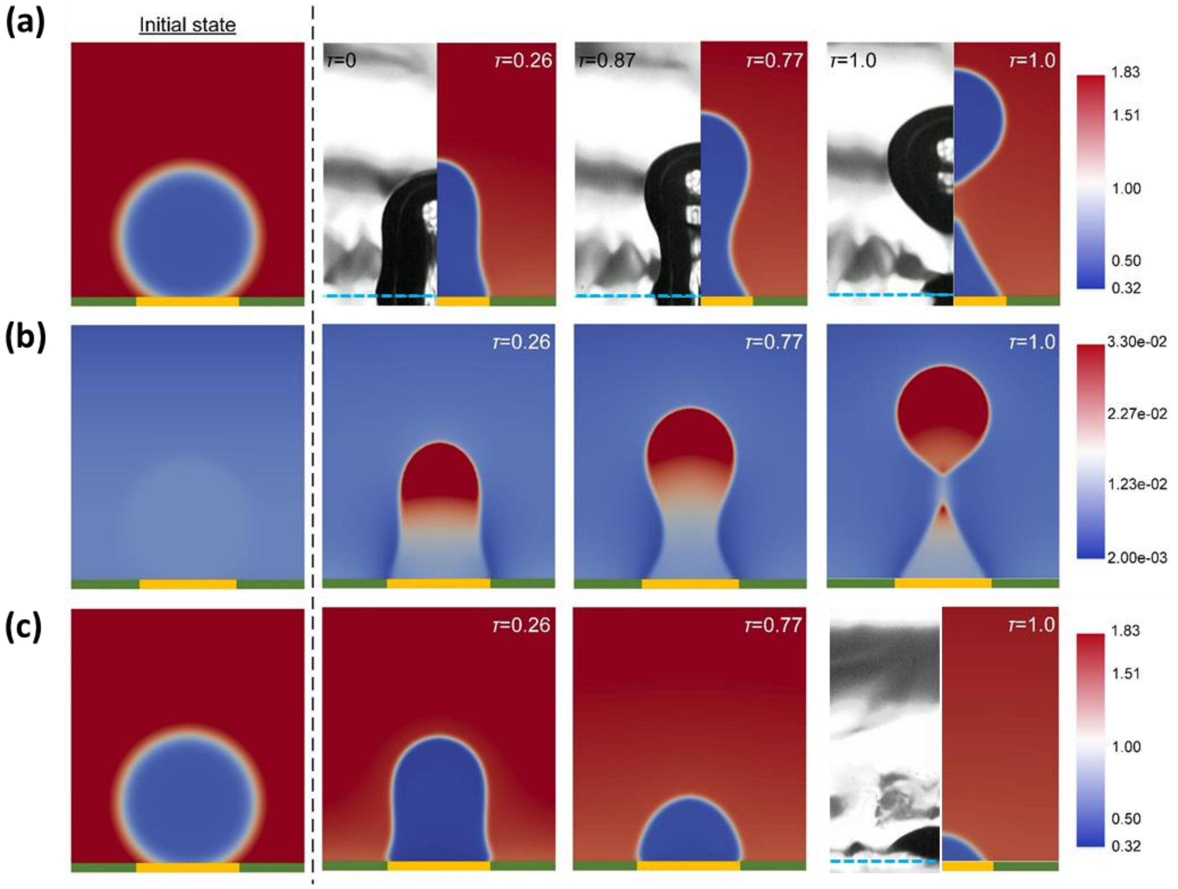

Figure 3.18 (a) Bubble behavior in the binary system (water + nitrogen), which are shown side by side with experimental observations (blue dash lines represent the heating surface). The color scale indicates fluid density normalized by the critical density of water. Nondimensional time, τ, is scaled by the bubble departure period. Contact angles of the yellow- and green-colored portions of the heating surface are set to be 120° and 10°, respectively. (b) A spatial distribution of nitrogen at the same instants as in (a), whose normalized density is represented by the color scale. (c) Bubble behavior in the single component system.

its TPCL is pinned at the border between the hydrophilic and hydrophobic domains. After that, the bubble gradually grows into vertical direction, while accumulating nitrogen (see Fig. 3.18b). Finally, concavity is formed at lower part of the interface, resulting in a partial bubble departure of the above-neck-portion. The obtained bubble behavior shows good qualitative agreement with the experimental result in the gassy subcooled condition. As shown in Fig 3.18b, the accumulated nitrogen is largely concentrated near the apex of the bubble. Therefore, the nitrogen is mostly removed by the partial bubble departure. This finding well explain the experimental results that detached bubbles rise to the surface without condensing completely, and an extremely long departure period is needed for re-accumulation of the non-condensable gas. In the single component system, shown in Fig. 3.18c, the bubble laterally expands until TPCL reaches to the border at first, as with the binary system. Then, however, it keeps shrinking, but not departs from the surface (τ = 0.77 and 1.0 in Fig. 3.18c). This is because condensation of vapor is facilitated owing to an absence of non-condensable gas in the bubble. The result also qualitatively agrees with the experimental observation that bubble does not detach from the surface and takes a flat shape in the pure subcooled condition.

The non-condensable gas affects not only bubble behavior, but also surrounding liquid motion. Fig. 3.19a and b indicate evolutions of a local velocity distribution at the bubble interface under the binary and single component systems, respectively. In the present simulation, the isodensity contour of $\rho = 0.8\rho_l$ is defined as the liquid-vapor interface. The choice seems somewhat arbitrary; however, it is deemed to be justified for the liquid-vapor interface has a finite thickness, which precludes an exact definition. In the binary system, as the bubble grows, the velocity vectors below the neck increasingly align with the bubble surface. This tangential flow is considered to be driven by a difference in surface tension between the low-temperature top and high-temperature bottom of the bubble—Marangoni convection is induced. In the single component system, conversely, the tangential flow appears only in the initial period, then the most of the velocity vectors cut across the interface. The perpendicular flow represents liquid motion due to condensation of vapor.

From the flow distribution in Fig. 3.19a and b, intensities of Marangoni convection is evaluated by integrating a tangential mass flux on the interface over the bubble surface ($M^{\parallel}$

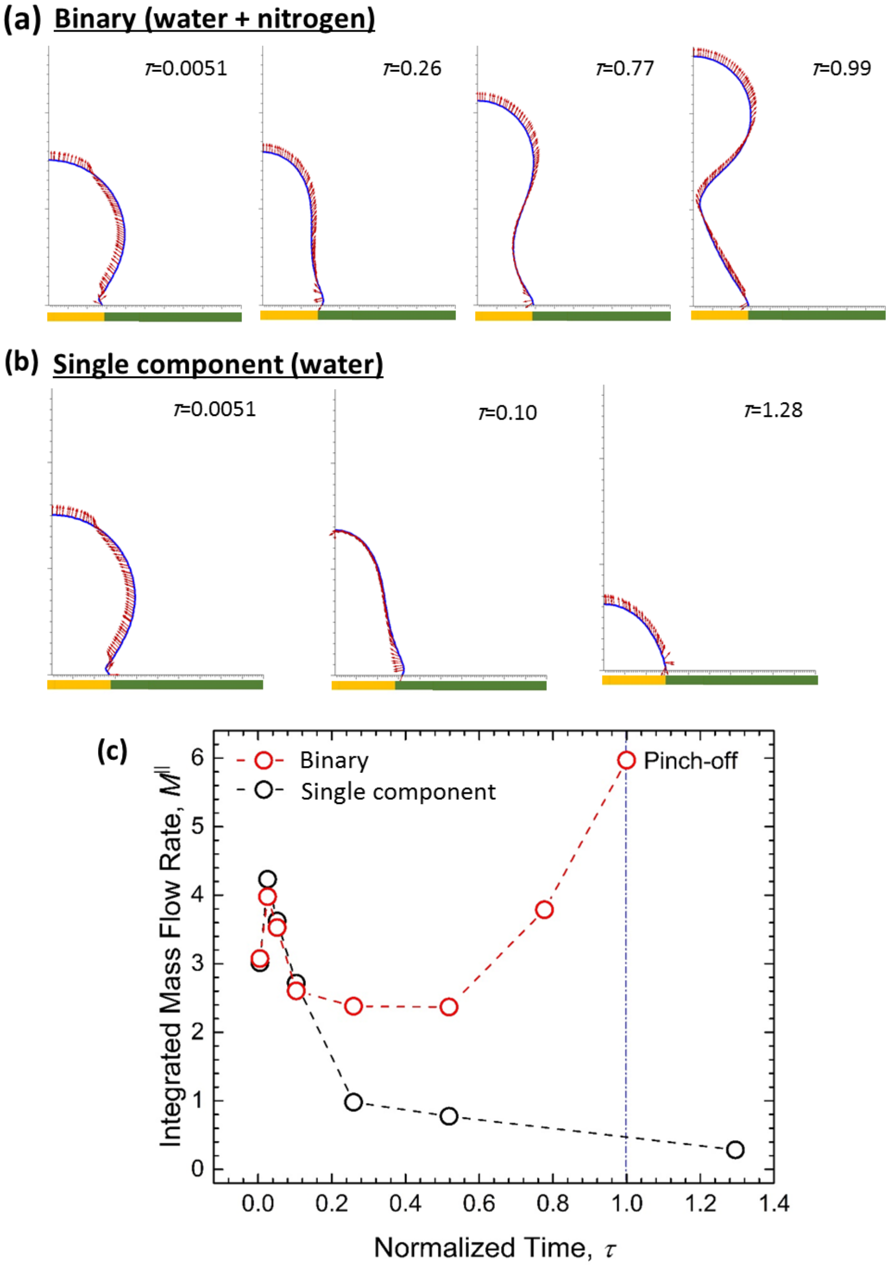

Fig. 3.19 Evolutions of the local velocity distribution of the bubble interface in the (a) binary (water + nitrogen) and (b) single component (water) systems. (c) Total tangential mass fluxes integrated over the liquid-vapor interface, $M^{\parallel}$, versus nondimensional time, τ.

$= \int_L \rho \vec{\mathbf{v}} \cdot \vec{\mathbf{t}}\, \mathrm{d}l$, where $\vec{\mathbf{v}}$ is the velocity vector, $\vec{\mathbf{t}}$ is a unit vector tangential to the surface, and L is the total length of the interface). Figure 3.19c shows $M^{|}$ at various elapsed times in the two systems. In the binary system, the tangential flow takes place over the entire period, which sharply increases after the formation of the necking. $M^{|}$ in the single component system is very similar with that in the binary system at $\tau \leq 0.1$, where the flow is supposed to be dominated by the horizontal expansion of the bubble. Since then, however, it tends to decrease, and becomes less than one tens of the binary system at $\tau = 1$. Through this comparison, it is revealed that non-condensable gas plays significant role in continuation of stable Marangoni convection.

It is generally known that Marangoni convection dominates heat transfer of pool boiling in micro-gravity conditions, but is less apparent under the normal gravity [159, 160]. However, Petrovic et al. [161] found that, in high subcooled conditions, bubbles, formed by dissolved air, induced strong Marangoni convection, improving heat transfer performance remarkably. In their study, subcooled pool boiling on an upward-facing plain copper surface were tested at $\Delta T_{\mathrm{sub}} = 40,\ 50,\ 60,$ and $70\ ^{\circ}\mathrm{C}$. As a result, a Marangoni-convection-dominant regime appeared between the natural convection region and normal nucleate boiling region (triggered by nucleation of pure vapor bubble). Additionally, in such conditions, a gradient of the boiling curve changed twice at the onsets of Marangoni convection and nucleate boiling, which is very similar to the present result (Fig. 3.9b).

3.6 Heat transfer mechanisms

From the above experimental and numerical results, heat transfer mechanisms of the gassy subcooled boiling on the biphilic surface can be explained as follows (classification of heat transfer mechanisms is shown in Fig. 3.20). Heat transfer is dominated by natural convection at $\Delta T_{\mathrm{sat}} < -2$ K, where no or a very few bubbles are generated. Therefore, boiling

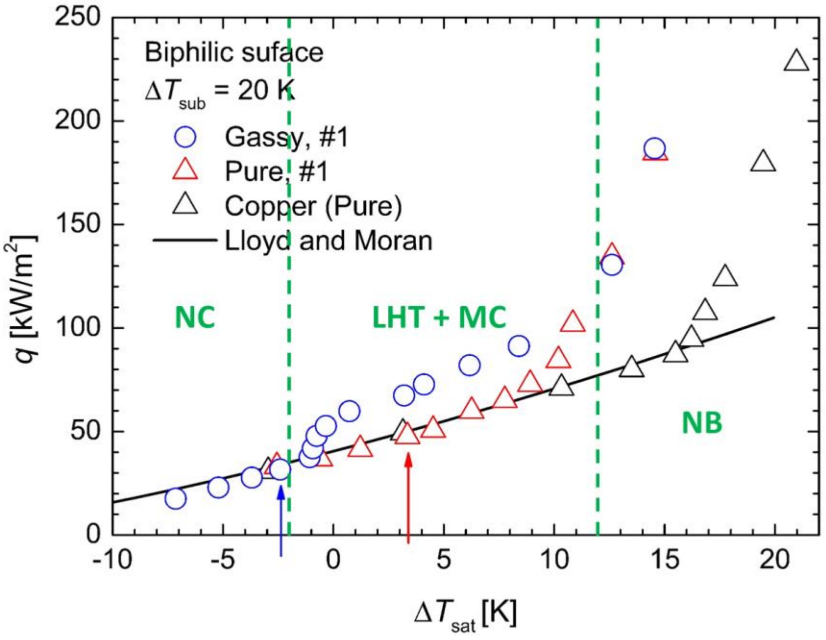

Figure 3.20 Classification of heat transfer mechanisms of the gassy subcooled boiling from the biphilic surface. The data of pure subcooled boiling on biphilic and copper surfaces are plotted for comparison. NC: Natural convection. LHT: Latent heat transport. MC: Marangoni convection. NB: Nucleate boiling.

curves of the two conditions overlap with each other.

At $\Delta T_{\mathrm{sat}} = -2$-12 K, HTC of the gassy subcooled boiling is improved by bubbles on the hydrophobic spots. Heat transfer mode in that region is supposed to differ from that in a normal boiling, since the bubbles hardly detach from the spot. Two mechanisms are considered to be reasons for the heat transfer enhancement. One is latent heat transport due to evaporation at the lower part of the bubbles and condensation at the upper of the bubbles. The other is Marangoni convection, which is driven by a temperature difference between the apex and bottom of the bubbles. Note that a contribution ratio of the respective mechanisms has not been verified in the present study.

Bubble departure from TiO_2 surface and the periphery of the hydrophobic domain plays a significant role in heat transfer at $\Delta T_{\mathrm{sat}} > 12$ K. The heat transfer mechanism is considered to be similar to that in a normal nucleate boiling because an inclination of the boiling curve coincides with that on the mirror-finished copper surface, as shown in Fig. 3.20. Therefore, the difference in HTC between the gassy and pure subcooled conditions is eliminated at $\Delta T_{\mathrm{sat}} >$ 12 K, though the large primary bubbles are still on the hydrophobic spots in the gassy subcooled boiling. Since bubble departure from the spot periphery starts at low ΔT_{sat}, the boiling curves on the biphilic surface are uniformly sifted toward the left side compared with the copper surface.

3.7 Summary

In this chapter, boiling heat transfer experiment and single bubble experiment were conducted to investigate the effect of dissolved air on subcooled boiling from biphilic surfaces. In addition single bubble behavior was simulated by using the diffuse interface model, and consequently, noncondensable gas distribution and surrounding liquid motion were obtained. The main finding through them are summarized as follows.

(1) ΔT_{ONB} shifts from negative values in the gassy subcooled condition to positive values in the pure subcooled condition: namely, ONB at negative ΔT_{sat} does not occur without sufficient presence of dissolved air even on a hydrophobic surface. In addition, the result can be explained well by Torikai's model [121].

(2) Boiling curves of the gassy and pure subcooled conditions almost overlap with each other at $\Delta T_{\mathrm{sat}} \leq -2$ K and ≥ 12 K. HTC is enhanced in the range of -2 K $< \Delta T_{\mathrm{sat}} <$ 12 K under the gassy subcooled condition.

(3) Periodic bubble departure with extremely small frequency (9.0×10^{-4} Hz) is observed at a negative ΔT_{sat} ($= -1.2$ K) in the gassy subcooled condition. The frequency significantly increases as ΔT_{sat} increases, whereas a departure diameter just slightly decreases. By contrast, a primary bubble does not detach from the spot in the pure subcooled condition. Moreover, the bubble shrinks with increasing ΔT_{sat}.

(4) A bubble height is decided by the balance between the saturation temperature of the

bubble (reduced by non-condensable gas) and a temperature of the surrounding liquid. In the pure subcooled boiling, the bubble cannot grow high enough to depart due to lack of dissolved air.

(5) The simulation with the diffuse interface model qualitatively reproduces the bubble behavior obtained in the gassy and pure subcooled conditions. The strong interfacial flow, tangential to the surface (Marangoni convection), is induced only in the two component system (water + nitrogen), because of the enlarged surface tension difference between the apex and bottom of the bubble.

(6) The HTC enhancement due to bubbles stably attaching on hydrophobic spot at -2 K $< \Delta T_{\mathrm{sat}} <$ 12 K in the gassy subcooled condition is considered to be caused by (i) Latent heat transport due to evaporation and condensation and (ii) Marangoni convection.

Chapter 4

Effect of system pressure

4.1 Experimental apparatus and heating surfaces

To control the system pressure, a boiling vessel must be enclosed. Thus, the closed type apparatus (shown in Fig. 3.2) was used in the experiment. Note that the bellows was not used because the target of this study is only the saturated condition. Peripheral equipment was also the same with that in the previous chapter.

Heating surfaces were fabricated by Ni/TFEO electroplating (refer to Sub-section 2.1.5 for details). Three different biphilic surfaces (having different diameters and pitches) and the mirror-finished copper surface were used in the experiments. Pictures and information of the surfaces are shown in Fig. 4.1 and Table 4.1, respectively. The patterns were decided based on the smallest spot diameter which could be made (= 0.5 mm).

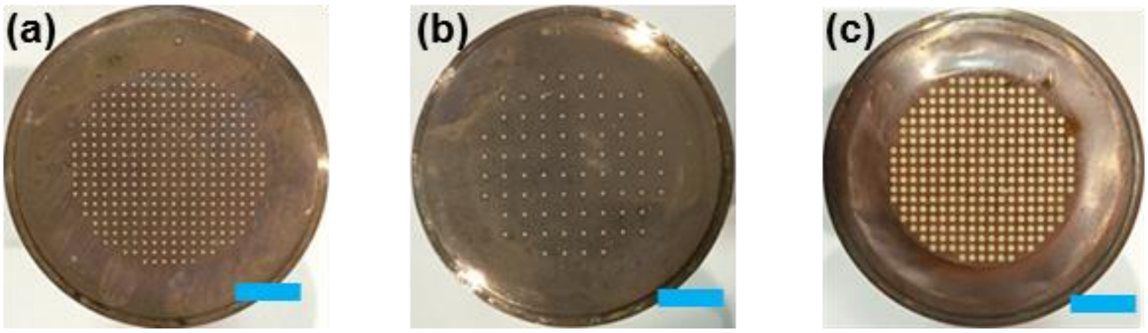

Figure 4.1 Biphilic surfaces with different diameters and pitches of hydrophobic spots, (a) Surface A (φ = 0.5 mm, p = 1.5 mm), (b) Surface B (φ = 0.5 mm, p = 3.0 mm), and (c) Surface C (φ = 1.0 mm, p = 1.5 mm). Blue scale bar: 10 mm.

Table 4.1 Surface information.

Surface	Diameter [mm]	Pitch [mm]	Number of spots	N/A [1/m^2]*	Area ratio**
A	0.5	1.5	316	4.47×10^5	0.088
B	0.5	3.0	80	1.13×10^5	0.022
C	1.0	1.5	316	4.47×10^5	0.351
D	Mirror-finished copper surface				

*The number of the hydrophobic spots per unit area

**Area ratio is calculated by dividing the combined area of the hydrophobic spots by the total heating area.

4.2 Experimental procedures and data reduction

In the present study, to examine superiority of biphilic surfaces, boiling heat transfer experiments were performed with various biphilic surfaces under sub-atmospheric conditions. In addition, single bubble experiments were conducted to investigate the influence of system pressure on bubble behavior. A data reduction method was devised for low pressure conditions. In this section, procedures of the boiling heat transfer experiment and single bubble experiment, and the data reduction method are described.

4.2.1 Boiling heat transfer experiment

The experimental procedure was, by and large, the same with that described in Sub-section 3.2.2, excluding the following processes. The water level was set to be 120 mm from the heating surface, which has significant effect at low pressures, as described later. Then, vacuum degassing was carried out for 2 hours continuously (according to the subcooled boiling experiment in Chapter 3, this degassing procedure is supposed to be enough to eliminate dissolved air). After the degassing, the inside of boiling vessel was filled with a single component (that is, water), naturally reaching the saturated state. System pressure was controlled by adjusting bulk liquid temperature—the bulk temperature was maintained at the saturation temperature corresponding to an intended pressure by using heaters and cooler. After the steady state was reached, boiling curve was taken while increasing heat input to the surface in a stepwise manner.

A data reduction method was also modified for sub-atmospheric conditions. As mentioned later, ΔT_{sat} largely fluctuated with periods from several to tens of seconds due to an occurrence of intermittent boiling at reduced pressures. The sampling time was, therefore, increased to two minutes. In addition, the steady state was judged with two different definitions for continuous and intermittent boiling, respectively. In the case of continuous boiling, when the temperature fluctuation for two minutes became less than $\pm 0.5\ ^{\circ}\mathrm{C}$ without monotonic temperature increase/decrease, the boiling behavior was regarded as the steady state. As for the intermittent boiling, it was difficult to judge the steady state by monitoring the temperature variations owing to the large fluctuation. Thus, it was assumed that the steady state was reached 20 minutes after the heat input was increased, which was the typical waiting time of continuous boiling.

A hydrostatic pressure of a water column with 120 mm in height (about 1.2 kPa) acts on the heating surface during the experiment. Its influence becomes more significant at lower pressures, resulting in a difference of the saturation temperature between the heating surface and liquid surface, as shown in Fig. 4.2. ΔT_{sat} is, hence, calculated with the following equation with the hydrostatic pressure taken into account.

$$\Delta T_{\mathrm{sat}} = T_{\mathrm{w}} - T_{\mathrm{sat}}\left(P_{\mathrm{w}}\right) \tag{4.1}$$

In the above equation, P_{w} is pressure acting on the wall, which is derived from

$$P_{\mathrm{w}} = P_{\mathrm{s}} + \rho_{\mathrm{l}} g H \tag{4.2}$$

where P_{s} is pressure at the liquid surface, calculated based on the bulk liquid temperature, and H is liquid level from the wall. In this chapter, system pressures, P, indicate P_{w} unless otherwise mentioned.

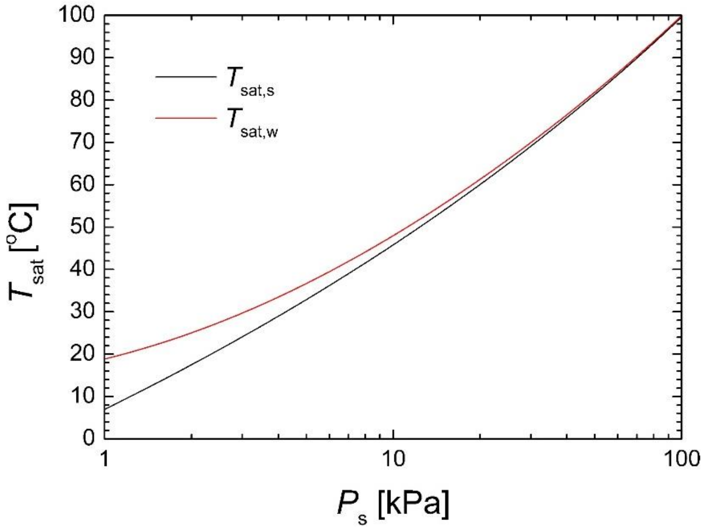

Figure 4.2 Difference between the saturation temperatures at the liquid surface, $T_{\mathrm{sat,s}}$, and heating wall, $T_{\mathrm{sat,w}}$, caused by the hydrostatic pressure of water column with a height of 120 mm, at the various liquid surface pressures, P_{s}.

4.2.2 Single bubble experiment

Experiments were carried out with a copper surface having a single hydrophobic spot made by the PTFE spray coating (see Sub-section 2.1.3). An experimental apparatus was totally the same with that in Sub-section 3.2.3. The following procedure was taken to observe bubble behavior. Firstly, feeding and degassing of water was conducted by the same manner as in the previous sub-section. After a bulk temperature was increased to 100 °C, a bubble was generated on the hydrophobic spot by applying an intended heat input to the surface. Then, the system pressure was reduced stepwisely by decreasing the bulk temperature with heat input to the surface being kept constant. Bubble behavior was captured with a high-speed camera at each pressure. Finally, the experiment was finished at a pressure where the bubble generation was suppressed for more than 20 minutes.

4.3 Boiling heat transfer characteristics

In the present section, the influence of system pressure on heat transfer is described. To make a performance comparison, firstly, experiments were conducted with three different biphilic surfaces and the mirror-finished copper surface under two different pressures: the atmospheric pressure and a reduced pressure (≈ 14.0 kPa). After that, the effect of pressure level was investigated in detail by using a biphilic surface in the pressure range from the atmosphere down to 6.9 kPa. At last, the present result was compared with recent studies for enhancement of sub-atmospheric pool boiling of water and water-based liquid.

4.3.1 Heat transfer enhancement with a biphilic surface

Figure 4.3a shows comparison of boiling curves between Surface D (mirror-finished copper) and Surface B (biphilic with $\varphi = 0.5$ mm and $p = 3.0$ mm) at $P \approx 102.3$ kPa (atmospheric) and 14.0 kPa (corresponding to $T_{\mathrm{bulk}} \approx 50$ °C). The arrows in the figure represent the ONB points, and ΔT_{ONB} are summarized in Table 4.2. The solid lines indicate the calculations based on Kutateladze's correlation [25] at the corresponding pressures,

$$\frac{hl_{\mathrm{a}}}{\lambda_{\mathrm{l}}} = 7.0 \times 10^{-4} Pr_{\mathrm{l}}^{0.35} \left(\frac{ql_{\mathrm{a}}}{\rho_{\mathrm{v}} L_{\mathrm{lv}} \nu_{\mathrm{l}}} \right)^{0.7} \left(\frac{Pl_{\mathrm{a}}}{\sigma} \right)^{0.7} \tag{4.3}$$

$$l_{\mathrm{a}} = \sqrt{\frac{\sigma}{g(\rho_{\mathrm{l}} - \rho_{\mathrm{v}})}} \tag{4.4}$$

where h is HTC, l_{a} is Laplace coefficient, Pr is Prandtl number, and ν is kinetic viscosity. Fig. 4.3b shows relationship between h and ΔT_{sat} in the nucleate boiling regime (namely, after ONB). Error bars in Fig. 4.3a and b correspond to the maximal and minimal values of two minutes' measurements and the measurement uncertainty (see Section A-1), respectively. Note that experiments were conducted at $q < 400$ kW/m^2 and CHF was not taken, in order to avoid damage to the hydrophobic coating (whose allowable temperature is 280 °C).

On Surface D, ΔT_{ONB} is largely increased at the low pressure, leading to the right-side shift of the boiling curve, which agrees with the previous studies [56, 130]. ONB occurs at the

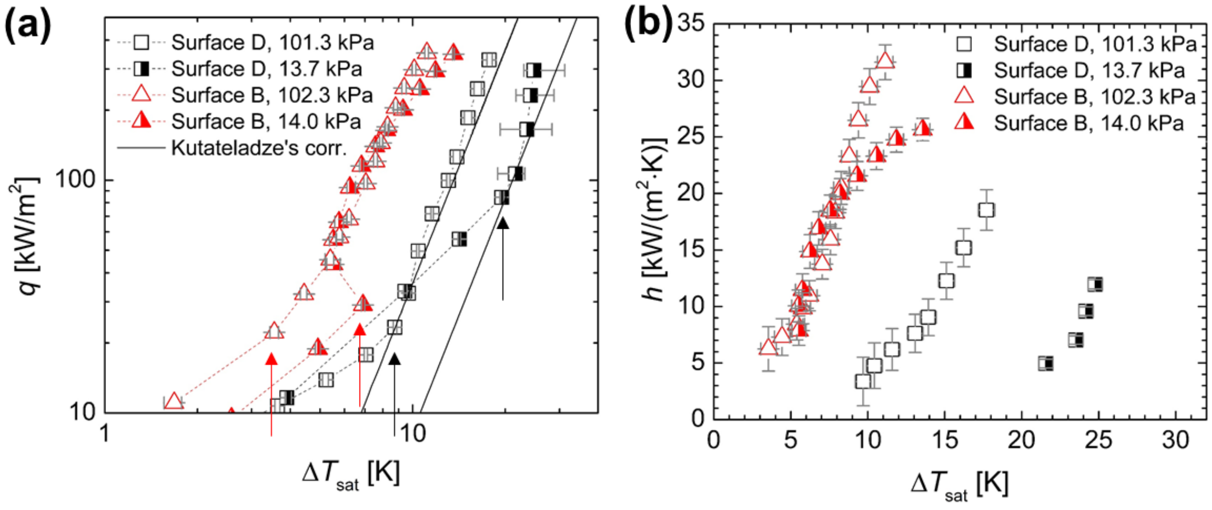

Figure 4.3 (a) Boiling heat transfer comparison between Surface B (φ = 0.5 mm, p = 3.0 mm) and Surface D (mirror-finished copper) at $P \approx 102.3$ kPa and 14.0 kPa ($T_{\mathrm{bulk}} \approx 50$ °C). Error bars show the maximal and minimal values of two minutes' measurements in the steady state. (b) The corresponding h vs ΔT_{sat} in the nucleate boiling region after ONB. Error bars show the measurement uncertainty.

Table 4.2 ΔT_{ONB} [K] corresponding to Fig. 4.3a.

P [kPa]	Surface B	Surface D
102.3	1.6	8.4
14.0	6.9	19.3

extremely low ΔT_{sat} (= 1.6 K) and overshoot was not observed in atmospheric boiling on Surface B. ΔT_{ONB} increases to 6.9 K at P = 14.0 kPa, which is still 12.4 K lower than that on Surface D at the same pressure. HTC on Surface B at P = 14.0 kPa is dramatically enhanced after a temperature excursion at ONB, resulting in the little gap between the two boiling curves at the different pressures. At 6 K ≤ ΔT_{sat} ≤ 8 K, the boiling at the low pressure performs even better than that at the atmospheric pressure. As a result, the boiling performance on Surface B in the sub-atmospheric condition was enhanced by more than six times compared with that on Surface D (comparison at the same ΔT_{sat}). Here, validity of the present apparatus is confirmed since the boiling curves of Surface D at the two pressures show good agreement with eq. (4.3).

One of the signature characteristics of sub-atmospheric boiling is large surface temperature fluctuation, as reported in the previous studies [129, 132]. Fig. 4.4a and b illustrate relationship between the standard deviation, *SD*, of T_1 (measured by the thermocouple inserted at 3 mm below the surface) and q. The data at and above the heat flux of arrowed points are in the nucleate boiling regime. *SD* in natural convection is approximately 0.03 $^{\mathrm{o}}$C, regardless of surfaces. *SD* of atmospheric boiling on Surface D gradually increases at the initial stage after ONB, and then, takes almost constant values (≈ 0.15 $^{\mathrm{o}}$C) at $q \geq 120$ kW/m^2. Under the sub-atmospheric condition, *SD* drastically jumps up due to ONB (notice that the vertical axis of

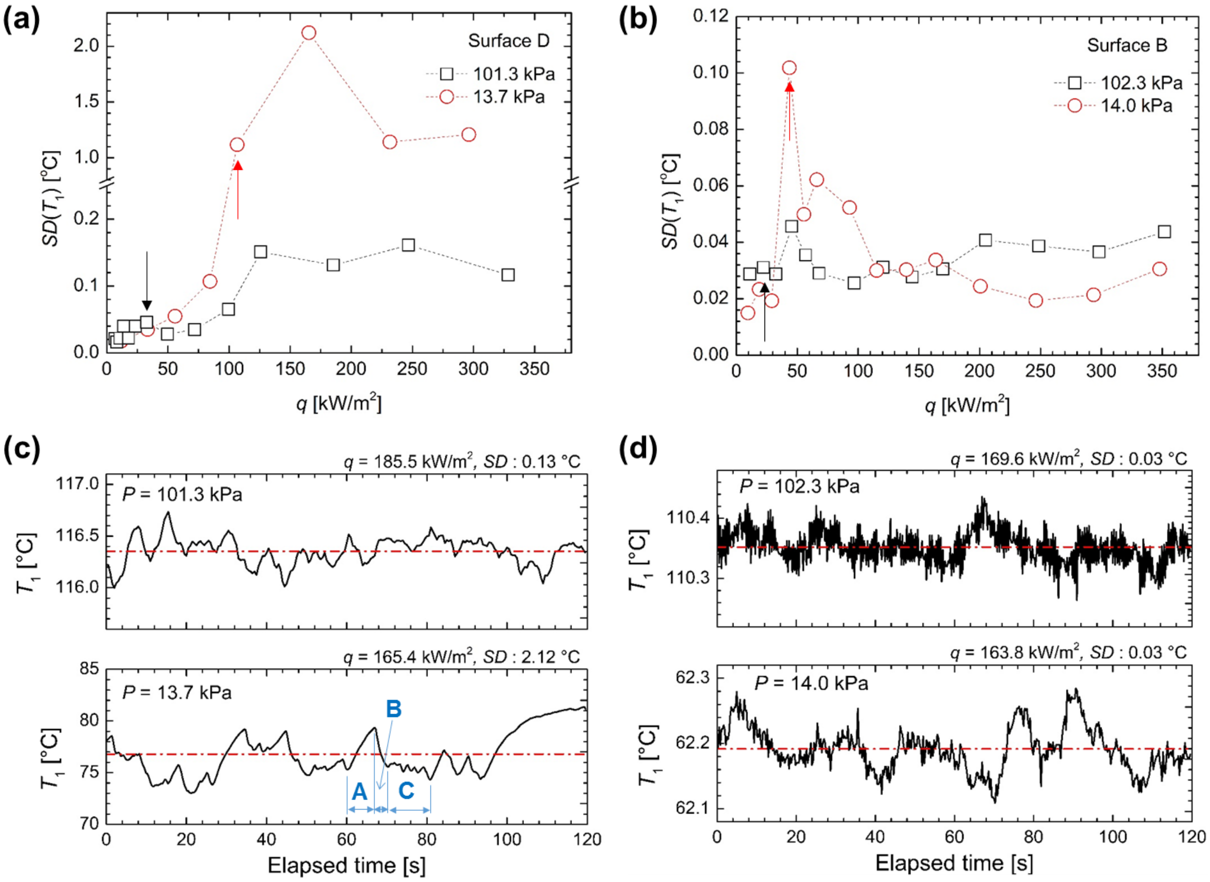

Figure 4.4 Relationships between the standard deviation, *SD*, of T_1 (measured at 3 mm below the top surface) and q on (a) Surface D and (b) B. The data at and above the heat flux of arrowed points are in the nucleate boiling regime. Notice that the vertical axis of (a) is broken for visibility. Transient temperature measurements of T_1 on (c) Surface D and (d) B at $P \approx 102.3$ kPa and 14.0 kPa during two minutes in the steady state at q = 163-186 kW/m^2. The red-dot-dash lines represent the mean values.

the figure is broken), which is one order of magnitude larger than that in the atmospheric condition. Fig. 4.4c illustrates transient measurements of T_1 at $q \approx 170$ kW/m^2 over two minutes in the steady state under the atmospheric and sub-atmospheric conditions. The black solid and red dash-dot lines are measured and averaged values, respectively. At the reduced pressure, large temperature fluctuation occurs with a frequency of 10^{-1} Hz, which is also observed in the previous works using normal metal surfaces [129, 132]. From bubble behavior at the same condition (Fig. 4.5) captured by the video camera, the temperature fluctuation is explained as follows. T_w continuously increases during a waiting period due to low HTC of single-phase natural convection (A in Fig. 4.4c. Note that time scale is not synchronized between the figures). When the surface is heated up enough, nucleation is initiated. The following extensive bubble growth removes a large amount of heat from the surface to the surrounding liquid. Because of the significantly reduced vapor density, the bubble expansion exceeds a size of the outer skirt of the heating surface (see t = 2333 ms in Fig. 4.5). The detachment of this large bubble after the long waiting period induces a sharp drop in T_w. Since cavities on the surface trap part of vapor of the bubble, bubble departures from random nucleation sites follow the first bubble, bringing continuous decrease in T_w (B in Fig. 4.4c). A size of the bubbles gradually decreases with decreasing T_w (t = 2867 ms and 3333 ms in Fig.

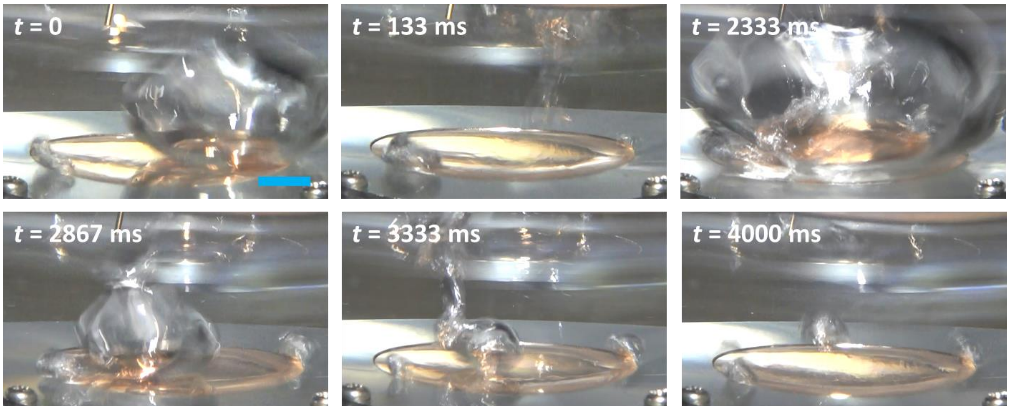

Figure 4.5 Evolution of boiling behavior on Surface D at q = 165.4 kW/m^2 and P = 13.7 kPa, corresponding to the lower panel in Fig. 4.4c. Blue scale bar: 10 mm.

4.5). Finally, boiling is ceased completely after detachment of bubbles with intervals of about one second (C in Fig. 4.4c). A long waiting period is introduced again until a disrupted superheated liquid layer is reconstructed.

On Surface B, as shown in Fig. 4.4b, T_1 at the atmospheric pressure is remarkably stable, whose *SD* is about four times smaller than that of the copper surface at the same pressure. As described in Sub-section 1.4.1, when a bubble departs from the hydrophobic region, part of the bubble is left behind on the surface. The residual vapor works as a nucleus of the next bubble, leading to essentially continuous bubble growth and departure. In addition, bubbles are generated only from hydrophobic spots at up to a medium heat flux, whose departure diameter depends on a size of the spots: namely, bubbles with a uniform diameter detach from uniformly distributed nucleation sites (namely, hydrophobic spots) in boiling on biphilic surfaces. As a result, T_w becomes very stable compared with a normal metal surface. At P = 14.0 kPa, *SD* takes large values at the beginning of boiling; however, there is no remarkable difference between the two pressures at $q > 100$ kW/m^2. Surface B can retain its stabilizing effect on T_w at the reduced pressure. Although a spatial distribution of T_w could not be obtained with the present experimental apparatus, in a series of studies by Zupančič et al. [114, 162], it was revealed that the spatial *SD* of T_w on a biphilic surface is also two times smaller than that on a plain stainless surface. Hence, biphilic surfaces can bring T_w with high temporal and spatial stability.

Figure 4.6a and b show evolutions of boiling behavior on Surface B at P = 102.3 kPa and14.0 kPa, respectively. At the atmospheric pressure, bubbles depart from the all hydrophobic spots with a uniform diameter at q = 45.5 kW/m^2. As q increases, neighboring bubbles start to merge, and eventually large coalesced bubbles detach from the surface at q = 298.1 kW/m^2. By contrast, at P = 14.0 kPa, large bubbles with different sizes are generated from part of the hydrophobic spots at the initial stage of boiling (q = 43.5 kW/m^2 in Fig. 4.6b).

Figure 4.6 Evolutions of boiling behavior on Surface B at P = (a) 102.3 kPa and (b) 14.0 kPa, and various heat fluxes. Blue scale bar: 10 mm.

In this condition, partial deactivation of the spots, which have been activated once, is observed from time to time. This unstable behavior is supposed to be the reason for the slightly enlarged SD in Fig 4.4b. As q increases, the all hydrophobic spots are stably activated ($q = 93.0$ kW/m^2 in Fig4.6b), resulting in SD comparable to that at the atmospheric pressure. At the reduced pressure, since a bubble size becomes large due to a low vapor density, a single large coalesced bubble is released from the surface at high heat fluxes.

Here, based on the observation, behavior of the boiling curve (Fig. 4.3a) is considered. Firstly, a difference between the overshoot at ONB is explained as follows. ONB occurs on a hydrophobic spot having a cavity with an optimum shape for bubble nucleation, regardless of system pressure. A bubble, whose TPCL is pinned at the edge of the spot, is formed at the atmospheric pressure because of low ΔT_{ONB} (= 1.6 K) and high ρ_{v} (= 0.597 kg/m^3). Such small bubble does not interfere the surrounding spots (this is clearly shown in q = 45.5 kW/m^2 in Fig. 4.6a, where isolated bubbles depart from the spots without merging). Therefore, the number of nucleation sites gradually increases as q rises, leading to a smooth incline of boiling curve. Conversely, at P = 14.0 kPa, the initial bubble grows to a large size while engulfing the surrounding spots due to high ΔT_{ONB} (= 6.9 K) and low ρ_{v} (= 0.094 kg/m^3). Then, the bubble leaves residual vapor on the spots during the departure process, resulting in a simultaneous activation of many nucleation sites. Consequently, HTC is sharply improved, which appears on boiling curve as the overshoot. Secondly, behavior of HTC is considered as follows. In general, boiling curve in the nucleate boiling regime has a constant gradient from the isolated bubble region to the interference region (where mushroom-shaped bubbles start to be formed). Then, the gradient decreases in the second transition region (where a formation of dry patches occurs) [22]. At lower pressure, q where the second transition region initiates must become smaller due to lower CHF. Therefore, HTC of P = 14.0 kPa is inferior to that of P = 102.3 kPa at $q > 200$ kW/m^2. On the other hand, when the all hydrophobic spots are activated (namely, constant nucleation site density), HTC depends on a bubble departure diameter and frequency. At low heat flux regime ($q \approx 95$ kW/m^2), bubbles mostly departed without merging at P = 102.3 kPa, whereas lateral coalescence of bubbles is facilitated at P = 14.0 kPa. This promoted departure of large bubbles under the low pressure is considered to trigger the reverse pressure effect (high HTC at low pressure) in the range of 50 kW/m^2 $< q <$ 200 kW/m^2.

4.3.2 Effects of spot diameter and pitch

Similar experiments were repeated for Surface A and C to study the effect of a diameter and pitch of the hydrophobic spots. Fig. 4.7a shows boiling curves on the three biphilic surfaces at the atmospheric and reduced pressure ($P \approx 14.0$ kPa), and the corresponding h vs ΔT_{sat} is illustrated in Fig. 4.7b. The solid lines in Fig. 4.7a are the calculations of eq. (4.3) at the respective pressures. The error-bars in the two figures indicate the measurement uncertainty. In the atmospheric condition, HTCs are higher in the order of Surface C, A, and B over the entire heat flux range. This result is in agreement with the earlier work by Jo et al. [110] that biphilic surface with smaller pitch and larger diameter shows the best HTC at low heat fluxes (smaller diameter was advantageous at $q > 400$ kW/m^2). At $P \approx 14.0$ kPa, conversely, Surface A has the best performance, excluding the initial stage of boiling ($q < 80$ kW/m^2 and $\Delta T_{\text{sat}} < 5$ K), because of significant deterioration of HTC on Surface C. On surface A and B, HTC became worse than that in the atmospheric condition at higher heat fluxes, which is more significant on Surface A.

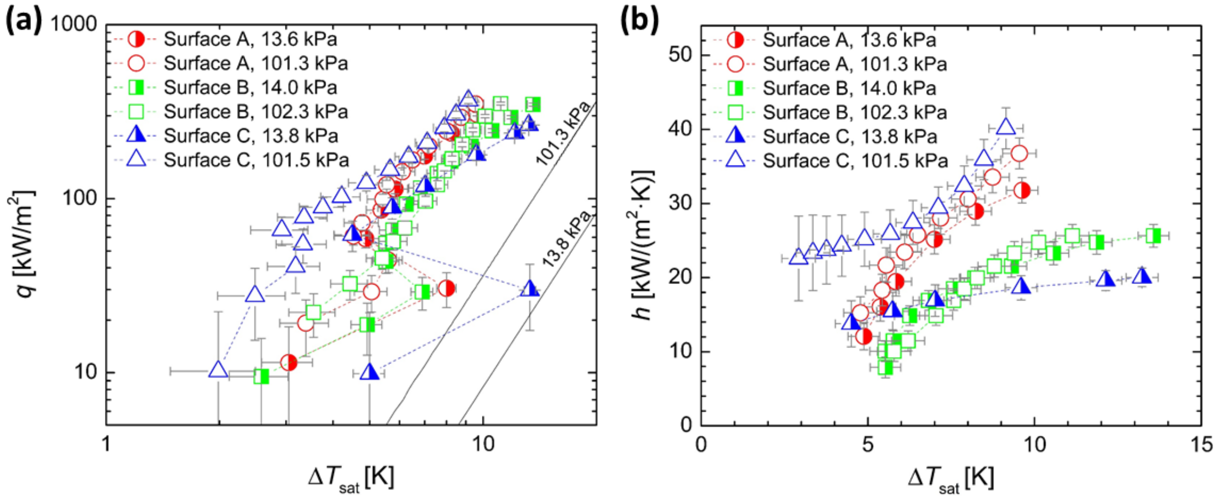

Figure 4.7 (a) Comparison of boiling curves between the three biphilic surfaces (Surface A, B, and C) at $P \approx 101.3$ kPa and 14.0 kPa. The solid lines indicate the calculations of eq. (4.3) at the respective pressures. (b) The corresponding h vs ΔT_{sat} in the nucleate boiling region. Error bars in (a) and (b) show the measurement uncertainty.

Figure 4.8a and b show the influences of a pitch and diameter of the hydrophobic spots, respectively, at the atmospheric pressure and about 14.0 kPa. The vertical axes, $h_{\mathrm{meas}}/h_{\mathrm{corr}}$, correspond to an enhancement ratio of HTC normalized by the calculations of Eq. (4.3) at the respective pressures. As for Fig. 4.8a, HTC is enhanced for smaller pitch over the entire heat flux, regardless of the pressure. The enhancement ratio becomes greater at the low pressure on the both surfaces. This is due to that Surface A and B are less influenced by the system pressure (see Fig. 4.6), meanwhile HTC derived from eq. (4.3) is in proportional to $P^{0.7}$. Moreover, trends of $h_{\mathrm{meas}}/h_{\mathrm{corr}}$ vs. q on the surfaces are similar to each other. On the other hand, heat transfer characteristics much differ between surfaces with the different spot diameters. $h_{\mathrm{meas}}/h_{\mathrm{corr}}$ on Surface C takes very high values at low heat fluxes; however, it sharply decreases as q increases. Furthermore, $h_{\mathrm{meas}}/h_{\mathrm{corr}}$ at the two pressures almost overlap with each other on Surface C, unlike Surface A and B.

As mentioned above, Surface A shows the highest $h_{\mathrm{meas}}/h_{\mathrm{corr}}$ at $P \approx 14.0$ kPa, which exceeds three-fold over the entire heat flux range and reaches the peak (= 3.8) at q = 86.1 kW/m^2 (comparison at the same q).

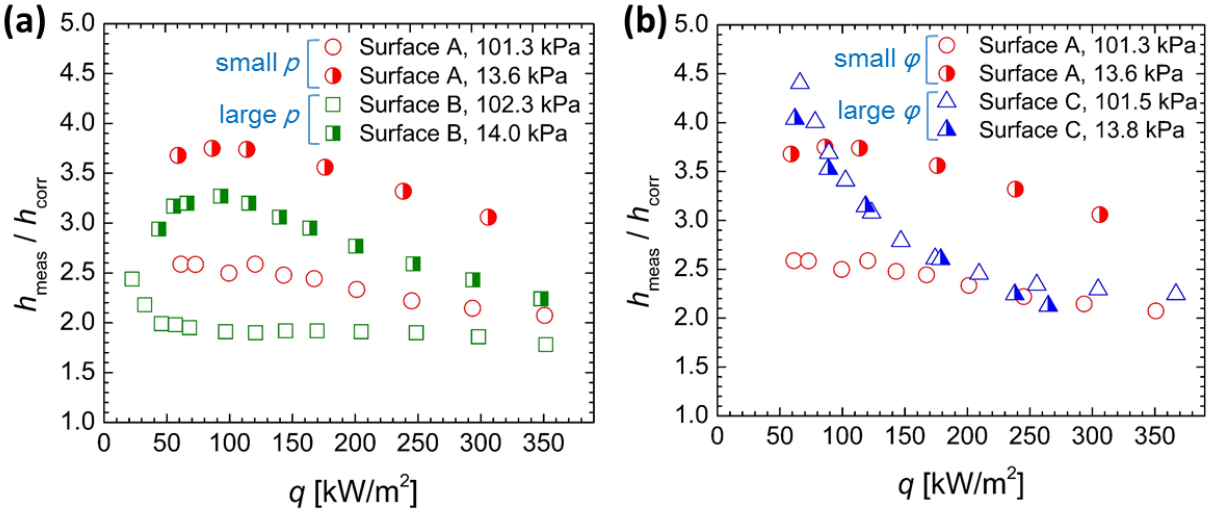

Figure 4.8 Effect of (a) a pitch and (b) diameter of the hydrophobic spots. The vertical axis, $h_{\mathrm{meas}}/h_{\mathrm{corr}}$, is HTC normalized by the calculations based on eq. (4.3) for the respective pressures.

Figure 4.9 and 4.10 show evolutions of boiling behavior at the atmospheric and sub-atmospheric pressures on Surface A and C, respectively. On Surface A, bubbles, generated at the initial stage, do not interfere the surrounding spots at the atmospheric pressure, as with Surface B. However, when neighboring spots are activated, the bubbles inevitably coalesce with each other before the departure (see the red allow in Fig. 4.9a), because a departure

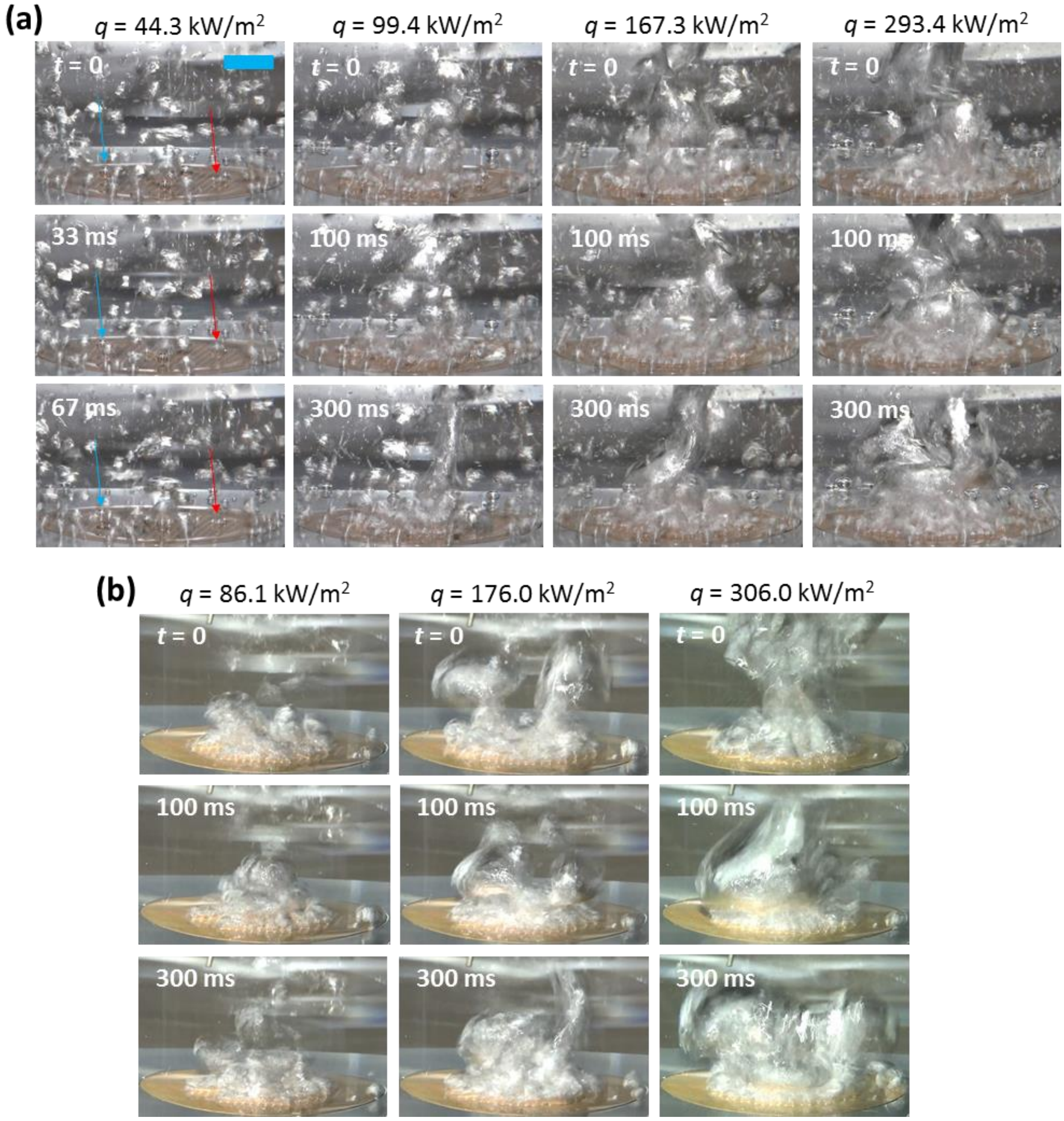

Figure 4.9 Evolutions of boiling behavior on Surface A at P = (a) 101.3 kPa and (b) 13.6 kPa, and various heat fluxes. Blue scale bar: 10 mm. The red and blue arrows indicate bubble merging between neighboring spots and an isolated bubble, respectively.

diameter of a single bubble from a spot with a diameter of 0.5 mm is approximately 3 mm (below the spacing between the spots), as described later in Sub-section 4.4.2. A departure frequency of this merged bubble is approximately 10 times higher than that of isolated bubble (the blue allow in Fig. 4.9a), leading to the substantial increase in HTC. When the all spots are activated, several coalesced bubbles are formed on the surface ($q = 99.4$ kW/m^2 in Fig. 4.6). As q further increases, single large bubble is emitted from the surface, and consequently a gradient of boiling curve decreases (namely, HTC deteriorates). At $P = 13.6$ kPa, formation of coalesced bubble is facilitated and its size is increased owing to a low vapor density. On surface A, boiling curve of $P = 13.6$ kPa gets close but not exceeds that of $P = 101.3$ kPa. This is likely because the heat transfer acceleration effect due to bubble coalescence takes place in the both pressures.

By contrast, on Surface C, it is occasionally observed that nucleation sites spread to the adjacent hydrophobic spots even at the atmospheric pressure. Bubbles coalesce among them in the beginning of their growth period since a departure diameter of a single bubble (≈ 4 mm, see Sub-section 4.4.2 for details) is much larger than a spacing of the hydrophobic spots (0.5 mm at the most narrow part). As a result, violent bubble departure occurs at low ΔT_{sat} ($q =$ 89.1 kW/m^2 in Fig. 4.10), and HTC is significantly improved. However, increase in HTC with increasing q is gradual because liquid supply to the surface is suppressed by frequent departure of mushroom-shaped bubbles. Consequently, $h_{\mathrm{meas}}/h_{\mathrm{corr}}$ is reduced sharply. On Surface C, there is no remarkable difference in boiling behavior between $P = 101.5$ and 13.8 kPa. This coincidence of boiling behavior likely brings the overlapped $h_{\mathrm{meas}}/h_{\mathrm{corr}}$. Incidentally, it is widely known that relationship between q vs. ΔT_{sat} can be characterized as $q \sim \Delta T_{\mathrm{sat}}{}^n$ on a boiling curve. A closer examination of the boiling curve in Fig. 4.7a reveals that there are two characteristic regions which are represented by $n \approx 3$ and 1.3. The former appears at almost entire q in the atmospheric condition and at low q under the reduced pressure on Surface B,

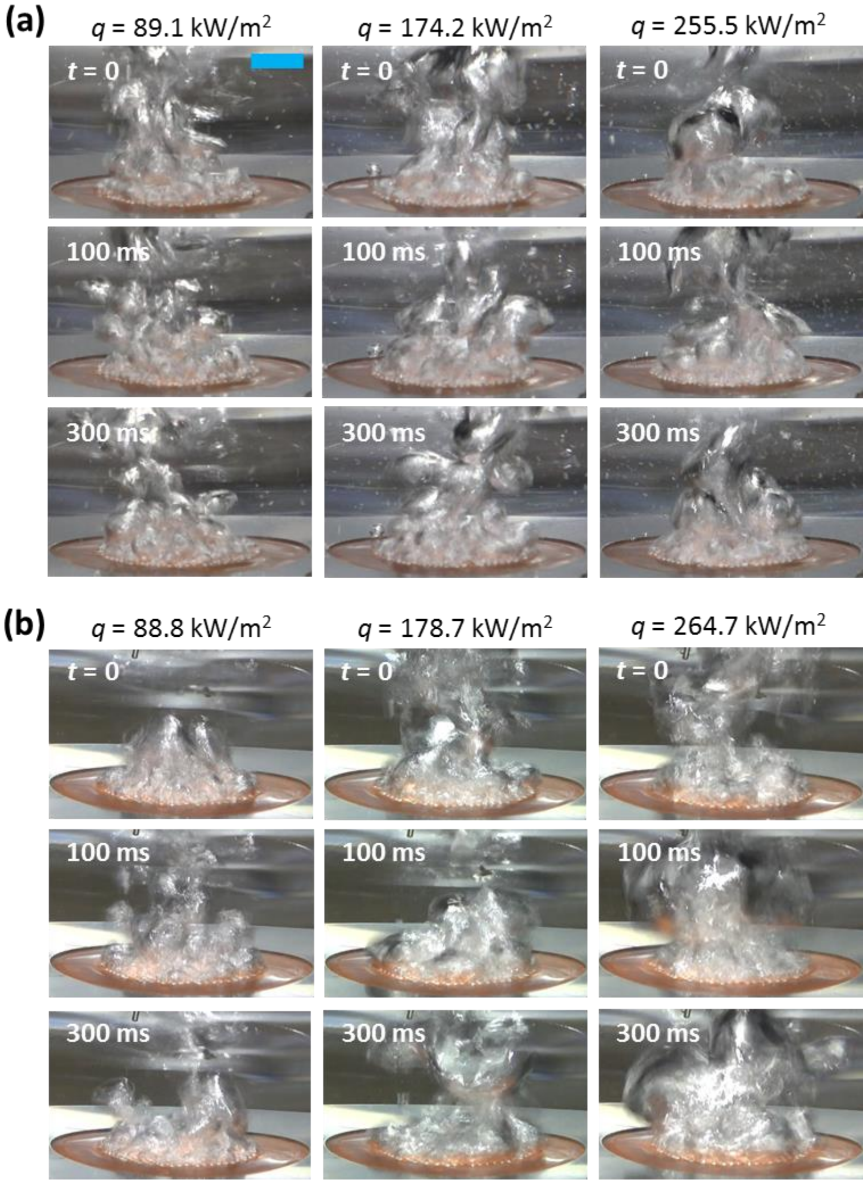

Figure 4.10 Evolutions of boiling behavior on Surface C at P = (a) 101.5 kPa and (b) 13.8 kPa, and various heat fluxes. Blue scale bar: 10 mm.

and at low q under the both pressures on Surface A (see Table 4.3), that is where bubble merging is relatively moderate. The value of $n \approx 3$ is similar to that of eq. (4.3) ($n = 3.3$). Thus, the boiling behavior in the region is estimated to be similar to a normal nucleate boiling. On the other hand, the regime with $n \approx 1.3$ is seen at almost all q under the both pressures on Surface C, and at high q under the reduced pressure on Surface B and A. In a pool boiling experiment on a uniform hydrophobic surface performed by Takata et al. [108], a gradient of

Table 4.3 Two characteristic regions in the boiling curves, shown in Fig 4.7(a), represented by $n \approx 3$ and 1.3 for the equation of $q \sim \Delta T_{\mathrm{sat}}{}^{n}$.

Surface	P [kPa]	Range of q [kW/m^2]	n
B	102.3	45.5-298.1	3.0
	14.0	66.0-115.3	3.2
A	101.3	61.1-120.3	3.1
	13.6	58.0-113.7	3.6
C	101.5	66.0-209.3	1.3
	13.8	62.0-264.7	1.3
A	13.6	176.0-306.0	1.7
B	14.0	200.5-347.9	1.4

boiling curve was $n = 1.3$ in the range from ONB to CHF. Therefore, it is suggested that $n = 1.3$ represents boiling behavior where liquid supply to the surface is extremely difficult. In addition, Gaertner [22] reported that n became 5.5 from the isolated bubble region to the interference region, and decreased to 0.6 in the second transition region. Although the values of n differ from that of Gaertner, the similar transition appears to take place in the present study due to suppressed liquid circulation to the surface at higher q and lower P.

4.3.3 Transition to intermittent boiling on a biphilic surface

The effect of the pressure level was investigated over the range from the atmospheric pressure down to 6.9 kPa by using Surface B. Fig. 4.11a and b show the obtained boiling curves and HTC, respectively, and ΔT_{ONB} are summarized in Table 4.4. The solid lines are the calculations of eq. (4.3) for P = 101.3 kPa and 6.9 kPa. Error bars in Fig. 4.11a and b correspond to the maximal and minimal values of two minutes' measurements and the measurement uncertainty, respectively.

The result shows generally increasing ΔT_{ONB} with decreasing pressure, as with the case of a copper surface (which is inversed between P = 8.6 and 6.9 kPa, because experiments were

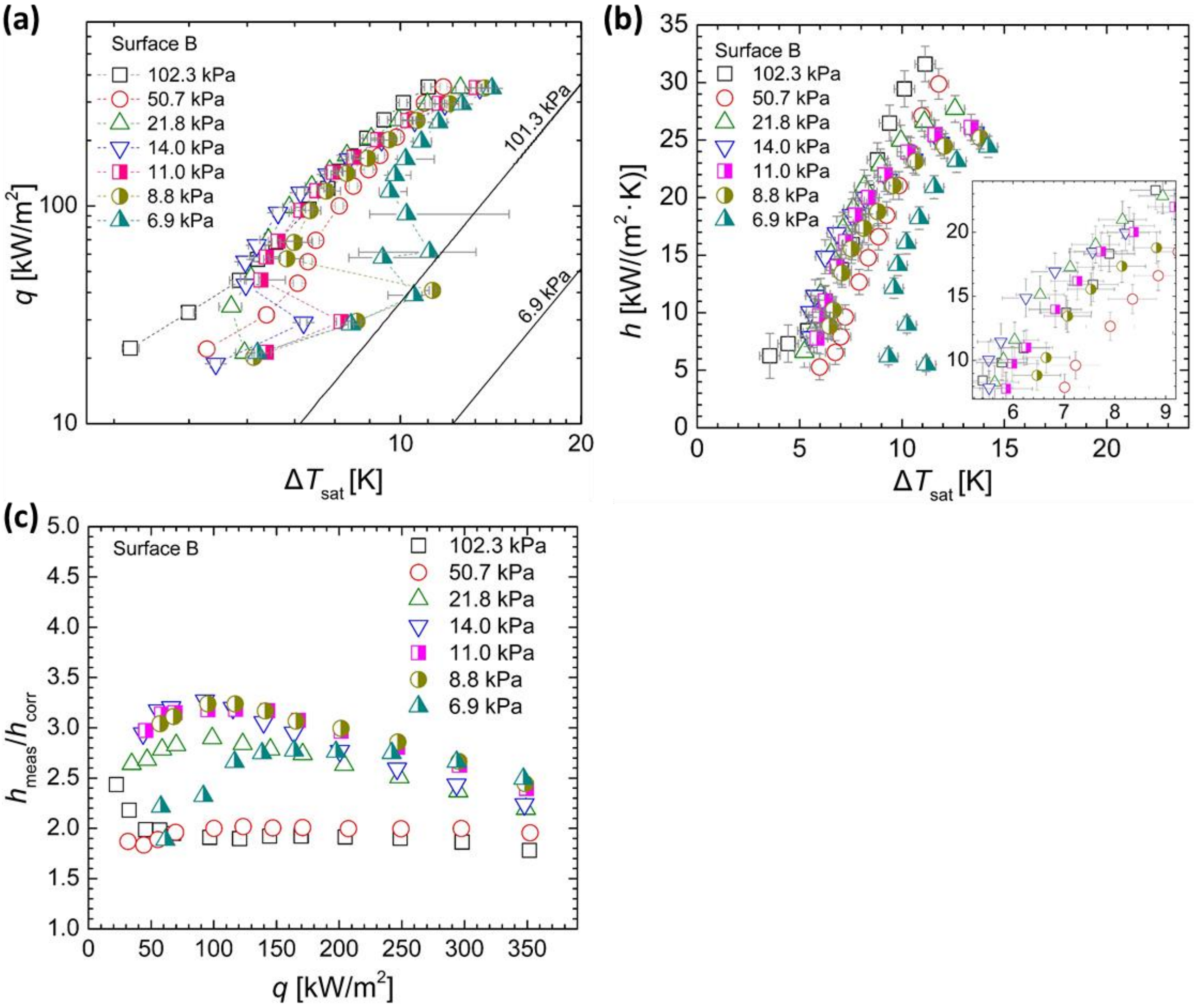

Figure 4.11 (a) Boiling curves and (b) HTC (after ONB) obtained on Surface B at different pressures. Error bars in (a) and (b) show the maximal and minimal values over two minutes' measurements in the steady state and the measurement uncertainty, respectively. The solid lines in (a) represent the calculations of eq. (4.3) at $P = 101.3$ kPa and 6.9 kPa. (c) The corresponding $h_{\mathrm{meas}}/h_{\mathrm{corr}}$ vs q.

Table 4.4 The effect of the pressure level on ΔT_{ONB} of Surface B.

P [kPa]	102.3	50.7	21.8	14.0	11.0	8.8	6.9
ΔT_{ONB} [K]	1.6	4.8	5.5	6.9	8.0	11.3	10.6

performed by controlling q, but not T_{w}). On the other hand, effect of system pressure on heat transfer performance is significantly different from that on a normal metal surface. Specifically, HTC decreases at $P = 50.7$ kPa; however, HTCs of $P = 21.8$-8.8 kPa are equal to or greater than that in the atmospheric condition at $q \leq 200$ kW/m^2. Then, HTC suddenly deteriorates at 6.9 kPa, where data show a wide scatter at $q \leq 100$ kW/m^2. For an enhancement ratio of HTC (Fig. 4.11c), $h_{\mathrm{meas}}/h_{\mathrm{corr}}$ are almost the same between $P = 102.3$ and 50.7 kPa. The pressure, at which $h_{\mathrm{meas}}/h_{\mathrm{corr}}$ becomes the maximum, changes in the order of $P = 14.0$, 11.0, 8.6, and 6.9 kPa as q increases since higher q is needed to reach stable continuous boiling at lower pressure, as mentioned later.

As described in Sub-section 4.3.1, fluctuation of T_{w} is useful to estimate boiling behavior. Fig. 4.12 indicates relationship between *SD* of T_1 and q at the respective pressures, where data before ONB is omitted. *SD* is kept almost constant (≈ 0.5 °C) at $P \geq 21.8$ kPa. In addition, from an observation of boiling behavior (Fig. 4.13a and b), bubbles continuously depart from the all hydrophobic spots at the pressures. Base on the two points, the boiling behavior at $P \geq 21.8$ kPa can be regarded as stable continuous boiling. In the range of $P \leq 14.0$ kPa, *SD* at low q increases as P decreases. Additionally, under lower P, enlarged *SD* is maintained at higher q. Bubble generation from some hydrophobic spots becomes intermittent at $P = 14.0$ kPa and low q (see Fig. 4.6b). At $P = 8.8$ kPa, more unstable bubble behavior is obtained, where a few random spots are intermittently activated in the low heat flux region (Fig. 4.13c).

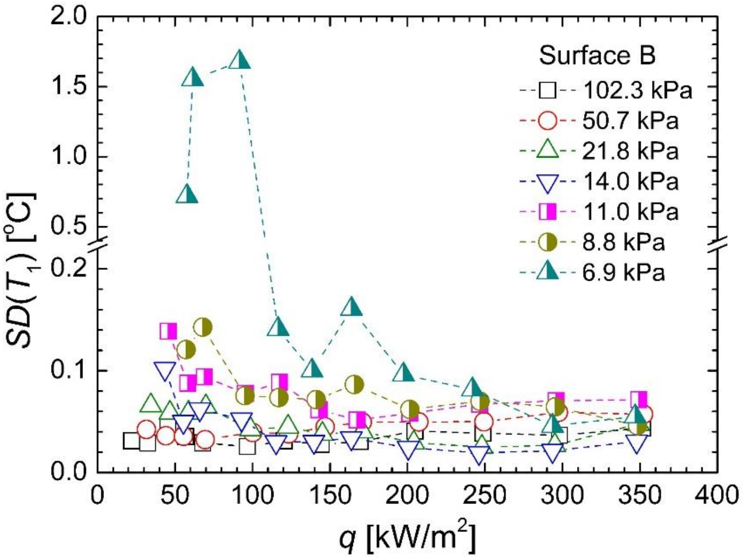

Figure 4.12 Relationships between *SD* of T_1 and q on Surface B at various pressures. Data before ONB is omitted. Notice that the vertical axis is broken for visibility.

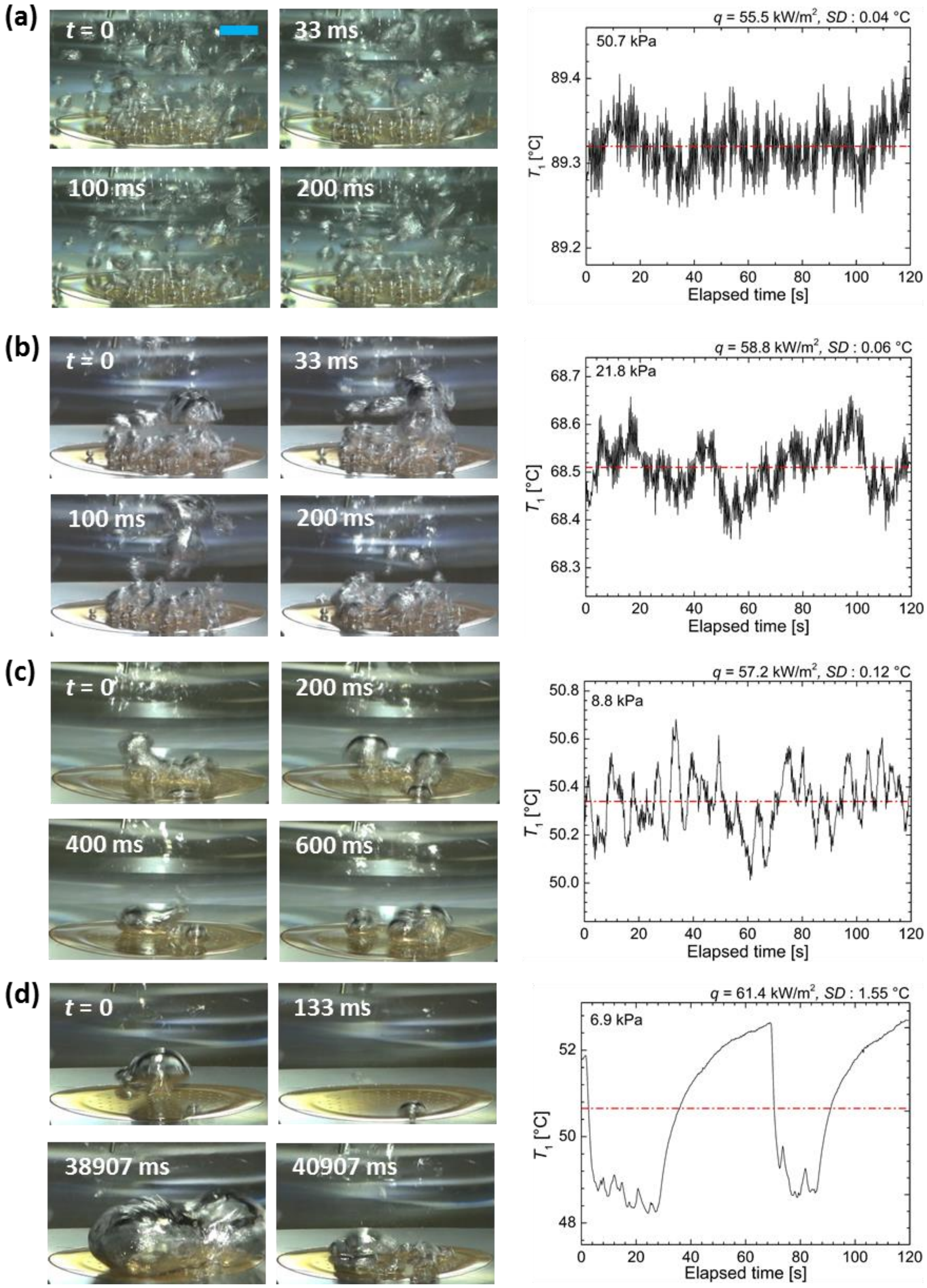

Figure 4.13 Evolutions of boiling behavior (left panels) and the corresponding transient measurements of T_1 during two minutes in the steady state (right panels) on Surface B at $q \approx 60$ kW/m^2 and $P =$ (a) 50.7 kPa, (b) 21.8 kPa, (c) 8.8 kPa, and (d) 6.9 kPa. Blue scale bar: 10 mm. The red-dot-dash lines in the right panels represent the mean values.

However, a some spot is always activated, and bubble generation is never ceased completely at P = 8.8-14.0 kPa. This pressure range is, hence, considered as a transition regime from continuous to intermittent boiling. Waiting periods for tens of seconds is finally introduced at P = 6.9 kPa (Fig. 4.13d), resulting in drastic increase in *SD* (Fig. 4.12). From the above observation, it is revealed that the biphilic surface can significantly lower the transition pressure from continuous to intermittent boiling, but not totally suppress an occurrence of intermittent boiling.

Based on boiling behavior in Fig. 4.13, HTC deterioration at P = 50.7 kPa, seen in Fig. 4.11, is explained as follows. As mentioned above, heat transfer enhancement under low pressures is caused by promoted departure of coalesced bubbles due to a low vapor density. However, most of the departed bubbles at P = 50.7 kPa are isolated in the low heat flux region (see Fig. 4.13a). The lack of facilitated bubble detachment is supposed to cause the decrease in HTC at P = 50.7 kPa compared with the atmospheric pressure and $P \leq 21.8$ kPa. The change of P, which gives the maximum $h_{\mathrm{meas}}/h_{\mathrm{corr}}$, with increasing q can be explained by using Fig. 4.12. At low pressures, q is needed to be larger than a certain value to sustain stable continuous boiling. In addition, HTC of the stable continuous boiling is less affected by pressure level, excluding the high heat flux region where liquid recirculation to the surface is interrupted (see Fig. 4.11b). As a result, the pressure giving the highest $h_{\mathrm{meas}}/h_{\mathrm{corr}}$ decreases as q increases along with an appearance of the stable continuous boiling.

As shown in Fig. 4.11a boiling curve of P = 6.9 kPa gradually approaches to those of the higher pressures as q rises. In addition, *SD* tends to decrease at q = 100 kW/m^2, which becomes comparable to that in the atmospheric condition at $q \geq 293.7$ kW/m^2. Fig. 4.14 shows boiling behavior and the corresponding transient temperature measurements of T_1 at q = 164.0 kW/m^2 and 293.7 kW/m^2, respectively. At q = 164.0 kW/m^2, bubbles are vigorously generated from several random hydrophobic spots, where the complete waiting period is not introduced (Fig.

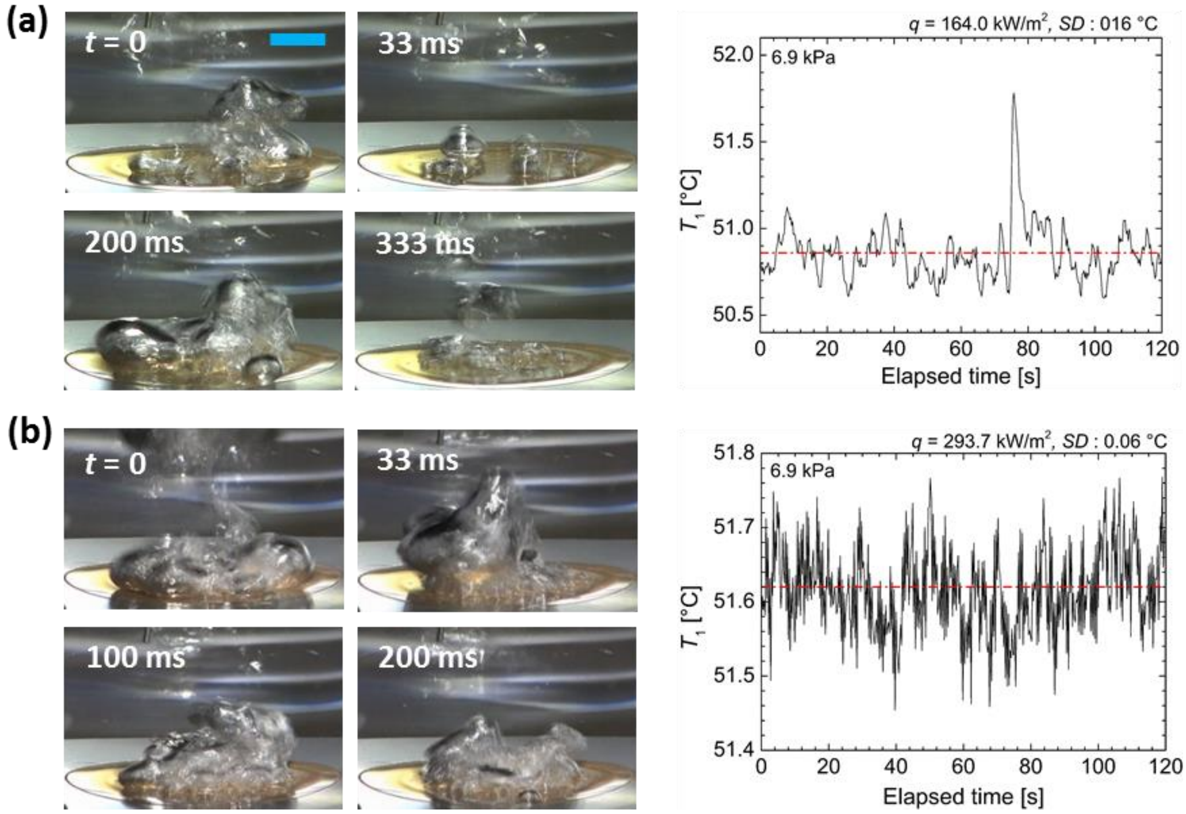

Figure 4.14 Evolutions of boiling behavior (left panels) and the corresponding transient temperature measurements of T_1 during two minutes in the steady state (right panels) on Surface B at $P = 6.9$ kPa, and $q =$ (a) 164.0 kW/m^2 and (b) 293.7 kW/m^2. Blue scale bar: 10 mm. The red-dot-dash lines in the right panel represent the mean values.

4.14a). Such transition region appears from $q = 100$ kW/m^2 to 250 kW/m^2 while increasing the number of nucleation sites. Eventually, the all hydrophobic spots are activated at $q \geq 293.7$ kW/m^2 and T_1 is maintained stably (Fig. 4.14b). Hence, boiling behavior shifts from intermittent to stable continuous boiling as q increases at 6.9 kPa. Similar result was observed in previous studies using normal metal surfaces [56, 130, 133]. In the papers, the transition was considered to result from shortening of time for reconstruction of a superheated liquid layer with increasing q. As mentioned later, however, intermittent boiling on biphilic surfaces is considered to be triggered by condensation of residual bubbles on hydrophobic spots. Thus, the transition in the present study is supposed to be due to suppression of the condensation with the help of high q.

4.3.4 Comparison with previous studies

The present biphilic surface shows great heat transfer enhancement at low ΔT_{sat} due to the facilitation of bubble generation on hydrophobic spots. Table 4.5 summarizes HTC comparison (at $\Delta T_{\mathrm{sat}} \approx 10$ K) of the present result and recent studies for enhancement of sub-atmospheric pool boiling of water and water-based liquid. Compared with flat [145] or nanostructured [144, 163] surfaces, our surface has the highest HTC. Although surfaces with fin structures or screen mesh [140, 141, 164] show better HTC due to the enlarged heat transfer area, it is considered that the biphilic surface is an excellent way to enhance sub-atmospheric boiling in terms of HTC based on the actual heat transfer area (not projected area). In addition, HTC monotonically decreases as P decreases among the previous works. To the best of my knowledge, the reverse pressure effect (described in Sub-section 4.3.3) has been firstly observed in this study.

Table 4.5 Comparison of the present result and recent studies for enhancement of sub-atmospheric pool boiling of water and water-based liquid.

Source	Surface / Liquid	P [kPa]	h [kW/(m^2·K)]*
Present study	Biphilic surface / Water	8.8	21.0
		11.0	24.0
		21.8	24.9
Liu et al. [145]	Plain surface / Water-based nanofluid	20.0	11.6
Kwark et al. [144]	Nanoparticle-coated surface / Water	20.0	8.2
Arya et al. [163]	Nano-structured thin wire / Water	12.4	0.37
Pal et al. [141]	Multiple layered fin surface / Water	9.7	36.3
Chan et al. [140]	Fin surface / Water	9	57.0
Sloan et al. [164]	Multiple layered screen mesh / Water	20.3	127.7

*HTC at $\Delta T_{\mathrm{sat}} \approx 10$ K.

4.4 Single bubble behavior

In the present section, the influence of system pressure on behaver of a single bubble is described. Bubble behavior and TPCL motion were observed at various sub-atmospheric pressures using a surface with a single hydrophobic spot (having different diameters). From the observation, a bubble departure diameter and bubble growth rate are obtained, which were compared with the existing correlations.

4.4.1 Bubble behavior and TPCL motion

To investigate the influence of system pressure on bubble behavior in detail, a single bubble growing from a hydrophobic spot was observed by the high-speed camera. Experiments were carried out with copper surfaces ($\theta \approx 80^{\circ}$) having a single hydrophobic spot, made of the PTFE spray coating ($\theta \approx 120^{\circ}$), at its center (see Sub-section 2.1.3).

Figure 4.15 indicates evolutions of bubble behavior on a surface with φ = 0.5 mm spot at a heat input of 30 W and various pressures, where the moment of departure is set as $t = 0$. At P = 103.9 kPa (Fig. 4.15a), TPCL of the bubble is always pinned at the edge of the spot during bubble growth and departure processes, as with the previous studies [110, 118]. In addition, part of vapor is remained on the spot after the detachment, which works as a nucleus for the next bubble. By contrast, this pinning effect is lost under the sub-atmospheric conditions. At P = 49.2 kPa, TPCL is depinned from the border and moves toward hydrophilic side during the growth process. As a result a contact diameter, d_{c}, is enlarged to more than 1 mm ($t = -5$ ms in Fig 4.15b), leading to a larger departure diameter, d_{d}, compared with the atmospheric condition. The residual bubble is remained on the spot after the departure in the condition. At a lower P of 33.0 kPa, the depinning of TPCL becomes more apparent ($t = -7$ ms in Fig. 4.15c), where d_{d} reaches 15 mm. Such departure of large bubble possibly causes a long waiting period on a normal metal surface; however, on the biphilic surface, TPCL is

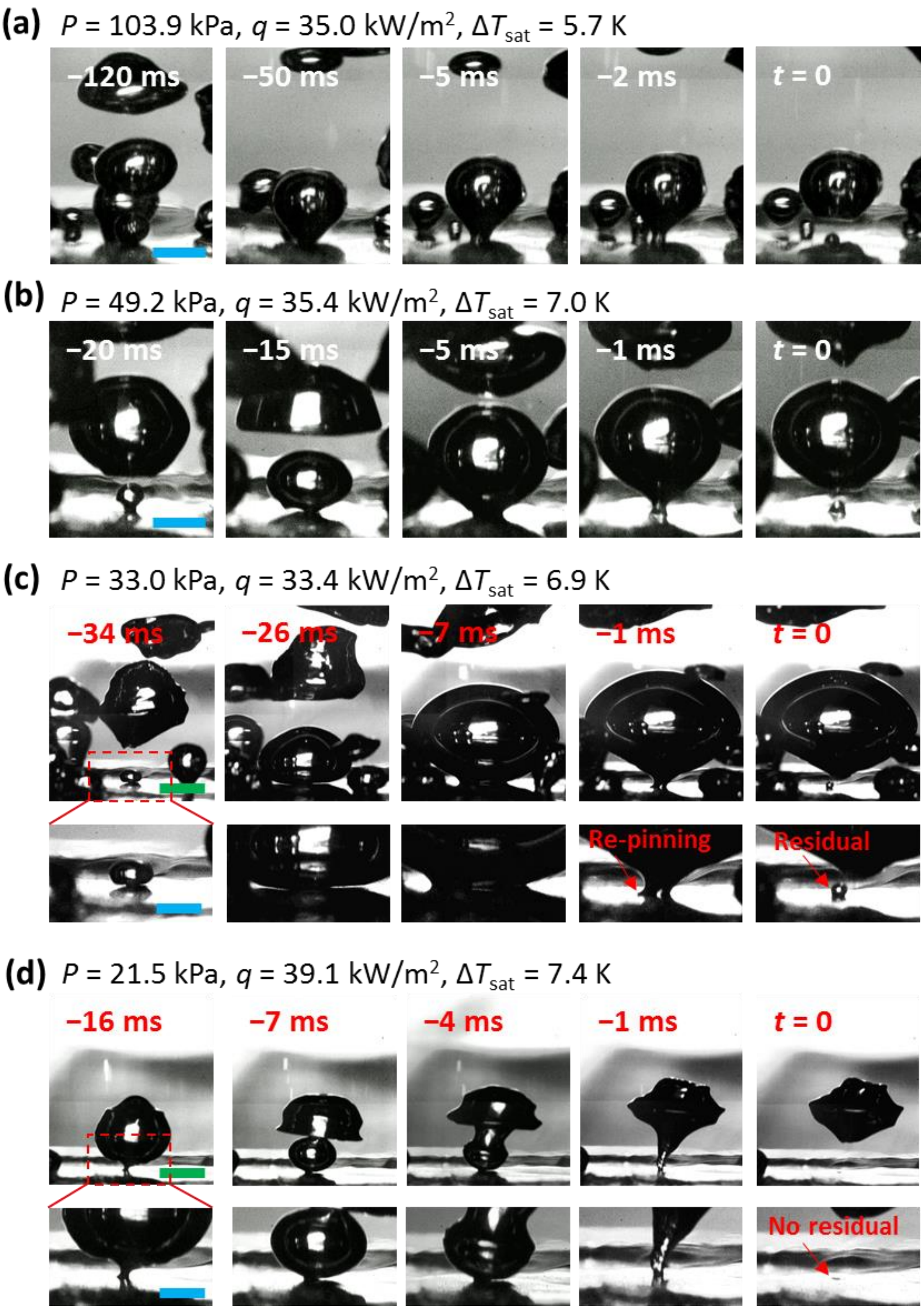

Figure 4.15 Evolutions of single bubble behavior growing from a hydrophobic spot (φ = 0.5 mm) at $P =$ (a) 103.9 kPa, (b) 49.2 kPa, (c) 33.0 kPa and (d) 21.5 kPa. The bottom panels in (c) and (d) are enlarged views of a vicinity of the heating surface (pointed out with a red-dot line). Blue scale bar: 2 mm. Green scale bar: 4 mm.

pinned at the border again (re-pinning) during the departure process ($t = -1$ ms in Fig. 4.15c), and then, the residual vapor is left on the spot after the bubble detachment. Since the next bubble grows from the residue, the essentially continuous bubble growth and departure are repeated, as same with the atmospheric condition. Conversely, a complete bubble departure without the residual vapor is observed at $P = 21.5$ kPa. In the condition, a bubble on the spot is drawn into the wake induced by a forgoing bubble, and eventually, the bubble departs from the surface while merging into the forgoing bubble ($t = -7$--1 ms in Fig. 4.15d). After the departure, the spot is exposed to the liquid due to an absence of a residual vapor ($t = 0$ in Fig. 4.15d). Consequently, a waiting period of hundreds of seconds is introduced until the next bubble generation. By further decreasing P, bubble generation from the spot is completely ceased. From the above observation, it is suggested that biphilic surface can sustain continuous boiling at pressure where a residual bubble is remained on a hydrophobic spot, and a disappearance of the residue triggers intermittent boiling.

Figure 4.16 shows behavior of the complete bubble departure at various pressures and heat inputs with several spot diameters. In the all conditions, the center portion of a bubble on the surface is raised during the growth process due to the wake, where the convex part penetrates the forgoing bubble. Then, in the departure process, the bubble rises while decreasing its volume. As seen in Fig. 4.16c, TPCL is re-pinned at the edge of the spot just before the bubble departure ($t = -2$ ms in Fig. 4.16c). Subsequently, a thin vapor film is formed on the spot ($t = -1$ ms in Fig. 4.16c); however the vapor then disappears 1 ms later ($t = 0$ in Fig. 4.16c), resulting in the complete bubble departure. As described in Sub-section 4.2.1, liquid adjacent to the surface (above the superheated liquid layer) is remarkably subcooled at low pressures owing to the hydrostatic pressure. Since the departed bubble is condensed (apparent at $t = 0$-2 ms in Fig. 4.16c), strong wake of the subcooled water, induced by the forgoing bubble, brings significant cooling effect in a vicinity of the surface. From the above, it is considered that condensation of vapor, which has been trapped on the spot, causes the disappearance of the residual bubble.

(a) φ = 2.0 mm, P = 17.0 kPa, q = 64.2 kW/m^2, ΔT_{sat} = 10.1 K

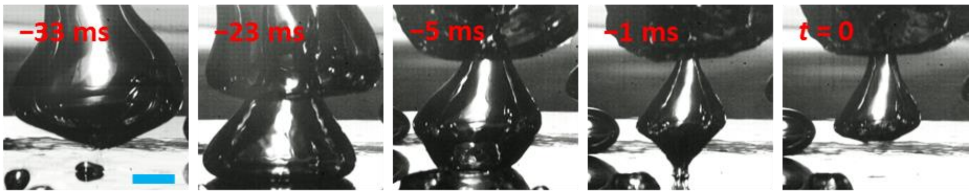

(b) φ = 3.8 mm, P = 13.5 kPa, q = 16.6 kW/m^2, ΔT_{sat} = 6.0 K

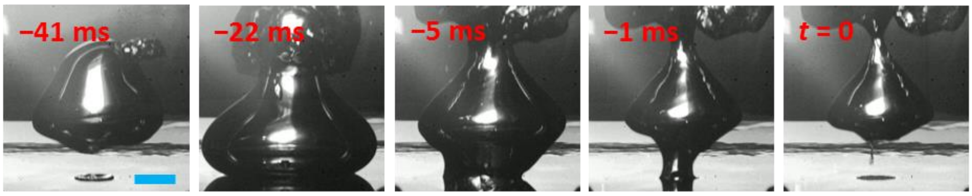

(c) φ = 3.8 mm, P = 13.5 kPa, q = 29.4 kW/m^2, ΔT_{sat} = 9.8 K

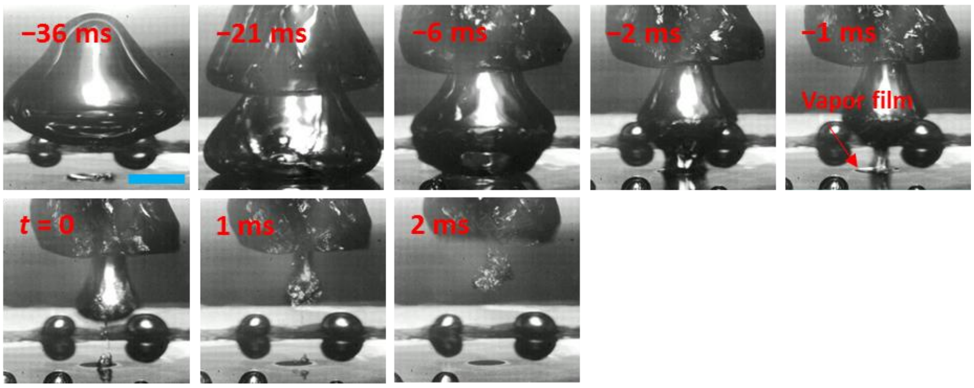

Figure 4.16 Behavior of the complete bubble departure at various pressures and heat inputs with several spot diameters. Blue scale bar: 5 mm.

4.4.2 Bubble departure diameter

Similar experiments were conducted at various pressures and heat inputs with surfaces having different spot diameters, φ, to measure a bubble departure diameter, d_d. The results are shown in Fig. 4.17, where 20 measurement values are plotted for the respective pressures. The blue and red solid lines (d_{Zuber} and d_{Cole}) are the calculations of the Zuber's (eq. (1.12)) and Cole's correlations (eq. (1.13)), respectively.

In $\varphi = 0.5$ mm (Fig. 4.17a), all the data converge on d_{Zuber} at the atmospheric pressure. As described in Sub-section 1.2.3, Zuber's model is based on the assumption that d_c is kept constant. Since TPCL of a bubble is pinned at the edge of the hydrophobic spot in the condition (shown in 4.15a), the experimental result shows the good agreement with d_{Zuber}. On the other hand, at low pressures, departures of several large bubbles with the depinned TPCL and small bubbles with the pinned TPCL alternately occur, resulting in large scatter of d_{d}. Although the variation of d_{d} is supposed to be caused by change in T_{w} near the spot, the local

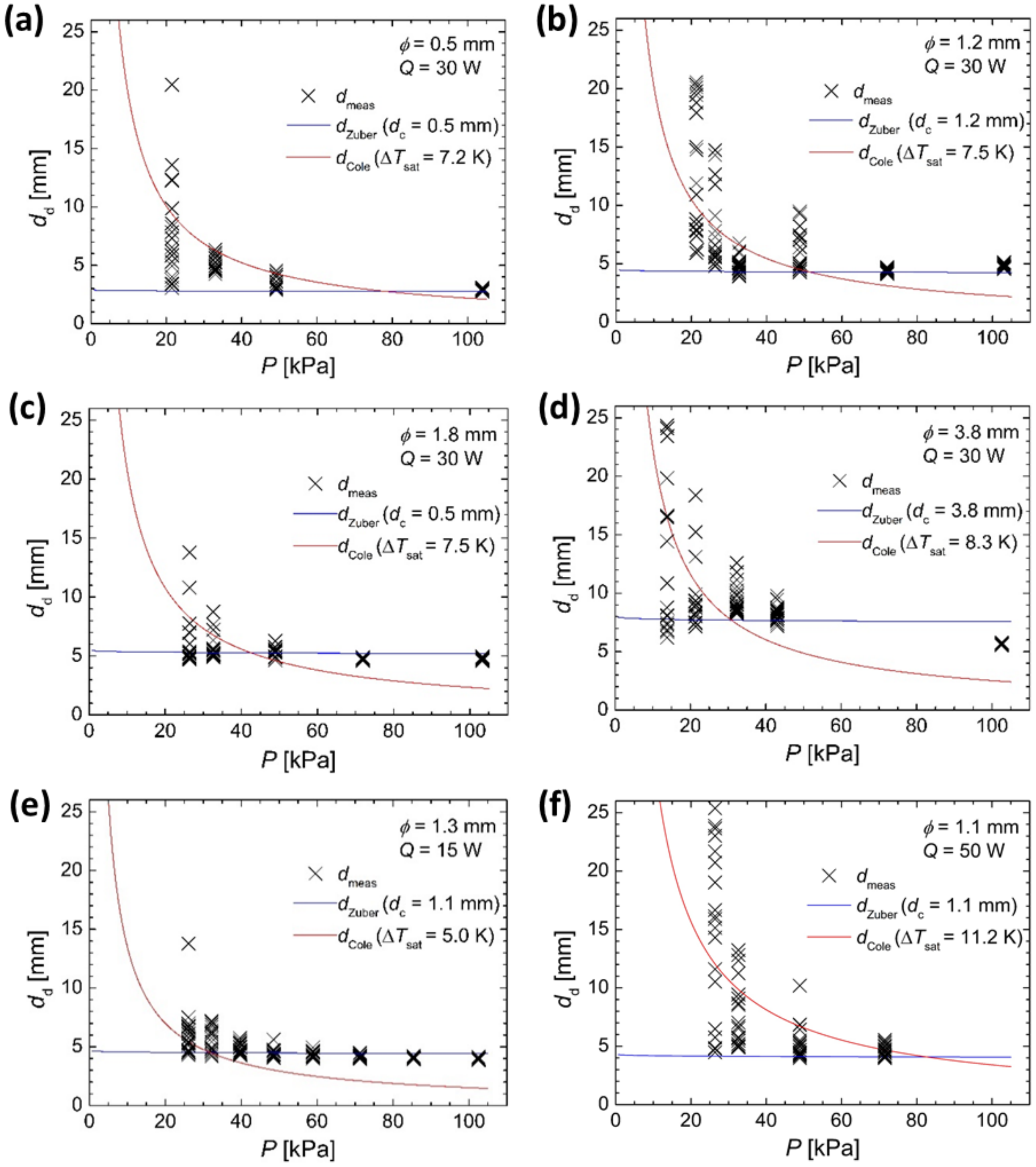

Figure 4.17 Bubble departure diameter, d_{d}, of surfaces with different hydrophobic spot diameters at various heat input, Q, and P. Blue and red solid lines are calculations of eq. (1.12) and (1.13), respectively.

temperature cannot be obtained in the present experimental apparatus. The fluctuation of d_d is enlarged at lower P, which is generally distributed between d_Zuber and d_Cole. In $\varphi = 1.2$ mm and $Q = 30$ W (Fig. 4.17b), the pinning of TPCL is sustained even at $P = 72$ kPa. As a result, d_d at the pressure is also in good agreement with d_Zuber. Then, d_d varies largely due to the depinning of TPCL at $P < 72$ kPa. Under all the other condition, d_d converges at a certain value as far as the pinning of TPCL is available, regardless of pressure.

From a closer examination of Fig. 4.17a and b, and f with the magnitude relation between d_Zuber and d_Cole taken into account, $d_\mathrm{d} \approx d_\mathrm{Zuber}$ is obtained (namely, TPCL is pinned) in the range of $d_\mathrm{Zuber} > d_\mathrm{Cole}$, whereas fluctuation of d_d increases due to the depinned TPCL at P where $d_\mathrm{Zuber} < d_\mathrm{Cole}$. As for the other conditions (Fig. 4.17c, d, and e), the correlation is apparently not satisfied; however d_d at the atmospheric pressure are not estimated properly with Zuber's correlation in such conditions. Although φ is used as d_c for the calculation of d_Zuber in Fig. 4.17, the actual bubble departure follows the necking appeared on the interface. Therefore, practically, an adhesion force due to surface tension in the experiments differs from the Zuber's model. This difference becomes more significant as φ increases, leading to the large deviation between obtained d_d and d_Zuber. However, bubble departure on the biphilic surfaces is supposed to be dominated by the balance of the static forces at atmospheric condition and low heat fluxes because of the moderate bubble growth. Hence the nature of the bubble departure is the same as the Zuber's model. Based on the concept, eq. (1.12) is modified by multiplying by a constant factor, so that d_Zuber coincides with d_d at the atmospheric pressure. Fig. 4.18 shows TPCL behavior map (pinning or depinning) with φ as the horizontal axis and normalized pressure P/P^* as the vertical axis. P^* corresponds to a pressure where the modified d_Zuber ($d_\mathrm{Zuber}{}^*$) is equal to d_Cole. The map includes data obtained with heat inputs of 15, 30, and 50 W. As shown in the figure, transition from pinning to depinning occurs at $P/P^* \approx 1$, regardless of φ—depinning takes place in conditions with $d_\mathrm{Cole} > d_\mathrm{Zuber}{}^*$, in other words, $d_\mathrm{d} \approx$

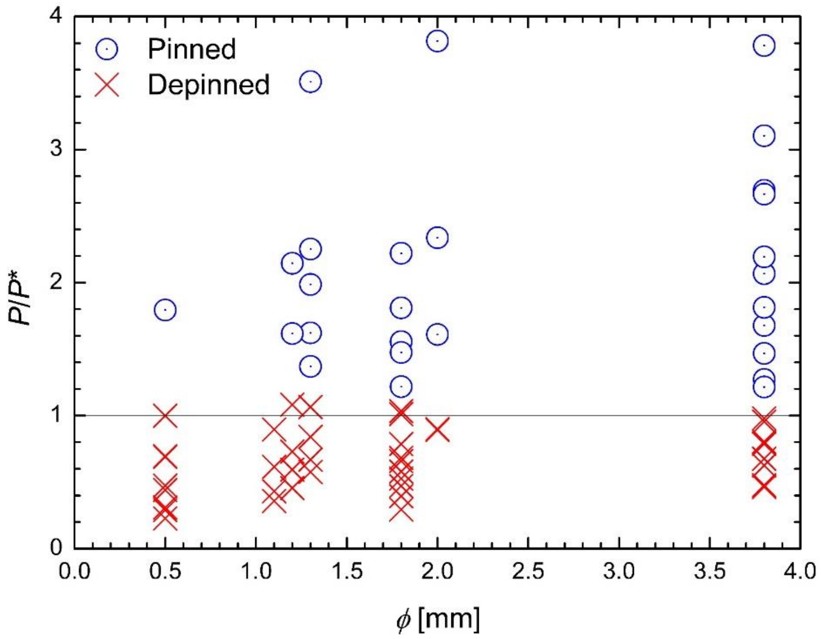

Figure 4.18 TPCL behavior map (pinned or depinned). The vertical axis is the system pressure normalized with P^*, corresponding the pressure where $d_{\mathrm{Zuber}}{}^*$ becomes equal to d_{Cole}.

$d_{\mathrm{Zuber}}{}^*$ is obtained, regardless of P in the range of $d_{\mathrm{Zuber}}{}^* > d_{\mathrm{Cole}}$. Here, the Cole's model is a correlation for a uniform and moderate wettability surfaces. Therefore, this result means that d_{d} can be increased to $d_{\mathrm{Zuber}}{}^*$ in the conditions where $d_{\mathrm{d}} < d_{\mathrm{Zuber}}{}^*$ on a normal surface; however, expansion of TPCL cannot be suppressed by adding hydrophobic spots under conditions where $d_{\mathrm{d}} > d_{\mathrm{Zuber}}{}^*$ on a normal surface. As described in Sub-section 1.4.1, depinning of TPCL was reported at the atmospheric pressure and $\Delta T_{\mathrm{sat}} \approx 7$ K in boiling on a biphilic surface having hydrophobic spots with $\varphi = 100$ μm in the previous study of Jo et al. [111]. P^* at $\varphi = 100$ μm and $\Delta T_{\mathrm{sat}} = 7$ K is calculated to be 178. 8 kPa, which is far above the atmospheric pressure. Hence, the depinning of TPCL occurs even at the atmospheric (and may be also pressurized) condition, when φ is chosen very small.

4.4.3 Bubble growth rate

From the observation of bubble behavior, bubble growth rate was also investigate under conditions close to the border between the pinned and depinned. Fig. 4.19 shows evolutions of a bubble height (distance between the bottom and apex), H, and width, W, and averaged bubble radius, r_{ave}, under pinned and depinned conditions, where r_{ave} is derived by taking an average of H and W. The measurements were taken every 1 ms. Under the depinned condition, depinning of TPCL occurred at the arrowed point. It is well known that bubble growth mechanisms are generally divided into two types: inertia-dominated and heat transfer-dominated, which appear in the initial and later stage, respectively. The theoretical equation for the former and the latter were proposed by Rayleigh [165], and Plesset and Zwick [166], respectively, as below.

$$r(t) = \left\{ \frac{2}{3} \left(\frac{T_\infty - T_{\mathrm{sat}}}{T_{\mathrm{sat}}} \right) \frac{L_{\mathrm{lv}} \rho_{\mathrm{v}}}{\rho_{\mathrm{l}}} \right\}^{1/2} t \tag{4.5}$$

$$r(t) = 2\sqrt{\frac{3}{\pi}} Ja \sqrt{\alpha_l t} \tag{4.6}$$

where a_{l} is thermal diffusivity of liquid. The blue and red solid lines in the bottom panels of

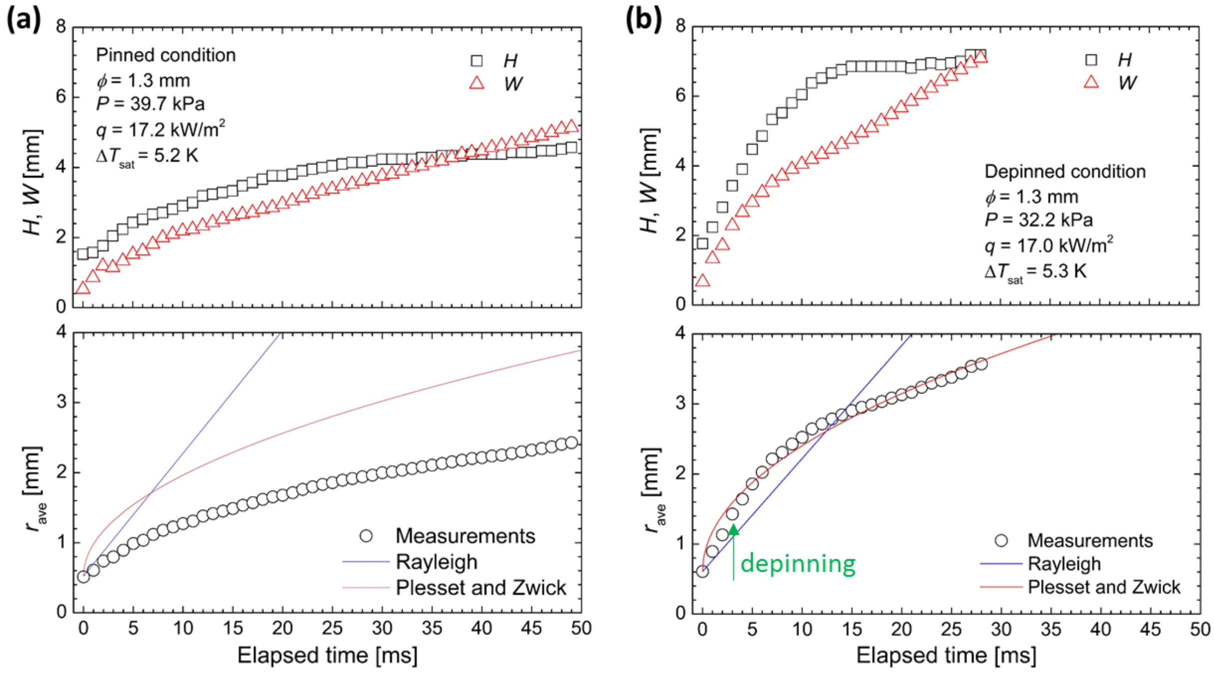

Figure 4.19 Evolutions of a bubble height, H, and width, W, (top panels) and averaged bubble radius, r_{ave}, (bottom panels) under (a) pinned and (b) depinned conditions, where r_{ave} is derived by taking an average of H and W. Under the depinned condition, depinning of TPCL occurs at the arrowed point.

Fig.4.19 are the calculations based on the two equations. In the above equation, T_∞ needs to be decided properly, which is not a bulk liquid temperature because liquid adjacent to the bubble is superheated. Since temperature profile in a vicinity of the bubble is not obtained in the present study, the film temperature (the arithmetic mean of T_{bulk} and T_{w}) is used in the calculations. In addition, taking a residual bubble on the hydrophobic spot into account, $r_{\mathrm{ave}}(t = 0)$ of the equations is offset to fit the actual value at $t = 0$.

Under the pinned condition, the bubble growth rate is remarkably lower than those of the two equations. However, an index for a power-law-approximation of the result (namely, n of $r_{\mathrm{ave}} = t^n$) is 0.39, which more or less matches that of Plesset and Zwick's correlation ($n = 0.5$). Thus, bubble growth in the pinned condition can be regarded as heat transfer-dominant mode. The reason for the discrepancy from eq. (4.6) is considered to be because evaporation is suppressed compared with a normal surface due to a shorter length of TPCL pinned at the edge of the hydrophobic spot. By contrast, the bubble growth rate in the depinned condition is in good agreement with eq. (4.6). Therefore, the hydrophobic spot does not affect bubble behavior after the depinning, excluding remaining of a residual bubble.

4.5 Summary

In this chapter, boiling heat transfer experiment and single bubble experiment were conducted to investigate the effect of system pressure on boiling from biphilic surfaces. The main findings through them are summarized as follows.

(1) At $P = 14.0$ kPa, ΔT_{ONB} on a biphilic surface is reduced by 12 K, and HTC is improved by six times (comparison at the same ΔT_{sat}), compared with a mirror-finished copper surface. Intermittent boiling occurs on the copper surface at the reduced pressure, whereas stable continuous boiling is sustained on the biphilic surface. As a result, T_{w} on the biphilic surface is stabilized extremely.

(2) A surface with a small diameter and pitch (Surface A) shows the highest HTC at $P \approx 14.0$ kPa, excluding the initial stage of boiling. Since behaviors of bubble coalescence are different, the effect of system pressure on HTC differs from surface to surface.

(3) The biphilic surface can maintain continuous boiling at lower P, compared with the copper surface. HTC of surfaces with a small diameter (Surface A and B) are less affected by pressure level in the continuous boiling region, and then, it suddenly deteriorates due to transition to intermittent boiling. Moreover, on surface with a small diameter and a large pitch (Surface B), HTC increases as P decreases at places. The inverse effect of pressure has not been reported yet, to the best of author's knowledge

(4) The present biphilic surfaces have a superior performance compared with the previous studies, in terms of HTC based on the actual heat transfer area (not projected area).

(5) In low pressure conditions, TPCL is depinned from the border between a hydrophobic and hydrophilic domains, and moves toward a hydrophilic side. At a pressure above a certain value, TPCL is re-pinned at the border during the departure process, resulting in a residual vapor on the spot after the detachment. However, the residual bubble disappears due to cooling effect of surrounding subcooled liquid, and then a long waiting period is introduced The disappearance of the residual bubble is considered as the trigger of intermittent boiling on biphilic surfaces.

(6) Bubble departure diameter, d_{d}, converges at a certain value as far as TPCL is pinned, regardless of pressure. Under the depinned condition, fluctuation of d_{d} is enlarged as P decreases. A pressure at the border of the pinned and depinned conditions is in good agreement with P^*, where departure diameters derived from the modified Zuber's correlation ($d_{\mathrm{zuber}}{}^*$) and Cole's equation (d_{cole}) coincide with each other.

(7) Bubble growth rate under the pinned condition is remarkably lower than those of theoretical equations due to a shorter length of TPCL. By contrast, the growth rate of a

depinned bubble agrees well with Plesset and Zwick's correlation (where heat transfer-dominated mode is considered), which means the hydrophobic spot does not affect bubble behavior after the depinning, excluding remaining of a residual bubble.

Chapter 5

Conclusions

This thesis aimed to reveal the effect of dissolved air and system pressure on pool boiling from biphilic surfaces. The main outcomes are summarized as follow.

In Chapter 1, outlines of engineering importance and research history of boiling phenomenon were given. Basic characteristics of boiling and related physics were also introduced. The status and objectives of this study were specified based on a literature survey regarding to effect of wettability modification, dissolved air, and system pressure.

In Chapter 2, a detailed description about heating surfaces was given. TiO_2 sputtering was employed to fabricate a superhydrophilic surface. Hydrophobic surfaces were made by PTFE-spray coating, P-HNT coating, and Ni/TFEO electroplating. Contact angle and surface topology of the resulting surfaces were measured by means of $\theta/2$ method, and SEM and laser microscopy, respectively.

In Chapter 3, effect of dissolved air on subcooled boiling from biphilic surfaces were described. Two experimental apparatuses, open and closed types, were developed in this study. By taking different degassing procedures for the respective apparatuses, two contrasting conditions were obtained: gassy subcooled (containing the saturation amount of dissolved air) and pure subcooled (where dissolved air was thoroughly eliminated). Boiling heat transfer experiment and single bubble experiment were conducted under each condition to investigate the effect of dissolved air on heat transfer performance, bubble behavior, and temperature profiles inside a bubble. In addition single bubble behavior was numerically simulated by using the diffuse interface model. Consequently, distribution of noncondensable gas and surrounding liquid motion were obtained. The heat transfer mechanism was considered based on comparison between experimental and numerical results. The main findings through them are summarized as follows.

(1) ΔT_{ONB} shifts from negative values in the gassy subcooled condition to positive values in the pure subcooled condition: namely, ONB at negative ΔT_{sat} does not occur without sufficient presence of dissolved air even on hydrophobic surfaces. In addition, the result can be explained well by Torikai's model [121]

(2) Boiling curves of the two conditions almost overlap with each other at $\Delta T_{\mathrm{sat}} \leq -2$ K and ≥ 12 K. HTC is enhanced in the range of -2 K $< \Delta T_{\mathrm{sat}} <$ 12 K under the gassy subcooled condition due to latent heat transport and Marangoni convection induced by bubbles stably attaching on hydrophobic spots

(3) A bubble height is decided by the balance between the saturation temperature of the bubble (reduced by non-condensable gas) and a temperature of the surrounding liquid. In the pure subcooled boiling, thus, bubbles cannot grow large enough to depart from the surface because of lack of dissolved air.

(4) The numerical simulation revealed the strong interfacial flow, tangential to the surface, is induced only in the two component systems (water + nitrogen), because of the enlarged surface tension difference between the apex and bottom of the bubble. This tangential flow corresponds to the Marangoni flow.

In Chapter 4, the effect of system pressure on boiling from biphilic surfaces was experimentally investigated. Boiling heat transfer and single bubble experiments were conducted under various pressure conditions. Specifically, HTCs of three different biphilic surfaces and a mirror finished copper surface were compared at the atmospheric and reduced ($P \approx 14.0$ kPa) pressures. Boiling characteristics were examined in the pressure range from the atmospheric and down to 6.9 kPa, using a biphilic surface. In addition, on surfaces having a single hydrophobic spot, bubble behavior and TPCL motion were observed with the help of a high-speed camera. Departure diameter and growth rate were also measured. The main finding through them are summarized as follows.

(1) At P = 14.0 kPa, ΔT_{ONB} on a biphilic surface is reduced by 12 K, and HTC is improved by six times (comparison at the same ΔT_{sat}), compared with a mirror-finished copper surface. On the biphilic surface, extremely-stabilized wall temperatures are obtained at the reduced pressure.

(2) A surface with a small diameter and pitch (Surface A) shows the highest HTC at $P \approx$ 14 kPa, excluding the initial stage of boiling. Since behaviors of bubble coalescence are different, the effect of system pressure on HTC differs from surface to surface.

(3) The biphilic surface can maintain continuous boiling at a lower pressure, compared with the copper surface. HTC of surfaces with a small diameter (Surface A and B) are less affected by pressure level in the continuous boiling region, and then, it suddenly deteriorates due to transition to intermittent boiling. Moreover, on surface with a small diameter and a large pitch (Surface B), HTC increases as P decreases in a certain pressure range.

(4) In low pressure conditions, TPCL is depinned from the border between a hydrophobic and hydrophilic domains, and moves toward a hydrophilic side. A departed bubble leaves a residual vapor on the hydrophobic spot owing to re-pinning of TPCL at a pressure above a certain value; however, the residue disappears at the lower pressures due to cooling effect of surrounding subcooled liquid. The disappearance of the residual bubble is considered as the trigger of intermittent boiling on biphilic surfaces.

(5) Bubble departure diameter, d_{d}, converges at a certain value as far as TPCL is pinned, regardless of pressure. Under the depinned condition, fluctuation of d_{d} is enlarged as

P decreases. A pressure at the border of the pinned and depinned conditions is in good agreement with P^*, where calculations of the modified Zuber's correlation ($d_{\mathrm{zuber}}{}^*$) and Cole's equation (d_{cole}), coincide with each other.

These are the outcomes through the present study. Boiling characteristics on biphilic surfaces were firstly measured in the pure subcooled condition. As a result, the effect of dissolved air on heat transfer performance and bubble behavior has been clarified. The influence of system pressure was also investigated for the first time. Consequently, it has been revealed that biphilic surfaces enable to lowering of transition pressure to intermittent boiling and remarkable enhancement in HTC. Additionally, new findings such as a disappearance of a residual bubble and inverse pressure effect on HTC were obtained.

As mentioned above, the effect of system pressure on HTC differs from surface to surface—The optimum pattern depends on pressure as well as heat flux. Hence, a comprehensive correlation, including non-dimensional parameters of bubble departure diameter and size of a hydrophobic spot, needs to be developed to predict HTC under various conditions.

Acknowledgement

I would like to express my gratitude to all who have contributed to my study at Thermofluid and Physics Laboratory in Kyushu University. Firstly, I deeply appreciate my supervisor, Prof. Yasuyuki Takata, for his guidance, patient, and encouragement, as well as for giving valuable opportunities. Without his understanding and personal support, I could not complete this thesis.

I also would like to thank the Dissertation Committee Members, Prof. Koji Takahashi and Prof. Masamichi Kohno, for agreeing to participate in the review process and making many suggestions and comments.

I would like to thank Dr. Naoya Sakoda and Prof. Kan'ei Shinzato for providing helpful discussion during laboratory meetings. I also would like to thank Ms. Mituko Shuto for her kind support.

I sincerely appreciate Dr. Sumitomo Hidaka for his time and help in constructing my experiments. I also would like to thank Mr. Takeshi Matoba for his technical support.

I would like to express my sincere gratitude to Dr. Biao Shen for helpful discussions. He frequently provided very thoughtful suggestions and helped with writing papers. I also would like to thank Dr. Orejon, Dr. Harish, Dr. Alexandros, and Dr. Kuroki for their kindness and support.

I wish to express my warm thanks to past and present members of our laboratory, especially members of the boiling group: Dr. Suroto, Ms. Hirabayashi, Dr. He, Mr. Furusato, Mr. Imamura, Mr. Mine, Mr. Hamazaki, and Mr. Ikeda.

I acknowledge the financial support from I^{2}CNER in Kyushu University.

Lastly, I dearly appreciate my family who have always respected my will and helped me through my studies.

References

[1] K. Teramoto, Innovating survey on the boiler technologies (in Japanese), *Survey Reports on the Systemization of Technologies*, vol. 7, 2007.

[2] https://www.tlv.com/ja/articles/articles_009.html.

[3] S-J. Chen, A. A. Tseng, Spray and jet cooling in steel rolling, *International Journal of Heat and Fluid Flow*, vol. 13, no. 4, pp. 358-369, 1992.

[4] H. Zhang, S. Shao, H. Xu, H. Zou, C. Tian, Free cooling of datacenters: A review, *Renewable & Sustainable Energy Reviews*, vol. 35, pp. 171-182, 2014.

[5] M. Zhang, Z. Liu, G. Ma, The experimental investigation on thermal performance of a flat two-phase thermosyphon, *International Journal of Thermal Sciences*, vol. 47, no. 9, pp. 1195-1203, 2008.

[6] H. Kubota, Y. Takata, T. Ito, M. Iwakuni, K. Funaki, Boiling heat transfer characteristics of subcooled nitrogen (in Japanese), *TEION KOGAKU (Journal of Cryogenics and Superconductivity Society of Japan)*, vol. 37, no. 9, pp. 485-491, 2002.

[7] L. Benkheira, B. Baudouy, M. Souhar, Heat transfer characteristics of two-phase He I (4.2 K) thermosiphon flow, *International Journal of Heat and Mass Transfer*, vol.50, no. 17-18, pp. 3534-3544, 2007.

[8] https://www.jraia.or.jp/product/heatpump/i_broke.html.

[9] A. Hepbasli, A key review on exergetic analysis and assessment of renewable energy resources for a sustainable future, *Renewable & Sustainable Energy Reviews*, vol. 12, pp. 593-661, 2008.

[10] K. J. Chua, S. K. Chou, W. M. Yang, Advances in heat pump systems: A review, *Applied Energy*, vol. 87, no. 12, pp. 3611-3624, 2010.

[11] Z. Song, X. Zhang, C. Eriksson, Data center energy and cost saving evaluation, *Energy Procedia*, vol. 75, pp. 1255-1260, 2015.

[12] M. Dayarathna, Y. Wen, R. Fan, Data center energy consumption modeling: A survey, *IEEE Communications Surveys & Tutorials*, vol. 18, no. 1, pp. 732-794, 2016.

[13] Agency for Natural Resources and Energy, Energy white paper 2017, 2017.

[14] http://www.nedo.go.jp/activities/ZZJP_100097.html.

[15] Y. Katto, Science of boiling (1) (in Japanese), *Journal of the Heat Transfer Society of*

Japan, vol. 44, no. 186, pp. 38-42, 2005.

[16] R. M. Manglik, On the advancements in boiling, two-phase flow heat transfer, and interfacial phenomena, *Journal of Heat Transfer-Transactions of ASME*, vol. 128, no. 12, pp. 1237-1242, 2006.

[17] S. Nukiyama, The maximum and minimum values of the heat Q transmitted from metal to boiling water under atmospheric pressure, *International Journal of Heat and Mass Transfer*, vol. 9, no. 12, pp. 1419-1433, 1966.

[18] K. Nishikawa, Historical developments in the research of boiling heat transfer, *JSME International Journal*, vol. 30, no. 264, pp. 897-905, 1987.

[19] S. G. Bankoff, A. J. Hajjar, B. B. McMlothin, On the nature and location of bubble nuclei in boiling from surfaces, *Journal of Applied Physics*, vol. 29, no. 12 pp. 1739-1741, 1958.

[20] H. K. Forster, N. Zuber, Growth of a vapor bubble in a superheated liquid, *Journal of Applied Physics*, vol. 25, no. 4, pp. 474-478, 1954.

[21] R. Cole, L. Shulma, Bubble growth rates at high Jakob numbers, *International Journal of Heat and Mass Transfer*, vol. 9, no. 12, pp. 1377-1390, 1966.

[22] R. F. Gaertner, Photographic study of nucleate pool boiling on a horizontal surface, *Journal of Heat Transfer-Transactions of ASME*, vol. 87, no. 1, pp. 17-27, 1965.

[23] M. G. Cooper, A. J. P. Lloyd, The microlayer in nucleate pool boiling, *International Journal of Heat and Mass Transfer*, vol. 12, no. 8, pp. 895-913, 1969.

[24] W. M. Rohsenow, A method of correlating heat transfer data for surface boiling of liquids, *MIT Technical Report No. 5,* 1951.

[25] S. S. Kutateladze, Heat transfer in condensation and boiling, State Scientific and Technical Publishers of Literature on Machinery, 1952.

[26] K. Nishikawa, K. Yamagata, On the correlation of nucleate boiling heat transfer, *International Journal of Heat and Mass Transfer*, vol. 1, no. 2-3, pp. 219-235, 1960.

[27] N. Zuber, Hydrodynamic aspects of boiling heat transfer, Ph.D. thesis, University of California, Los Angeles, 1959.

[28] P. J. Berenson, Film-boiling heat transfer from a horizontal surface, *Journal of Heat Transfer-Transactions of ASME*, vol. 83, no. 3, pp. 351-356, 1961.

[29] W. Nakayama, T. Daikoku, H. Kuwahara, K. Kakizaki, High-flux heat transfer surface

"THERMOEXCEL" (in Japanese), *Hitachi Review*, vol. 57, no. 8, pp. 1-4, 1975.

[30] C. F. Gottzmann, P. S. O'Neill, P. E. Minton, High efficiency heat exchanger, *Chemical Engineering Progress*, vol. 69, no. 7, pp. 69-75, 1973.

[31] S. K. Das, N. Putra, W. Roetzel, Pool boiling characteristics of nano-fluids, *International Journal of Heat and Mass Transfer*, vol. 46, no. 5, pp. 851-862, 2003.

[32] S. Onishi, H. Ohta, N. Ohtani, Y. Fukuyama, H. Kobayashi, Boiling heat transfer by nucleate boiling of immiscible liquids, *Interfacial Phenomena and Heat Transfer*, vol. 1, no. 1, pp. 63-80, 2013.

[33] H. Sakashita, A. Ono, Y. Nakabayashi, Measurements of critical heat flux and liquid–vapor structure near the heating surface in pool boiling of 2-propanol/water mixtures, *International Journal of Heat and Mass Transfer*, vol. 53, no. 7-8, pp. 1554-1562, 2010.

[34] M. Shojaeian, A. Kosar , Pool boiling and flow boiling on micro- and nanostructured surfaces, *Experimental Thermal and Fluid Science*, vol. 63, pp. 45-73, 2015.

[35] D. E. Kim, D. I. Yu, D. W. Jerng, M. H. Kim, H. S. Ahn, Review of boiling heat transfer enhancement on micro/nanostructured surfaces, *Experimental Thermal and Fluid Science*, vol. 66, pp. 173-196, 2015.

[36] D. Attinger, C. Frankiewicz, A. R. Betz, T. M. Schutzius, R. Ganguly, A. Das, C. J. Kim, C. M. Megaridis, Surface engineering for phase change heat transfer: A review, *MRS Energy & Sustainability*, vol. 1, no. E4, pp. 1-40, 2014.

[37] S. Mori, K. Okuyama, Enhancement of the critical heat flux in saturated pool boiling using honeycomb porous media, *International Journal of Multiphase Flow*, vol. 35, no. 10, pp. 946-951, 2009.

[38] N. Nagai, S. Nishio, Pool boiling on a single-crystal sapphire surface: A measuring method of quantities upon liquid-solid contacts (in Japanese), *Transactions of the Japan Society of Mechanical Engineers Series B*, vol. 61, no. 588, pp. 3018-3023, 1995.

[39] F. Demiray, J. Kim, Microscale heat transfer measurements during pool boiling of FC-72: Effect of subcooling, *International Journal of Heat and Mass Transfer*, vol. 47, no. 14-16, pp. 3257-3268, 2004.

[40] T. Yabuki, O. Nakabeppu, Heat transfer mechanisms in isolated bubble boiling of water observed with MEMS sensor, *International Journal of Heat and Mass Transfer*, vol. 76, pp. 286-297, 2014.

[41] T. H. Kim, E. Kommer, S. Dessiatoun, J. Kim, Measurement of two-phase flow and heat transfer parameters using infrared thermometry, *International Journal of Multiphase Flow*, vol. 40, pp. 56-67, 2012.

[42] Y. Utaka, K. Nakamura, A. Sakurai, K. Itagaki, H. Sonoda, Configuration of micro-layer in nucleate boiling (in Japanese), *Transactions of the Japan Society of Mechanical Engineers Series B*, vol. 74, no. 747, pp. 98-104, 2008.

[43] S. G. Kandlikar, Handbook of PHASE CHANGE: Boiling and Condensation, CRC Press, 1999.

[44] The Japan Society of Mechanical Engineers, JSM Textbook Series Heat Transfer (in Japanese), Maruzen Publishing, 2005.

[45] The Japan Society of Mechanical Engineers, Boiling heat transfer and cooling (in Japanese), JAPAN INDUSTRIAL PUBLISHING, 1989.

[46] J. Kim, Review of nucleate pool boiling bubble heat transfer mechanisms, *International Journal of Multiphase Flow*, vol. 35, no. 12, pp. 1067-1076, 2009.

[47] Y. Koizumi, M. Shoji, M. Monde, Y. Takata, N. Nagai, Boiling- Research and Advances, Elsevier, 2017.

[48] M. M. Rahman, J. Pollack, M. McCarthy, Increasing boiling heat transfer using low conductivity materials, *Scientific Reports*, vol. 5, 13145, 2015.

[49] P. A. Raghupathi, S. G. Kandlikar, Effect of thermophysical properties of the heater substrate on critical heat flux in pool boiling, *Journal of Heat Transfer-Transactions of ASME*, vol. 139, no. 11, 111502, 2017.

[50] T. Inoue, N. Kawae, M. Monde, Effect of subcooling on critical heat flux during pool boiling on a horizontal heated wire, *Heat and Mass Transfer*, vol. 33, no. 5-6, pp. 481-488, 1998.

[51] M. Shoji, L. C. Witte, S. Sankaean, The influence of surface conditions and subcooling on film-transition boiling, *Experimental Thermal and Fluid Science*, vol. 3, no. 3, pp. 280-290, 1990.

[52] R. L. Judd, H. Merte, M. E. Ulucakli, Variation of superheat with subcooling in nucleate pool boiling, *Journal of Heat Transfer-Transactions of ASME*, vol. 113, no. 1, pp. 201-208, 1991.

[53] D. P. Shatto, G. P. Peterson, Pool boiling critical heat flux in reduced gravity, *Journal*

of Heat Transfer-Transactions of ASME, vol. 121, no. 4, pp. 865-873, 1999.

[54] P. Di Marco, W. Grassi, Motivation and results of a long-term research on pool boiling heat transfer in low gravity, *International Journal of Thermal Sciences*, vol. 41, no. 7, pp. 567-585, 2002.

[55] R. Raj, J. Kim, J. McQuillen, Gravity scaling parameter for pool boiling heat transfer, *Journal of Heat Transfer-Transactions of ASME*, vol. 132, no. 9, 091502, 2010.

[56] K. Nishikawa, Y. Fujita, Y. Nawata, The effect of pressure on heat transfer and bubble behavior at saturated nucleate boiling (in Japanese), *Transactions of the Japan Society of Mechanical Engineers*, vol. 42, no. 361, pp. 2879-2891, 1976.

[57] H. Sakashita, A. Ono, Boiling behaviors and critical heat flux on a horizontal plate in saturated pool boiling of water at high pressures, *International Journal of Heat and Mass Transfer*, vol. 52, no. 3-4, pp. 744-750, 2009.

[58] D. Gorenflo, E. Baumhogger, T. Windmann, G. Herres, Nucleate pool boiling, film boiling and single-phase free convection at pressures up to the critical state. Part I: Integral heat transfer for horizontal copper cylinders, *International Journal of Refrigeration*, vol. 33, no. 7, pp. 1229-1250, 2010.

[59] K. Nishikawa, H. Kusuda, K. Yamasaki, K. Tanaka, Nucleate boiling at low liquid levels, *Bulletin of JSME*, vol. 10, no. 38, pp. 328-338, 1967.

[60] P. J. Berenson, Experiments on pool-boiling heat transfer, *International Journal of Heat and Mass Transfer*, vol. 5, no. 10, pp. 985-999, 1962.

[61] J. Kim, S. Jun, R. Laksnarain, S. M. You, Effect of surface roughness on pool boiling heat transfer at a heated surface having moderate wettability, *International Journal of Heat and Mass Transfer*, vol. 101, pp. 992-1002, 2016.

[62] D. S. Jung, J. E. S. Venart, A. C. M. Sousa, Effects of enhanced surfaces and surface orientation on nucleate and film boiling heat transfer in R-11, *International Journal of Heat and Mass Transfer*, vol. 30, no. 12, pp. 2627-2639, 1987.

[63] K. N. Rainey, S. M. You, Effects of heater size and orientation on pool boiling heat transfer from microporous coated surfaces, *International Journal of Heat and Mass Transfer*, vol. 44, no. 14, pp. 2589-2599, 2001.

[64] S. G. Kandlikar, A theoretical model to predict pool boiling CHF incorporating effects of contact angle and orientation, *Journal of Heat Transfer-Transactions of ASME*, vol.

123, no. 6, pp. 1071-1079, 2001.

[65] S. M. Kwark, M. Amaya, R. Kumar, G. Moreno, S. M. You, Effects of pressure, orientation, and heater size on pool boiling of water with nanocoated heaters, *International Journal of Heat and Mass Transfer*, vol. 53, no. 23-24, pp. 5199-5208, 2010.

[66] U. Magrini, E. Nannei, On the influence of the thickness and thermal properties of heating walls on the heat transfer coefficients in nucleate pool boiling, *Journal of Heat Transfer-Transactions of ASME*, vol. 97, no. 2, pp. 173-178, 1975.

[67] N. R. Prasad, J. S. Saini, R. Prakash, The effect of heater wall thickness on heat transfer in nucleate pool-boiling at high heat flux, *International Journal of Heat and Mass Transfer*, vol. 28, no. 7, pp. 1367-1375, 1985.

[68] J. Y. Chang, S. M. You, Boiling heat transfer phenomena from microporous and porous surfaces in saturated FC-72, *International Journal of Heat and Mass Transfer*, vol. 40, no. 18, pp. 4437-4447, 1997.

[69] S. G. Liter, M. Kaviany, Pool-boiling CHF enhancement by modulated porous-layer coating: Theory and experiment, *International Journal of Heat and Mass Transfer*, vol. 44, no. 22, pp. 4287-4311, 2001.

[70] W. Nakayama, T. Daikoku, H. Kuwahara, T. Nakajima, Dynamic model of enhanced boiling heat transfer on porous surfaces, *Journal of Heat Transfer-Transactions of ASME*, vol. 102, no. 3, pp. 445-450, 1980.

[71] R. L. Webb, C. Pais, Nucleate pool boiling data for five refrigerants on plain, integral-fin and enhanced tube geometries, *International Journal of Heat and Mass Transfer*, vol. 35, no. 8, pp. 1893-1904, 1992.

[72] J. J. Wei, H. Honda, Effects of fin geometry on boiling heat transfer from silicon chips with micro-pin-fins immersed in FC-72, *International Journal of Heat and Mass Transfer*, vol. 46, no. 21, pp. 4059-4070, 2003.

[73] J. Ogata, A. Yabe, Basic study on the enhancement of nucleate boiling heat transfer by applying electric fields, *International Journal of Heat and Mass Transfer*, vol. 36, no. 3, pp. 775-782, 1993.

[74] S. Laohalertdecha, P. Naphon, S. Wongwises, A review of electrohydrodynamic enhancement of heat transfer, *Renewable & Sustainable Energy Reviews*, vol. 11, pp. 858-876, 2007.

[75] K-A. Park, A. E. Bergles, Ultrasonic enhancement of saturated and subcooled pool boiling, *International Journal of Heat and Mass Transfer*, vol. 31, no. 3, pp. 664-667, 1988.

[76] H-Y. Kim, Y. G. Kim, B. H. Kang, Enhancement of natural convection and pool boiling heat transfer via ultrasonic vibration, *International Journal of Heat and Mass Transfer*, vol. 47, no. 12-13, pp. 2831-2840, 2004.

[77] A. Nakazima, Solid Surface Wettability and its Control (in Japanese), Uchida Rokakuho Publishing, 2007.

[78] R. N. Wenzal, Surface roughness and contact angle, *The Journal of Physical and Chemistry*, vol. 53, no. 9, pp. 1466-1467, 1949.

[79] A. B. D. Cassie, S. Baxter, Wettability of porous surface, *Transections of the Faraday Society*, vol. 40, pp. 546-551, 1944.

[80] C. P. Costello, W. J. Frea, A salient non-hydrodynamic effect on pool boiling burnout of small semi-cylindrical heaters, *Chemical Engineering Progress Symposium Series*, vol. 61, no. 57, pp. 258-268, 1965.

[81] K. Torikai, T. Yamazaki, Boiling heat transfer in an unwettable surface (in Japanese), *Transactions of the Japan Society of Mechanical Engineers*, vol. 32, no. 242, pp. 1557-1561, 1966.

[82] S. Hasegawa, R. Echigo, K. Koga, Maximum heat fluxes for pool boiling on partly poor wettable heating surfaces: Part 1, on the visual observation of boiling and the temperature profiles of heating surface (in Japanese), *Transactions of the Japan Society of Mechanical Engineers*, vol. 34, no. 268, pp. 2182-2190, 1968.

[83] S. Hasegawa, R. Echigo, T. Takegawa, Maximum heat fluxes for pool boiling on partly ill-wettable heating surfaces: Part 2, mainly on the nucleate boiling having tolerably high superheat (in Japanese), *Transactions of the Japan Society of Mechanical Engineers*, vol. 38, no. 315, pp. 2927-2934, 1972.

[84] T. Takegawa, S. Hasegawa, R. Echigo, Boiling heat transfer on ill-wettable surface: On bubble behavior (in Japanese), *Transactions of the Japan Society of Mechanical Engineers*, vol. 39, no. 320, pp. 1288-1296, 1973.

[85] Y. Yasukawa, Boiling heat transfer of a narrow and ill-wettable heating surface on which a single bubble grows (in Japanese), *Transactions of the Japan Society of Mechanical*

Engineers Series B, vol. 46, no. 401, pp. 121-128, 1980.

[86] K. Torikai, K. Suzuki, T. Kaneko, Effect of condition of heating surface on pool boiling heat transfer: On boiling for unwettable surface and grooving surface (in Japanese), *Transactions of the Japan Society of Mechanical Engineers Series B*, vol. 55, no. 511, pp. 767-769, 1989.

[87] Y. Nam, J. Wu, G. Warrier, Y. S. Ju, Experimental and numerical study of single bubble dynamics on a hydrophobic surface, *Journal of Heat Transfer-Transactions of ASME*, vol. 131, no. 12, 121004, 2009.

[88] Y. Takata, S. Hidaka, S. Uraguchi, Boiling feature on a super water-repellent surface, *Heat Transfer Engineering*, vol. 27, no. 8, pp. 25-30, 2006.

[89] C-C. Hsu, P-H. Chen, Surface wettability effects on critical heat flux of boiling heat transfer using nanoparticle coatings, *International Journal of Heat and Mass Transfer*, vol. 55, no. 13-14, pp. 3713-3719, 2012.

[90] S. A. Kovalev, An investigation of minimum heat fluxes in pool boiling of water, *International Journal of Heat and Mass Transfer*, vol. 9, no. 11, pp. 1219-1226, 1966.

[91] K. Nishikawa, S. Hasegawa, H. Honda, S. Sakaguchi, Studies on boiling characteristic curve: 1st report, the effects of bulk subcooling and surface conditions on heat transfer (in Japanese), *Transactions of the Japan Society of Mechanical Engineers*, vol. 34, no. 257, pp. 134-141, 1968.

[92] S. K. R. Chowdhury, R. H. S. Winterton, Surface effects in pool boiling, *International Journal of Heat and Mass Transfer*, vol. 28, no. 10, pp. 1881-1889, 1985.

[93] M. Maracy, R. H. S. Winterton, Hysteresis and contact angle effects in transition pool boiling of water, *International Journal of Heat and Mass Transfer*, vol. 31, no. 7, pp. 1443-1449, 1988.

[94] Y. Takata, S. Hidaka, M. Masuda, T. Ito, Pool boiling on a superhydrophilic surface, *International Journal of Energy Research*, vol. 27, no. 2, pp. 111-119, 2003.

[95] Y. Takata, S. Hidaka, J. M. Cao, T. Nakamura, H. Yamamoto, M. Masuda, T. Ito, Effect of surface wettability on boiling and evaporation, *Energy*, vol. 30, no. 2-4, pp. 209-220, 2005.

[96] Y. Chen, D. Mo, H. Zhao, N. Ding, S. Lu, Pool boiling on the superhydrophilic surface with TiO_2 nanotube arrays, *Science in China Series E: Technological Sciences*, vol. 52,

no. 6, pp. 1596-1600, 2009.

[97] L. Liao, R. Bao, Z. H. Liu, Compositive effects of orientation and contact angle on critical heat flux in pool boiling of water, *Heat and Mass Transfer*, vol. 44, no. 12, pp. 1447-1453, 2008.

[98] E. Forrest, E. Williamson, J. Buongiorno, L-W. Hu, M. Rubner, R. Cohen, Augmentation of nucleate boiling heat transfer and critical heat flux using nanoparticle thin-film coatings, *International Journal of Heat and Mass Transfer*, vol. 53, no. 1-3, pp. 58-67, 2010.

[99] W. Wu, H. Bostanci, L. C. Chow, Y. Hong, M. Su, J. P. Kizito, Nucleate boiling heat transfer enhancement for water and FC-72 on titanium and silicon oxide surfaces, *International Journal of Heat and Mass Transfer*, vol. 53, no. 9-10, pp. 1773-1777, 2010.

[100] C-K. Huang, C-W. Lee, C-K. Wang, Boiling enhancement by TiO_2 nanoparticle deposition, *International Journal of Heat and Mass Transfer*, vol. 54, no. 23-24, pp. 4895-4903, 2011.

[101] R. Chen, M-C. Lu, V. Srinivasan, Z. Wang, H. H. Cho, A. Majumdar, Nanowires for enhanced boiling heat transfer, *Nano Letters*, vol. 9, no. 2, pp. 548-553, 2009.

[102] D. Lee, T. Kim, S. Park, S. S. Lee , S. H. Ko, Zinc oxide nanowire forest for pool boiling heat transfer, *Japanese Journal of Applied Physics*, vol. 51, 11PE11, 2012.

[103] H. S. Ahn, J. Kim, M. H. Kim, Investigation of pool boiling critical heat flux enhancement on a modified surface through the dynamic wetting of water droplet, *Journal of Heat Transfer-Transactions of ASME*, vol. 134, no. 7, 071504, 2012.

[104] H-J. Jo, S-H. Kim, H. Kim, J. Kim, M. H. Kim, Nucleate boiling performance on nano/microstructures with different wetting surface, *Nanoscale Research Letters*, vol. 7, no. 1, 242, 2012.

[105] Y. Nam, E. Aktinol, V. K. Dhir , Y. S. Ju, Single bubble dynamics on a superhydrophilic surface with artificial nucleation sites, *International Journal of Heat and Mass Transfer*, vol. 54, no. 7-8, pp. 1572-1577, 2011.

[106] R. K. Young , R. L. Hummel, Improved nucleate boiling heat transfer, *Chemical Engineering Progress*, vol. 60, no. 7, pp. 53-58, 1964.

[107] Y. Takata, S. Hidaka, M. Kohno, Enhanced nucleate boiling by superhydrophobic coating with checkered and spotted patterns, *Proceedings of ECI International*

Conference on Boiling Heat Transfer, 2006.

[108] Y. Takata, S. Hidaka, M. Kohno, Effect of surface wettability on pool boiling: Enhancement by hydrophobic coating, *International Journal of Air-Conditioning and Refrigeration*, vol. 20, no. 1, 1150003, 2012.

[109] A. R. Betz, J. Xu, H. Qiu, D. Attinger, Do surface with mixed hydrophilic and hydrophobic areas enhance pool boiling?, *Applied Physics Letters*, vol. 97, 141909, 2010.

[110] H-J. Jo, H-S. Ahn, S-H. Kim, M. H. Kim, A study of nucleate boiling heat transfer on hydrophilic, hydrophobic and heterogeneous wetting surface, *International Journal of Heat and Mass Transfer*, vol. 54, no. 25-26, pp. 5643-5652, 2011.

[111] H-J. Jo, S-H. Kim, H. S. Park, M. H. Kim, Critical heat flux and nucleate boiling on several heterogeneous wetting surfaces: Controlled hydrophobic patterns on a hydrophilic substrate, *International Journal of Multiphase Flow*, vol. 62, pp. 101-109, 2014.

[112] A. R. Betz, J. R. Jenkins, C-J. Kim, D. Attinger, Significant boiling enhancement with surfaces combining surperhydrophilic and superhydrophobic patterns, *Proceedings of IEEE 24th International Conference on Micro Electro Mechanical Systems*, pp. 1193-1196, 2011.

[113] A. R. Betz, J. Jenkins, C-J. Kim, D. Attinger, Boiling heat transfer on superhydrophilic, superhydrophobic, and superbiphilic surfaces, *International Journal of Heat and Mass Transfer*, vol. 57, no. 2, pp. 733-741, 2013.

[114] M. Zupančič, M. Steinbucher, P. Gregorčič, I. Golobič, Enhanced pool-boiling heat transfer on laser-made hydrophobic/superhydrophilic polydimethylsiloxane-silica patterned surfaces, *Applied Thermal Engineering*, vol. 91, pp. 288-297, 2015.

[115] C-H. Choi, M. David, Z. Gao, A. Chang, M. Allen, H. Wang, C. Chang, Large-scale generation of patterned bubble arrays on printed bi-functional boiling surfaces, *Scientific Reports*, vol. 6, 23760, 2016.

[116] B. J. Suroto, M. Tashiro, S. Hirabayashi, S. Hidaka, M. Kohno, Y. Takata, Effects of hydrophobic-spot periphery and subcooling on nucleate pool boiling from a mixed-wettability surface, *Journal of Thermal Science and Technology*, vol. 8, no. 1, pp. 294-308, 2013.

[117] M. Tashiro, B. J. Suroto, T. Kakitani, S. Hidaka, M. Kohno, Y. Takata, Subcooled boiling from a surface with spotted patterns of hydrophilic and hydrophobic coatings,

Proceedings of ECI 8th International Conference on Boiling and Condensation Heat Transfer, 2012.

[118] B. Shen, B. J. Suroto, S. Hirabayashi, M. Yamada, S. Hidaka, M. Kohno, K. Takahashi, Y. Takata, Bubble activation from a hydrophobic spot at "negative" surface superheats in subcooled boiling, *Applied Thermal Engineering*, vol. 88, pp. 230-236, 2015.

[119] I. U. Vakarelski, N. A. Patankar, J. O. Marston, D. Y. Chan, S. T. Thoroddsen, Stabilization of Leidenfrost vapour layer by textured superhydrophobic surfaces, *Nature*, vol. 489, pp. 274-277, 2012.

[120] M. Behar, M. Courtaud, R. Ricque, R. Semeria, Fundamental aspects of subcooled boiling with and without dissolved gases, *Proceedings of 3rd International Heat Transfer Conference*, 1966.

[121] K. Torikai, H. Shimamune, F. Fujishiro, The effect of the dissolved gas content upon incipient boiling superheats, *Proceedings of 4th International Heat Transfer Conference*, 1970.

[122] Y. S. Hong, C. N. Ammerman, S. M. You, Boiling characteristics of cylindrical heaters in saturated, gas saturated, and pure-subcooled FC-72, *Journal of Heat Transfer-Transactions of ASME*, vol. 119, no. 2, pp. 313-316, 1997.

[123] R. Jeschar, H. Kraushaar, H. Griebel, Influence of gases dissolved in cooling water on heat transfer during stable film boiling, *Steel Research*, vol. 67, no. 6, pp. 227-234, 1996.

[124] H. Takamatsu, H. Kubo, H. Honda, Immersion cooling of a simulated microelectronic chip with artificial re-entrant cavities (in Japanese), *Transactions of the Japan Society of Mechanical Engineers Series B*, vol. 64, no. 621, pp. 142-148, 1998.

[125] K. N. Rainey, S. M. You, S. Lee, Effect of pressure, subcooling, and dissolved gas on pool boiling heat transfer from microporous, square pin-finned surfaces in FC-72, *International Journal of Heat and Mass Transfer*, vol. 46, no. 1, pp. 23-35, 2003.

[126] A. Cioncolini, L. Santini, M. E. Ricotti, Effects of dissolved air on subcooled and saturated flow boiling of water in a small diameter tube at low pressure, *Experimental Thermal and Fluid Science*, vol. 32, no. 1, pp. 38-51, 2007.

[127] X. Wang, S. Zhao, H. Wang, T. Pan, Bubble formation on superhydrophobic-micropatterned copper surfaces, *Applied Thermal Engineering*, vol. 35, pp. 112-119, 2012.

[128] C. J. Rallis, H. H. Jawurek, Latent heat transport in saturated nucleate boiling,

International Journal of Heat and Mass Transfer, vol. 7, no. 10, pp. 1051-1068, 1964.

[129] S. J. D. van Stralen, R. Cole, W. M. Sluyter, M. S. Sohal, Bubble growth rates in nucleate boiling of water at subatmospheric pressures, *International Journal of Heat and Mass Transfer*, vol. 18, no. 5, pp. 655-669, 1975.

[130] Y. Iida, T. Tsuyuki, K. Kawabata, On the boiling patterns of nucleate pool boiling at reduced pressure (in Japanese), *KAGAKU KOGAKU RONBUNSHU*, vol. 7, no. 5, pp. 459-464, 1981.

[131] C. Casarosa, E. L. Latrofa, The geyser effect in a two-phase thermosyphon, *International Journal of Heat and Mass Transfer*, vol. 26, no. 6, pp. 933-941, 1983.

[132] A. Niro, G. P. Beretta, Boiling regimes in a closed two-phase thermosyphon, *International Journal of Heat and Mass Transfer*, vol. 33, no. 10, pp. 2099-2110, 1990.

[133] W. R. McGillis, J. S. Fitch, W. R. Hamburgen, V. P. Carey, Pool boiling on small heat dissipating elements in water at subatmospheric pressure, *WRL Research Report 91/7*, 1991.

[134] F. Giraud, R. Rulliere, C. Toublanc, M. Clausse, J. Bonjour, Experimental evidence of a new regime for boiling of water at subatmospheric pressure, *Experimental Thermal and Fluid Science*, vol. 60, pp. 45-53, 2015.

[135] R. C. Chu, R. E. Simons, G. M. Chrysler, Experimental investigation of an enhanced thermosyphon heat loop for Cooling of a high performance electronics module, *Proceedings of 15th Annual IEEE Semiconductor Thermal Measurement and Management Symposium*, pp. 1-9, 1999.

[136] A. Pal, Y. K. Joshi, M. H. Beitelmal, C. D. Patel, T. M. Wenger, Design and performance evaluation of a compact thermosyphon, *Components and Packaging Technologies-Transactions of IEEE*, vol. 25, no. 4, pp. 601-607, 2002.

[137] H. Toyoda, Y. Kondo, Effect of non-condensable gas leakage on long term cooling performance of loop thermosyphon, *Journal of Electronics Cooling and Thermal Control*, vol. 3, no. 4, pp. 131-135, 2013.

[138] T. Fujimoto, F. Takeda, Y. Kondo, T. Fujii, T. Kato, Cooling unit for high-density packaging ICT rack by using boiling heat transfer (Evaluation on basic cooling performance of low height type thermosyphon) (in Japanese), *Transactions of the JSME*, vol. 80, no. 815, TEP0202, 2014.

[139] W. R. McGillis, J. S. Fitch, W. R. Hamgurgen, V. P. Carey, Pool boiling enhancement techniques for water at low pressure, *WRL Research Report*, vol. 90, no. 9, 1990.

[140] M. A. Chan, C. R. Yap, K. C. Ng, Pool boiling heat transfer of water on finned surfaces at near vacuum pressures, *Journal of Heat Transfer-Transactions of ASME*, vol. 132, no. 3, 031501, 2010.

[141] A. Pal, Y. Joshi, Boiling of water at subatmospheric conditions with enhanced structures: Effect of liquid fill volume, *Journal of Electronic Packaging-Transactions of ASME*, vol. 130, no. 1, 011010, 2008.

[142] S. J. Penley, R. A. Wirtz, Correlation of subatmospheric pressure, saturated, pool boiling of water on a structured-porous surface, *Journal of Heat Transfer-Transactions of ASME*, vol. 134, no. 8, 081502, 2012.

[143] N. K. Choon, A. Chakraborty, S. M. Aye, W. Xiaolin, New pool boiling data for water with copper-foam metal at sub-atmospheric pressures: Experiments and correlation, *Applied Thermal Engineering*, vol. 26, pp. 1286-1290, 2006.

[144] S. M. Kwark, M. Amaya, S. M. You, Pool boiling heat transfer characteristics of nanocoating in various working fluids, *Proceedings of 27th Annual IEEE Semiconductor Thermal Measurement and Management Symposium*, pp. 146-154, 2011.

[145] Z-H. Liu, X-F. Yang, J. G. Xiong, Boiling characteristics of carbon nanotube suspensions under sub-atmospheric pressures, *International Journal of Thermal Sciences*, vol. 49, no. 7, pp. 1156-1164, 2010.

[146] T-E. Tsai, H-H. Wu, C-C. Chang, S-L. Chen, Two-phase closed thermosyphon vapor-chamber system for electronic cooling, *International Communications in Heat and Mass Transfer*, vol. 37, no. 5, pp. 484-489, 2010.

[147] Z-H. Liu, X-F. Yang, G-S. Wang, G-L. Guo, Influence of carbon nanotube suspension on the thermal performance of a miniature thermosyphon, *International Journal of Heat and Mass Transfer*, vol. 53, no. 9-10, pp. 1914-1920, 2010.

[148] M. M. Sarafraz, F. Hormozi, S. M. Peyghambarzadeh, Role of nanofluid fouling on thermal performance of a thermosyphon: Are nanofluids reliable working fluid?, *Applied Thermal Engineering*, vol. 82, pp. 212-224, 2015.

[149] A. B. Solomon, R. Roshan, W. Vincent, V. K. Karthikeyan, L. G. Asirvatham, Heat transfer performance of an anodized two-phase closed thermosyphon with refrigerant as

working fluid, *International Journal of Heat and Mass Transfer*, vol. 82, pp. 521-529, 2015.

[150] J. Kim, J. F. Benton, D. Wisniewski, Pool boiling heat transfer on small heaters: Effect of gravity and subcooling, *International Journal of Heat and Mass Transfer*, vol. 45, no. 19, pp. 3919-3932, 2002.

[151] R. T. Ferrell, D. M. Himmelblau, Diffusion coefficients of nitrogen and oxygen in water, *Journal of Chemical and Engineering Data*, vol. 12, no. 1, pp. 111-115, 1967.

[152] J. R. Lloyd, W. R. Moran, Natural convection adjacent to horizontal surface of various planforms, *Journal of Heat Transfer-Transactions of ASME*, vol. 96, no. 4, pp. 443-447, 1974.

[153] Y. Nam, Y. S. Ju, Bubble nucleation on hydrophobic islands provides evidence to anomalously high contact angles of nanobubbles, *Applied Physics Letter*, vol. 93, no. 10, 103115, 2008.

[154] T. Nishiyama, K. Takahashi, T. Ikuta, Y. Yamada, Y. Takata, Hydrophilic domains enhance nanobubble stability, *ChemPhysChem*, vol. 17, no. 10, pp. 1500-1504, 2016.

[155] M. Tashiro, Study on boiling heat transfer on surfaces with spotted patterns of hydrophilic and hydrophobic coatings (in Japanese), Master thesis, Kyushu University, Fukuoka, 2013.

[156] N. Zuber, Nucleate boiling. The region of isolated bubbles and the similarity with natural convection, *International Journal of Heat and Mass Transfer*, vol. 6, no. 1, pp. 61-78, 1963.

[157] S. M. Dammer, D. Lohse, Gas enrichment at liquid-wall interfaces, *Physical Review Letters*, vol. 96, no. 20, 206101, 2006.

[158] D. Bratko, A. Luzar, Attractive surface force in the presence of dissolved gas: A molecular approach, *Langmuir*, vol. 24, pp. 1247-1253, 2008.

[159] J. Straub, The role of surface tension for two-phase heat and mass transfer in the absence of gravity, *Experimental Thermal and Fluid Science*, vol. 9, no. 3, pp. 253-273, 1994.

[160] Y. Abe, A. Iwasaki, Observation of vapor bubble of non-azeotropic binary mixture in microgravity with a two-wavelength interferometer, *Proceedings of 5th ASME/JSME Thermal Engineering Joint Conference*, AJTE-6418, 1999.

[161] S. Petrovic, T. Robinson, R. L. Judd, Marangoni heat transfer in subcooled nucleate pool

boiling, *International Journal of Heat and Mass Transfer*, vol. 47, no. 23, pp. 5115-5128, 2004.

[162] I. Golobič, M. Zupančič, Wall-temperature distributions of nucleate pool boiling surfaces vs. boiling curves: A new approach, *International Journal of Heat and Mass Transfer*, vol. 99, pp. 541-547, 2016.

[163] M. Arya, S. Khandekar, D. Pratap, S. A. Ramakrishna, Pool boiling of water on nano-structured micro wires at sub-atmospheric conditions, *Heat and Mass Transfer*, vol. 52, no. 9, pp. 1725-1737, 2016.

[164] S. Sloan, S. Penley, R. A. Wirtz, Sub-atmospheric pressure pool boiling of water on a screen-laminate enhanced surface, *Proceedings of the 25th Annual IEEE Semiconductor Thermal Measurement and Management Symposium*, 246, 2009.

[165] L. Rayleigh, On the pressure developed in a liquid during the collapse of a spherical cavity, *The London, Edinburgh, and Dublin Philosophical Magazine and Journal of Science*, vol. 34, no. 200, pp. 94-98, 1917.

[166] M. S. Plesset, S. Zwick, The growth of vapor bubbles in superheated liquids, *Journal of Applied Physics*, vol. 25, no. 4, pp. 493-500, 1954.

[167] T. Mizushina, R. Toei, Kagaku Kogaku Gairon (in Japanese), Sangyo Tosho, 1979.

[168] E. Wilhelm, R. Battino, R. J. Wilcock, Low-pressure solubility of gases in liquid water, *Chemical Reviews*, vol. 77, no. 2, pp. 219-262, 1977.

[169] J. Liu, M. Do-Quang, G. Amberg, Thermohydrodynamics of boiling in binary compressible fluids, *Physical Review E*, vol. 92, no. 4, 043017, 2015.

[170] J. Liu, G. Amberg, M. Do-Quang, Diffuse interface method for a compressible binary fluid, *Physical Review E*, vol. 93, no. 1, 013121, 2016.

Chapter A

Appendix

A-1 Uncertainty analysis

The uncertainty of the heat flux measurements can be calculated by,

$$\Delta q = \sqrt{\left(\frac{\partial q}{\partial \lambda_{\mathrm{c}}}\Delta\lambda_{\mathrm{c}}\right)^2 + \sum_{i=1}^{3}\left(\frac{\partial q}{\partial T_i}\Delta T_i\right)^2 + \sum_{i=1}^{3}\left(\frac{\partial q}{\partial x_i}\Delta x_i\right)^2} \tag{A.1}$$

where the uncertainty of thermal conductivity of copper, $\Delta\lambda_{\mathrm{c}}$, (literature data) is assumed to be negligible. The uncertainty of a temperature measurement, ΔT_{i}, and position of the thermocouples, Δx_{i}, are 0.2 °C and 0.02 mm, respectively.

For wall superheat,

$$\Delta(\Delta T_{\mathrm{sat}}) = \sqrt{\left(\frac{\partial(\Delta T_{\mathrm{sat}})}{\partial T_{\mathrm{w}}}\Delta T_{\mathrm{w}}\right)^2 + \left(\frac{\partial(\Delta T_{\mathrm{sat}})}{\partial T_{\mathrm{sat}}}\Delta(T_{\mathrm{sat}})\right)^2} \tag{A.2}$$

where ΔT_{w} is derived from the following equation,

$$\Delta T_{\mathrm{w}} = \sqrt{\left(\frac{\partial T_{\mathrm{w}}}{\partial T_1}\Delta T_1\right)^2 + \left(\frac{\partial T_{\mathrm{w}}}{\partial q}\Delta q\right)^2 + \left(\frac{\partial T_{\mathrm{w}}}{\partial x_1}\Delta x_1\right)^2 + \left(\frac{\partial T_{\mathrm{w}}}{\partial \lambda_{\mathrm{c}}}\Delta\lambda_{\mathrm{c}}\right)^2} \tag{A.3}$$

The second term in the square root of eq. (A.2) is neglected in Section 3, because all experiments are carried out at the atmospheric pressure and the uncertainty of the saturation temperature, $\Delta(T_{\mathrm{sat}})$, is small. On the other hand, $\Delta(T_{\mathrm{sat}})$ must be considered in Section 4 since T_{sat} is calculated from bulk water temperature while taking account hydrostatic pressure. $\Delta(T_{\mathrm{sat}})$ is assumed to correspond to the uncertainty of pressure acting on the surface, ΔP_{w}, as shown in the following equation.

$$\Delta P_w = \sqrt{\left(\frac{\partial P_\mathrm{w}}{\partial P_\mathrm{s}}\Delta P_\mathrm{s}\right)^2 + \left(\frac{\partial P_\mathrm{w}}{\partial H}\Delta H\right)^2 + \left(\frac{\partial P_\mathrm{w}}{\partial \rho_\mathrm{l}}\Delta \rho_\mathrm{l}\right)^2} \tag{A.4}$$

where the uncertainty of pressure at the liquid surface, ΔP_s, and height of the liquid surface from the heating surface, ΔH, are about 10% of P_s and 3 mm, respectively. The uncertainty of density of water, $\Delta\rho_\mathrm{l}$, (literature data) is assumed to be negligible.

Finally, the uncertainty of HTC, Δh, is obtained from,

$$\Delta h = \sqrt{\left(\frac{\partial h}{\partial q}\Delta q\right)^2 + \left(\frac{\partial h}{\partial(\Delta T_\mathrm{sat})}\Delta(\Delta T_\mathrm{sat})\right)^2} \tag{A.5}$$

A-2 Contact angle measurement

Contact angle, θ, is measured by the $\theta/2$ method. θ is calculated by the following equation with an assumption that the shape of a droplet is part of a sphere, as shown in Fig. A.1.

$$\tan\frac{\theta}{2} = \frac{H}{r} \quad \rightarrow \quad \theta = 2\tan^{-1}\frac{H}{r} \tag{A.6}$$

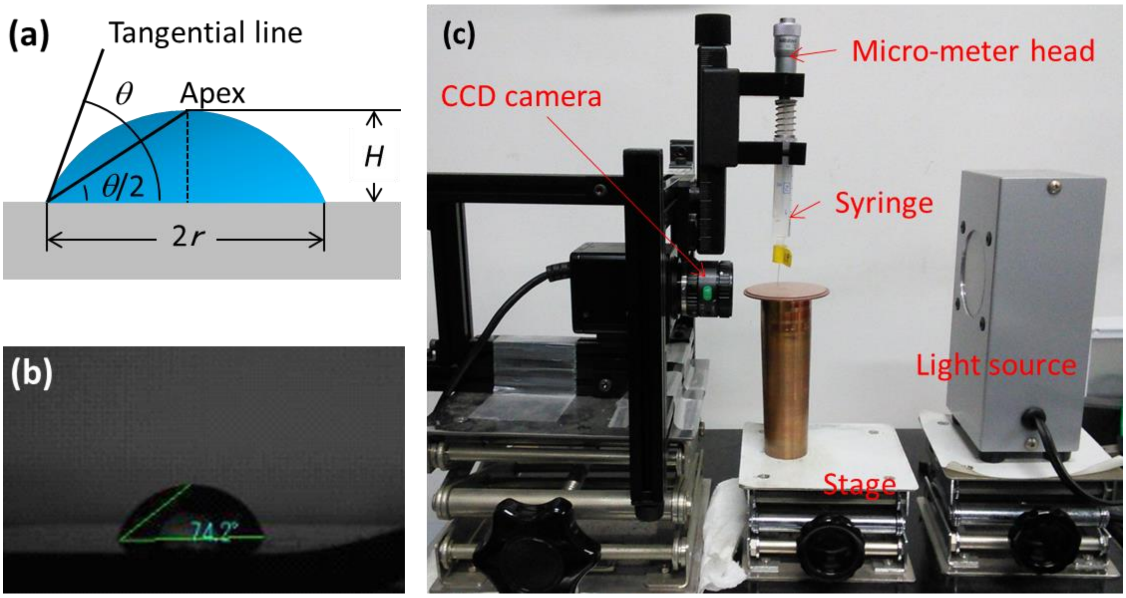

Fig. A.1 (a) Principle of the $\theta/2$ method. (b) Result of a contact angle measurement. (c) Contact angle measurement setup.

where r and H are contact radius and height of the droplet.

A measurement setup is shown in Fig. A.1c. A droplet is formed at the tip of the needle by pushing a syringe, containing pure water, with a micro-meter head. Then, the tip is moved downward to attach the droplet on a sample surface. The droplet is observed by a CCD camera with a light source on the opposing side. The image is captured in a computer, and then, analyzed with an image analysis software (SImage V06, Excimer), as shown in Fig. A.1b.

A-3 Gas solubility

When a gas mixture containing a solute component touches to a liquid, the solute component dissolves into the liquid, and finally, the steady state is reached. At this moment, a concentration of the solute component in the liquid is maximum under the condition. The value of the concentration is called solubility of the gas [167].

Solubility of a solute comportment is independent of the total pressure of the gas phase, and is decided by only partial pressure of the comportment. Solubility of gas decreases as temperature increases. The following liner relationship holds between solubility of gas (in terms of molar fraction), C_g, and partial pressure of the gas in the gas phase, P.

$$P = H_e C_g \tag{A.7}$$

where H_e is Henry's constant. The above equation is called Henry's law, which is available for gases, excluding helium and hydrogen, at partial pressures less than several atmospheric pressures and $C_g \leq 0.03$. H_e is a function of kinds of solvent and solute, and temperature, which is given by the following equation.

$$\ln\left(\frac{H_e}{H_{e0}}\right) = A\left(1 - \frac{T_0}{T}\right) + B\ln\left(\frac{T}{T_0}\right) + C\left(\frac{T}{T_0} - 1\right) \tag{A.8}$$

where $T_0 = 298.15$ K, and H_{e0}, A, B, and C are constants depending on combination of the gas and liquid. Values of the constants for combinations of water and various gasses are

Table A.1 Constants of eq. (A.8) for combinations of water and various gasses.

Gas	H_{e0} [MPa]	A [-]	B [-]	C [-]	Temp. range [K]
N_2	8569	28.952	−24.798		273-349
Air	7262	26.149	−21.652		273-374
O_2	4420	29.339	−24.453		273-349
Ar	4023	25.076	−20.140		273-349
CO_2	165.8	29.319	−21.669	0.3287	273-354

summarized in Table A.1, where reaction in water is neglected for CO_2 [168].

A-4 Detail of numerical simulation

In the present study, the diffuse interface model is employed to qualitatively simulate the phase change process in a binary fluid (i.e., 1-nitrogen and 2-water). The diffuse interface model assumes a finite thickness for the liquid-gas interface, based on the Helmholtz free-energy functional [169, 170]. The surface tension emerges naturally from the continuous transition as a result of incorporating gradient contributions of order parameters (in this case, densities of the two components, ρ_1 and ρ_2) in the energy and entropy formulations. The following scaling is introduced for the simulation, where dimensionless variables are marked with prime (’).

$$r' = L^* r\,,\ \ z' = L^* z\,,\ \ t' = t^* t\,,\ \ \rho' = \rho^* \rho\,,\ \ T' = T^* T\,,\ \ P' = P^* P\,,\ \ e' = \frac{P^*}{\rho^*} e \qquad \text{(A.9)}$$

where the critical parameters of the second component, water, ($\rho^* = m_2/3b_2$, $P^* = a_{22}/27b_2^2$, and $T^* = 8a_{22}/27k_B b_2$, where k_B is the Boltzmann constant) are chosen as the scales of density, pressure, and temperature, respectively. A characteristic length is $L^* = 2b_2^{1/3}$, and a characteristic time is $t^* = 6b_2^{5/6}(m_2/a_{22})^{1/2}$. Here, m_i is molecular mass of the component i, a_{ij} is attraction force between the component i and j, and b_i is molecular volume of the component i. The balance laws for mass, solute transport, momentum, and total energy can be written as follows (omitting ’) with the Helmholtz free-energy density, $f(\rho_1, \rho_2)$.

$$\frac{\partial \rho}{\partial t} + \nabla \cdot \left(\rho \vec{\mathbf{v}}\right) = 0 \tag{A.10}$$

$$\frac{\partial \rho_1}{\partial t} + \nabla \cdot \left(\rho_1 \vec{\mathbf{v}}\right) = \nabla \cdot \left[R_M \frac{\rho_1 \rho_2}{\rho^2} \nabla \left(\frac{\hat{\mu}_1 - \hat{\mu}_2}{T} \right) \right] \tag{A.11}$$

$$\frac{\partial \left(\rho \vec{\mathbf{v}}\right)}{\partial t} + \nabla \cdot \left(\rho \vec{\mathbf{v}} \vec{\mathbf{v}}\right) = R_P \nabla \cdot \overleftrightarrow{\hat{\mathbf{P}}} + \mathrm{Re}^{-1} \nabla \cdot \overleftrightarrow{\mathbf{\Gamma}} + R_G \rho \vec{\mathbf{e}}_{\mathbf{z}} \tag{A.12}$$

$$\begin{aligned} \frac{\partial \left(\rho e\right)}{\partial t} + \nabla \cdot \left(\rho e \vec{\mathbf{v}}\right) = {} & \nabla \cdot \left[\left(\overleftrightarrow{\hat{\mathbf{P}}} + {R_P}^{-1} \mathrm{Re}^{-1} \overleftrightarrow{\mathbf{\Gamma}} \right) \cdot \vec{\mathbf{v}} \right] + R_T \nabla \cdot \left[\left(\lambda_{12} \rho_1 + \rho_2 \right) \nabla T \right] \\ & - \sum_{i,j \in \{1,2\}} \nabla \cdot \left(\frac{TD_{i,j}}{m_i m_j} \frac{d\rho_i}{dt} \nabla \rho_j \right) \end{aligned} \tag{A.13}$$

$$\begin{aligned} f\left(\rho_1, \rho_2\right) = T & \left\{ \frac{8}{3} \rho_1 m_{21} \left[\ln \left(\frac{\rho_1 {m_{21}}^5 R_A}{T^{1.5} (1-\varphi)} \right) - 1 \right] \right\} \\ & - 3 \left(\rho_2^2 + 2 A_{12} m_{21} \rho_1 \rho_2 + A_{21} {m_{21}}^2 \rho_1^2 \right) \end{aligned} \tag{A.14}$$

Here a fraction for the volume fraction occupied by the molecules, φ, is defined as $\varphi = \rho_2/3 + m_{21} B_1 \rho_1$. Dimensionless parameters are $A_{11} = a_{11}/a_{12}$, $A_{12} = a_{12}/a_{22}$, $B_1 = b_1/b_2$, $m_{21} = m_2/m_1$, and $R_{\mathrm{A}} = (1/3)({b_2}^{1/3} \hbar^2 27\Pi/4 a_{22} m_2)^{3/2}$. In the above equation, the generalized chemical potential is described as

$$\hat{\mu}_i = \mu_i - \sum_j \frac{TD_{i,j}}{m_i m_j} \nabla^2 \rho_j \tag{A.15}$$

and the generalized pressure tensor is given as

$$\overleftrightarrow{\hat{P}} = -P \overleftrightarrow{\mathbf{I}} + \overleftrightarrow{\mathbf{P}}_D = -P \overleftrightarrow{\mathbf{I}} + L_D \overleftrightarrow{\mathbf{I}} - \frac{\partial L_D}{\partial \nabla \rho_1} \otimes \nabla \rho_1 - \frac{\partial L_D}{\partial \nabla \rho_2} \otimes \nabla \rho_2 \tag{A.16}$$

where

$$L_D = \sum_{i,j \in \{1,2\}} \rho_i \nabla \cdot \left(\frac{TD_{i,j}}{m_i m_j} \nabla \rho_j \right) + \frac{1}{2} \sum_{i,j \in \{1,2\}} \frac{TD_{i,j}}{m_i m_j} \nabla \rho_i \cdot \nabla \rho_j \tag{A.17}$$

and $\overleftrightarrow{\mathbf{I}}$ is the metric tensor. The thermodynamic pressure is defined as

$$P = \rho_1 \frac{\partial f\left(\rho_1, \rho_2\right)}{\partial \rho_1} + \rho_2 \frac{\partial f\left(\rho_1, \rho_2\right)}{\partial \rho_2} - f\left(\rho_1, \rho_2\right) \tag{A.18}$$

The total energy in eq. (A.13) is described as follows with internal energy in eq. (A.20).

$$\rho e = \rho u + \frac{1}{2R_P}\rho \vec{\mathbf{v}}^2 \tag{A.19}$$

$$\rho u = f\left(\rho_1, \rho_2\right) - T\frac{\partial f\left(\rho_1, \rho_2\right)}{\partial T} \tag{A.20}$$

In eq. (A.12) and (A.13), the viscous tensor is given as

$$\vec{\boldsymbol{\Gamma}} = \left(\eta_{12}\rho_1 + \rho_2\right)\left(\nabla\vec{\mathbf{v}} + \nabla\vec{\mathbf{v}}^{\perp}\right) + \frac{1}{3}\left(\eta_{12}\rho_1 + \rho_2\right)\vec{\mathbf{I}}\nabla\cdot\vec{\mathbf{v}} \tag{A.21}$$

where $\eta_{12} = \eta_1/\eta_2$ is a ratio of dynamic viscosities of the two components. The rest of the dimensionless parameters are as follows: Reynolds number, $Re = L^{*2}/t^*\eta_2$; a ratio of attractive potential energy to molecular kinetic energy, $R_\mathrm{p} = P^* t^{*2}/\rho^* L^{*2}$; a ratio of thermal conductivity of the two components, $\lambda_{12} = \lambda_1/\lambda_2$; the normalized mobility coefficient, $R_\mathrm{M} = P^* t^* M_\mathrm{f}/L^* 2\rho$; $R_T = \lambda_2 T^*/\rho^* e^* v^* L^*$ and $D_{ij} = \varkappa_{ij} k_B T^* \rho^{*2}/m_2^2 L^{*2} P$, which relates to the surface tension through bulk Helmholtz free energy,

$$\hat{f}\left(\rho_1, \rho_2\right) = f\left(\rho_1, \rho_2\right) + \frac{1}{2}\sum_{i,j\leftrightarrow\in\{1,2\}} \kappa_{ij}\nabla\rho_i\cdot\nabla\rho_j \tag{A.22}$$

or, in a more explicit form with x representing the coordinate normal to the interface

$$\sigma = \sum_{i,j\in\{1,2\}} \int_{-\infty}^{+\infty} \kappa_{ij}\frac{\partial\rho_i}{\partial x}\frac{\partial\rho_j}{\partial x}dx \tag{A.23}$$

where $\varkappa_\mathrm{ij}$ (i = j) is capillary coefficient of the component i and $\varkappa_\mathrm{ij}$ (i ≠ j) is the mixing parameter. The normalized gravitational acceleration is formulated as $R_\mathrm{G} = t^{*2}g/L^*$. From the point of view of computational cost, the physical model is limited to extremely small space (hundreds of nanometers) and time scales (a few nanoseconds). Consequently, gravitational acceleration, g, needs to be artificially increased by more than nine orders of magnitude in order to have an appreciable impact on bubble dynamics.

All simulations have been performed using a finite-element numerical toolbox femLego, which employs symbolic computation to solve complex partial differential equations. Specifically, the formulations (including governing equations, initial and boundary conditions) were fed into a single MAPLE worksheet. Then, they were automatically complied into complete computer source codes (both in C and FORTRAN). The numerical scheme was based on the characteristic-based split (CBS) method. The piecewise linear approximation and first-order Euler forward scheme were used for space and time discretization, respectively. In addition, the adaptive mesh technique was employed to calculate the liquid-gas interfacial region, where density gradient was large. Iteration tolerances for all the equations were set to 10^{-8}.

An axisymmetric domain ($0.001 \leq r \leq 100.001$, $-300.001 \leq z \leq -0.001$, with the plane of symmetry ($r = 0$) is removed to avoid potential singularity) was considered. At the initial condition (with a uniform system temperature of $T_i = 0.80$), the domain was filled with a two-phase mixture of water and nitrogen: $\rho_i^{\mathrm{v}} = 0.241$ (gaseous phase) in the upper one-third of the enclosure; and $\rho_i^{\mathrm{l}} = 1.934$ (aqueous phase) in the lower two-thirds. The symmetric boundary condition was applied to the left boundary, and the other walls assumed to be no-slip. The bottom and top walls were isothermal (Dirichlet), while the right wall was completely insulated (Neumann). A dilute presence of nitrogen ($\rho_1 = 0.01$) was evenly distributed everywhere in the initial state.

Firstly, the thermodynamic equilibrium state of this binary system was obtained under gravity ($R_{\mathrm{G}} = 5\times10^{-4}$) and a vertical temperature gradient (with a temperature at the bottom wall of $T_{\mathrm{bot}} = 0.82$). The relevant parameters in the condition were given as follows: $m_{21} = 0.8111$, $R_{\mathrm{A}} = 1.332\times10^{-5}$, $B_1 = 1.267$, $A_{11} = 0.247$, $R_{\mathrm{M}} = 0.170$, $D_{11} = 0.01$, and $D_{22} = 1.0$. Also, a non-zero A_{12} ($= 0.1$) was chosen, so that water and nitrogen could coexist in both aqueous and gaseous states. Furthermore, since $A_{12} < A_{11}$, nitrogen molecules evidently prefer the company of their own kind. As a result, nitrogen molecules slowly moved across the interface from the liquid phase to the gas phase.

The initialization led to a mean steady-state density of $\rho_1^{\mathrm{l}} = 6.604\times10^{-3}$ and $\rho_1^{\mathrm{v}} =$

1.703×10^{-2} in the aqueous and gaseous phase, respectively. Next, based on the obtained initial conditions, simulations were carried out for bubble behaviour in pool boiling with and without a presence of dissolved gas. In the simulation, a computational grid of 41×121 and a uniform time step of $\Delta t = 0.01$ were used. A saturated bubble embryo with a radius of $R_\mathrm{b} = 40$ and temperature $T_\mathrm{b} = 0.91$ containing a small amount of nitrogen gas ($\rho_1{}^\mathrm{b}=0.01$) was placed at $r = 0$ and $z = -265$, with a temperature at the bottom wall of $T_\mathrm{bot} = 0.91$. Thus, Bond number was $Bo_\mathrm{sim} = 6.95$, which more or less matches that of the experiment, $Bo_\mathrm{ex} = 5.94$. The wetting boundary conditions at a solid wall for a binary fluid can be written as,

$$\left(\kappa_{11}\nabla\rho_1 + \kappa_{12}\nabla\rho_2\right)\cdot\vec{\mathbf{n}} = \sigma\cos\theta_\mathrm{e}\frac{\partial G}{\partial\rho_1} \tag{A.24}$$

$$\left(\kappa_{21}\nabla\rho_1 + \kappa_{22}\nabla\rho_2\right)\cdot\vec{\mathbf{n}} = \sigma\cos\theta_\mathrm{e}\frac{\partial G}{\partial\rho_2} \tag{A.25}$$

where $\vec{\mathbf{n}}$ is a unit vector normal to the surface and θ_e is equilibrium contact angle. By assuming that contact line motion is independent of dissolved gas, the above equations can be simplified to

$$\kappa_{22}\nabla\rho\cdot\vec{\mathbf{n}} = \sigma\cos\theta_\mathrm{e}\frac{\partial G}{\partial\rho} \tag{A.26}$$

For a single component system, eq. (A.26) is also available. Here the nondimensional third-order polynomial function $\Gamma(\rho)$ was described as, $\Gamma(\rho) = -1.071\rho^3+3.34\rho^2-2.267\rho$. To simulate a biphilic surface, a non-uniform θ_e was assumed for the bottom wall ($\theta_\mathrm{e} = 120^\circ$ for $r < 30$; $\theta_\mathrm{e} = 10^\circ$ for $r > 30$). The two domains are smoothly connected with a hyperbolic tangent function at $r = 30$.